DOCTORAL THESIS

Computational models of rodent hippocampal nerve cells focusing on their morphology, excitability and function

by

Martin Mittag

JUSTUS-LIEBIG-
UNIVERSITÄT
GIESSEN

Institut für Theoretische Physik
Justus-Liebig-Universität Gießen

Gießen, 2023

Supervised by
Prof. Dr. Christian Heiliger
Prof. Dr. Peter Jedlička

Kein Wesen kann zu Nichts zerfallen!
Das Ew'ge regt sich fort in allen,
Am Sein erhalte dich beglückt!
Das Sein ist ewig; denn Gesetze
Bewahren die lebend'gen Schätze,
Aus welchen sich das All geschmückt.
Goethe

Contents

List of Abbreviations

ab	adult born
AD	Alzheimer's disease
AHP	afterhyperpolarisation
AIS	axon initial segment
AMPA	Alpha-amino-3-hydroxy-5-Methyl-4-isoxazole-Propionic Acid
AP	action potential
APP/PS1	human transgenes with APP Swedish mutation and PSEN1 with L166P mutation
ATP	adenosine triphosphate
BK	large-conductance Ca^{2+}-gated K^+ channel
CA	cornu ammonis region of CA1, CA2 and CA3
cv	coefficient of variation
DG	dentate gyrus
EA	Eingabe-Ausgabe
EC	entorhinal cortex
E/I	excitation-inhibition
EPSP	excitatory postsynaptic potential
GABA	Gamma-Aminobutyric Acid
GC	granule cell
GCL	granule cell layer
HF	hippocampal formation
HVA	high voltage-activated
IML	inner molecular layer
IO	input-output
ISI	inter-spike-interval
L5	layer five
LEC	lateral entorhinal cortex
LIF	leaky integrate fire model
LTP/LTD	long-term-potentiation and long-term-depression
MEC	medial entorhinal cortex
mGC	mature granule cell
MI	mutual information
MML	middle molecular layer
MVA	medium voltage-activated
NMDA	N-Methyl-D-Aspartate
OML	outer molecular layer
PDF	probability density function
PC	pyramidal cell
SEM	standard error of the mean
SK	small-conductance Ca^{2+}-gated K^+ channel
SLM	stratum lacunosum-moleculare
SO	stratum oriens
SP	stratum pyramidale
SR	stratum radiatum
Sub	subiculum
T2N	TREES-to-NEURON interface
WT	wild type

List of Figures

1 Abstract

The nerve cells in the mammalian brain come in various shapes and sizes. They constitute a complex system emerging from a complicated interplay of biophysical principles. Functionally, they can be compared to a computing unit transferring input into useful output, leading ultimately to cognitive functions or behaviour. This processing of information is called the input-output (IO) function of a neuron. The focus of this dissertation is on the particular IO function of hippocampal neurons, their underlying structure (morphology) and their intrinsic mechanisms (ion channels). In order to study these nerve cells, computational models offer the advantage of disentangling the involved biophysical mechanisms and their functional effects in a controlled manner. Therefore, I implement biologically realistic computational models of hippocampal neurons to simulate their IO function in several major, complementary *in silico* investigations. Initially, using detailed neuron models that include active ion channels and other dendritic non-linearities, I demonstrate that the neural IO function can be invariant even when the stimulated dendrites of the nerve cells show vastly different morphological structures and sizes. These results reveal a general principle called accordingly "dendritic constancy". Notably, the dendritic constancy principle can have important clinical implications for neurological diseases. For example, it has been suggested that morphological alterations lead to the concurrent increase in excitability of principal hippocampal nerve cells during Alzheimer's disease (AD). However, in line with the dendritic constancy principle, I show that the dendritic remodeling in AD cells is likely a homeostatic mechanism to maintain the cell IO function and information flow. The simulations instead reveal, that other intrinsic (ion channels) and extrinsic mechanism modifications lead to the excitability increase observed in AD cells in a multi-causal manner. Finally, various expressions of underlying ion channels cannot only affect the altered, pathological behaviour but potentially result in an optimised IO function and information processing. For instance, hippocampal granule cells (GCs) are believed to convert similar inputs into dissimilar outputs (pattern separation) while using as little energy as possible. The findings in this thesis reveal that the experimentally validated GC model seems to be close to optimal among a population of random, but valid, GC models with different ion channel expressions for the simultaneous performance of pattern separation and economy. In summary, by applying computational models in this dissertation I uncover a relationship between the underlying structure and ion channels of various nerve cells and their IO function.

2 Zusammenfassung

Die Nervenzellen von Säugetieren können verschiedene Formen und Größen aufweisen. Sie bilden ein komplexes System, das sich aus einem komplizierten Zusammenspiel biophysikalischer Prinzipien ergibt. Funktionell können sie mit einer Recheneinheit verglichen werden, die Eingaben in nützliche Ausgaben umwandelt, was schließlich zu kognitiven Funktionen oder Verhalten führt. Diese Informationsverarbeitung wird als Eingabe-Ausgabe (EA) Funktion bezeichnet. Der Schwerpunkt dieser Dissertation liegt auf der spezifischen EA-Funktion von Neuronen des Hippocampus, ihrer zugrunde liegenden Struktur (Morphologie) und ihren intrinsischen Mechanismen (Ionenkanäle). Zur Untersuchung dieser Nervenzellen bieten Computermodelle den Vorteil, die beteiligten biophysikalischen Mechanismen und ihre funktionellen Auswirkungen kontrolliert zu analysieren. Zunächst zeige ich mit detaillierten Neuronenmodellen, dass die EA-Funktion selbst dann konstant sein kann, wenn die stimulierten Dendriten sehr unterschiedliche Strukturen und Größen aufweisen. Diese Ergebnisse offenbaren ein allgemeines Prinzip, das entsprechend als "dendritische Konstanz" bezeichnet wird. Das Prinzip der dendritischen Konstanz kann zudem wichtige klinische Auswirkungen für neurologische Erkrankungen haben. So wurde beispielsweise vermutet, dass morphologische Veränderungen zu einer gleichzeitigen Erhöhung der Erregbarkeit der Pyramidalzellen des Hippocampus bei Alzheimer führen. In Übereinstimmung mit dem Prinzip der dendritischen Konstanz zeige ich jedoch, dass dendritische Veränderungen in Alzheimer wahrscheinlich ein homöostatischer Mechanismus zur Aufrechterhaltung der EA-Funktion sind. Die Simulationen demonstrieren stattdessen, dass andere intrinsische (Ionenkanäle) und extrinsische Mechanismen auf multikausaler Weise zu der beobachteten Erhöhung der Erregbarkeit in Alzheimer führen. Darüber hinaus können verschiedene Ausprägungen der zugrunde liegenden Ionenkanäle möglicherweise auch zu einer optimierten EA-Funktion und Informationsverarbeitung führen. Es wird beispielsweise angenommen, dass die Körnerzellen des Hippocampus ähnliche Eingaben in unterschiedliche Ausgaben umwandeln (Mustertrennung). Die Ergebnisse dieser Doktorarbeit belegen, dass das experimentell validierte Körnerzellen-Modell im Vergleich zu einer Vielzahl an gültigen Modellen mit variierten Ionenkanälen nahezu optimal zu operieren scheint für die gleichzeitige Maximierung der funktionellen EA-Mustertrennung und Energieminimierung. Zusammenfassend zeige ich mit Hilfe von Computermodellen in dieser Dissertation eine Relation zwischen den zugrunde liegenden Strukturen und Ionenkanälen von Nervenzellen und ihrer EA-Funktion auf.

3 Introduction

What is the input-output (IO) relationship of a nerve cell, one of the main computational units in the brain? Can it be calculated? The IO function of a neuron is commonly considered as the information flow within the cell in the following order: the reception of inputs in the dendrites (the tree-like structure of the nerve cell), the integration of the signals on their way to the soma (the cell body), the generation of action potentials (reversed potential) near the soma and eventually the further flow of the output via the axon connected to other neurons (Cook *et al.*, 2007). The overall picture of neural function via dendritic integration and computation of the input signals is rather complicated with non-linear processes involved and has been studied in detail in the past decades (Rall, 1959; Segev and London, 2000; London and Häusser, 2005; Poirazi and Papoutsi, 2020). Following in the footsteps of these works, this dissertation constitutes a contribution to realistic single nerve cell modelling. The emphasis is on the structure-function relationship at the interplay of morphological and compartmental modelling with active mechanisms to simulate the IO function of rodent hippocampal neurons. The IO function is exemplified in three major, complementary investigations in this thesis: first, general invariant principles; second, pathologically altered activity; third, optimised performance.

The introduction gives background information about theoretical fundamentals that are considered necessary in understanding the research in this thesis. Initially, the passive cable equation by Rall is introduced in 3.1, and its further application to dendritic trees with synaptic activation is derived in 3.2. Next, the passive cell model is extended to an active and more realistic cell model by including voltage-dependent ion channels. Therefore, the Hodgkin & Huxley model as well as the compartmental neuron model with ionic currents are introduced in 3.3 and 3.4. Compartmental models constitute the main computational modelling of nerve cells in this thesis. These nerve cells are located in the rodent hippocampus for all investigations here. Consequently, a neurophysiological background of this brain region is given in 3.5. Importantly, nerve cells can undergo pathological changes leading to impaired IO function. A prominent, pathological example is AD hyperexcitability for which an overview is given in 3.6. Subsequently, section 3.7 introduces the concept of Pareto optimization and a new measure for pattern separation. Both are important tools to investigate the IO function of hippocampal GCs. Thereby, mature GCs are compared to newly formed GCs. The introduction is closed with section 3.8 detailing the scope and aim of this dissertation.

3.1 The passive cable model of a nerve cell

What influence does cell structure have on cell activity and are there analytical tools to investigate it? When we observe the difference in morphology and topology in various neuronal cells we can easily assume that different structural architecture points to different function and behaviour of the cells. Previous work has demonstrated that indeed the computation done in the dendrites is complex and depends on morphology (Vetter *et al.*, 2001; Kath, 2005; London and Häusser, 2005; Silver, 2010; Poirazi and Papoutsi, 2020; Gidon *et al.*, 2020; Bicknell and Häusser, 2021). Consequently, changes in size or layout of that morphology can alter the excitability and spiking behaviour of the cell (Krichmar *et al.*, 2002; Van Ooyen *et al.*, 2002; van Elburg and van Ooyen, 2010). At the same time, even with such high diversity of dendritic structures among the cells there exist constraints and scaling laws that limit and predict morphological size and shape (Wittenberg and Wang, 2007; Teeter and Stevens, 2011; Cuntz *et al.*, 2012, 2013). In addition, general principles have been demonstrated that preserve specific passive and active electrotonic properties independent of cell size or shape (Jaffe and Carnevale, 1999; Häusser, 2001; Bakken and Stevens, 2012; Bird and Cuntz, 2016; Cuntz *et al.*, 2021).

Seminal theoretical work on electrotonic features and the prediction of the electric potential in neurons and dendrites with only passive properties has been done by e.g. Rall, Rinzel, Koch and Segev (Rall, 1959; Rall *et al.*, 1967; Rinzel and Rall, 1974; Segev and Rall, 1988; Koch and Segev, 1998). An important example of a cell's property is the input resistance, which is dependent on the cell's size (Rall, 1959, 1962). With other passive and active electrotonic properties being the same, a larger cell usually has more dendritic cable resulting in a stronger leak and therefore a larger input conductance, or inversely, the input resistance is smaller compared to a smaller cell. As a consequence (Ohm's law), the cell is less excitable (less depolarisation) if somatic current injection is considered.

The main idea of Rall (Rall, 1959, 1962) was to treat the branch of a neuronal dendrite as a passive, conducting cable comparable to cables in telegraph communication and their mathematical descriptions. Thereby, the branch $L(x)$ at location x is discretised into several segments. Within a dendritic segment Δx the potential $V(x)$ and current $I(x)$ are considered uniform. Each segment is surrounded by a membrane that consists of two thin layers. In electrical terms it can be represented by a capacitor. The cable here is considered passive,

which means the membrane resistance is voltage independent. Characteristic properties of the cable and its membrane are therefore the specific membrane resistance R_m (in Ωcm^2), the specific axial resistance R_a (in Ωcm) and the specific membrane capacitance C_m (in F/cm^2) applied to a cylindrical dendritic segment with membrane surface as in Figure 1.

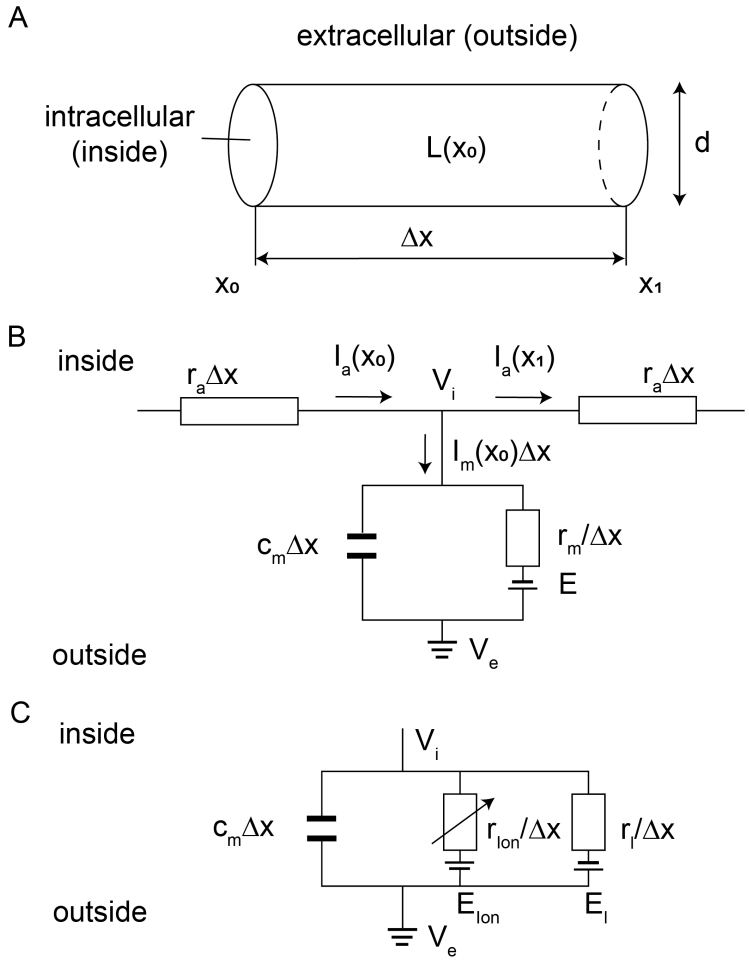

Figure 1. Analogy of a piece of dendrite as a cable and an electrical circuit

A, Dendritic segments can be described as a cylindrical cable with diameter d (in cm) and length Δx (in cm) as in Rall (1959, 1962). **B**, The dendrite can be compared to an electrical circuit with the axial segments of the internal medium as axial resistances $r_a = 4R_a/(\pi d^2)$ (in Ω/cm) in a row and with the membrane as the membrane capacitance $c_m = C_m \pi d$ (in F/cm) and resistance $r_m = R_m/(\pi d)$ (in Ωcm) in parallel, contributing to the membrane current I_m that leaks from I_a. The quantities are defined with respect to a unit length of the cylinder and have to be scaled with the increment Δx ($\Delta x \to 0$ in equations). V_i, V_e and E are the intracellular, extracellular and resting membrane potential respectively, resulting in electrotonic potential $V = V_i - V_e - E$. **C**, An active membrane patch includes voltage-dependent resistances r_{ion} per ion species in addition to the constant leak r_l with their respective equilibrium potentials E_{ion} and E_l as batteries.

Three rules and their interplay within an electrical network are important in deriving the cable equation to calculate current I and voltage V in a dendrite: Ohm's law, $V = IR$; capacitor formula, $I = C\frac{dV}{dt}$; and Kirchhoff's rule of current conservation at a node, $\sum I = 0$. The schematic in **Figure 1 B** summarizes the cable theory of a dendrite as an electrical circuit. First, when only the current in axial direction is considered without any leak from the membrane, it follows that, by using Ohm's law, a current injection at x will result in a voltage change at $x + \Delta x$ (Rall, 1959; Nelson *et al.*, 2008):

$$V(x) - V(x + \Delta x) = I_a(x,t)\Delta x \frac{R_a}{\pi(d/2)^2} \Rightarrow \frac{\partial V}{\partial x}(x,t) = -I_a(x,t)\frac{R_a}{\pi(d/2)^2} \tag{1}$$

The right side switched to a continuous representation with $\Delta x \to 0$. The specific axial resistance R_a is a fundamental quantity for a unit length and had to be divided by the cross sectional area $\pi(d/2)^2$ to account for the whole cylindrical segment. Next, when also the membrane resistance is included, it follows that the axial current leaks through the membrane proportional to the considered distance Δx. It can be described by Kirchhoff's rule as the currents are conserved:

$$I_a(x) - I_a(x + \Delta x) = I_m(x,t)\Delta x \Rightarrow \frac{\partial I_a}{\partial x}(x,t) = -I_m(x,t) \tag{2}$$

Thereby, the membrane current is defined as current flow across the membrane per unit length in A/m. When substituting I_a from **Equation 1** into **2** one obtains:

$$\frac{\partial^2 V}{\partial x^2}(x,t) = I_m(x,t)\frac{R_a}{\pi(d/2)^2} \tag{3}$$

Additionally, the membrane current is composed of two parts: the capacitive current due to the capacitance formula and the leak current due to Ohm's law (**Figure 1 B**). The membrane current further has to be scaled with the membrane circumference πd to account for the whole cylindrical segment. This results in:

$$I_m(x,t) = I_C(x,t) + I_{leak}(x,t) = \pi d(C_m\frac{\partial V}{\partial t}(x,t) + \frac{V}{R_m}(x,t)) \tag{4}$$

Combining **Equations 3** and **4** results into the cable equation:

$$\lambda^2\frac{\partial^2 V}{\partial x^2}(x,t) = \tau\frac{\partial V}{\partial t}(x,t) + V(x,t) \tag{5}$$

The general form of the cable equation is a second order differential equation of the electrotonic potential V with $V = V_m - E$, the difference between membrane potential V_m and resting membrane potential E as the driving force, and $V_m = V_i - V_e$, the difference between intracellular and extracellular potential. Thereby, λ is the electrotonic length constant $\lambda = \sqrt{(R_m/R_a)(d/4)}$ (in m) and τ is the time constant $\tau = R_m C_m$ (in s) describing the voltage attenuation over space and time respectively. The steady-state solution at $\partial V/\partial t = 0$ for a semi-infinite cable with somatic current injection I_{app} and somatic voltage response $V_0 = V(x = x_0)$ is as follows:

$$V(x) = V_0 e^{-x/\lambda} \tag{6}$$

The voltage V in that case decays with $1/e \approx 37\%$ at distance λ. Another particular boundary condition is the case of a natural sealed end of a terminal dendritic branch which is more relevant for a real morphology. In that case, a closed cable of total length l is considered, which results in the following solution (Rall, 1959):

$$V(x) = V_0 \left[\frac{\cosh\left(\frac{l-x}{\lambda}\right)}{\cosh\left(\frac{l}{\lambda}\right)} \right] \tag{7}$$

Since the cable equation in 5 is only linearly depending on V, and as the example of the steady-state solution is an exponentially decaying voltage signal, it is obvious, that the cable equation in this form can not have a traveling wave solution. It can therefore not transmit pulses as observed in neural action potentials. In addition, distributed synaptic inputs to a branching dendrite are more realistic than the somatic input here. These issues are addressed in the next sections.

3.2 The passive cable equation to distributed synaptic inputs

Complementary to somatic inputs, synaptic inputs and dendritic current transfer have also, but rarely, been explored (Rall *et al.*, 1967; Rall and Rinzel, 1973; Rinzel and Rall, 1974; London *et al.*, 1999; Segev and London, 2000; Bird and Cuntz, 2016; Bird *et al.*, 2021b). However, only recently synaptic current injections on a level of whole cell distributed synaptic inputs have been examined regarding the IO behaviour of cells with different sizes and shapes. Such investigation resulted in the discovery of the general principle of dendritic constancy, meaning that the output voltage remains largely invariant to dendritic length for synaptic activation

(Cuntz *et al.*, 2021). According to the analytical calculation along the entire electrotonic length, input resistance (decreased in a larger cell) and synaptic currents (increased in a larger cell with constant density) cancel one another. The solution in the paper by Cuntz *et al.* (2021) is a continuation of the works by Rall (1959); Rall *et al.* (1967); Koch and Segev (1998), represented by the **Equations 5** and **7** derived above, for a closed cable of total length l with synaptic current injections. For the voltage $v_x(0)$ at the root due to current injection I_{app} in the dendrites at a distance x from the soma one obtains:

$$v_x(0) = \frac{I_{app}}{G_\infty} \left[\frac{\cosh\left(\frac{l-x}{\lambda}\right)}{\sinh\left(\frac{l}{\lambda}\right)} \right] \tag{8}$$

Thereby, G_∞ is the input conductance at the proximal sealed end in a semi-infinite cable and λ the length constant as introduced above. When short cables are considered, G_∞ depends only linearly on λ and can be approximated with the total conductance of a λ length cylinder of the cable $G_\infty = G_m \pi d \lambda$. Additionally, it could be shown an equivalence of voltage responses to distributed current injections I_{dist} per unit length and the total current that was inserted over the total length l of the cell (Cuntz *et al.*, 2021). To get the total voltage V for all injected currents the integral from **Equation 8** has to be taken over all synaptic sites x:

$$V_{dist} = \frac{I_{dist}}{G_\infty \sinh\left(\frac{l}{\lambda}\right)} \int_0^l \cosh\left(\frac{l-x}{\lambda}\right) dx \tag{9}$$

$$V_{dist} = \frac{I_{dist}\lambda}{G_\infty} = \frac{I_{dist}}{G_m \pi d} \tag{10}$$

The shape of this equation shows a clear similarity to Ohm's law. It can be considered as an adaptation of the law to the case of dendritic trees (Cuntz *et al.*, 2021). In that case, the voltage responses to distributed synaptic inputs are independent of the (cable) length of the neuronal cell. They depend however on the specific membrane conductance G_m (inverse of R_m) and the diameter d of the cable. They also depend on the specific axial resistance R_a via I_{dist} defined per unit electrotonic length. In comparison, voltage responses to proximal and especially somatic current injections follow the relation $V = \frac{I}{G_\infty \tanh(l/\lambda))}$, which means a big cell with long length l and short length constant λ leads to small V. Looking at biological neurons and their environment, the most likely scenario for inputs are excitatory, synaptic inputs to the dendritic tree of the cell. They are distributed over the whole cell instead of the soma only. These synaptic currents first go through synaptic conductances which add to the

overall conductance per unit length under the condition of invariant synapse density. As a result, the voltage responses to distributed synaptic conductances are a little lower than the ones from current injections above. Importantly, there is still no length dependency of the voltage response (Cuntz *et al.*, 2021):

$$V_{syn} = \frac{I_{syn}}{G_m \pi d + G_{syn}} \tag{11}$$

Here, G_{syn} is the specific synaptic conductance. In conclusion, the analytical calculations and numerical simulations in Cuntz *et al.* (2021) reveal an electrotonic principle of dendritic constancy ensuring an equal impact of distributed synaptic inputs in a passive cable independent of its length.

Consequently, in the paper by Cuntz *et al.* (2021) the derived equations were tested and applied to a database of different neuronal cell types showing a wide range of size and complexity. Thereby, real dendritic morphologies from the *NeuroMorpho.Org* database were selected (July 2016, Ascoli *et al.*, 2007; 9841 reconstructions). After normalising the diameters (to an average diameter of $1 \mu m$) and applying common values of $G_m = 50 \frac{\mu S}{cm^2}$ for the specific membrane conductance, the steady-state voltage responses to distributed synaptic inputs were measured (**Figure 2**). As a result, a striking similarity of voltage responses for dendrites with different lengths spanning five orders of magnitude and including a large variety of different cell types and shapes was observed (Cuntz *et al.*, 2021). Importantly, at the far left and the far right end of the curve in the rare cases of very small or very large neuronal morphologies (yellow and red dots in **Figure 2**), the voltage response differed more compared to the average and the analytical predictions. The black line corresponded here to the analytical prediction from **Equation 10** (equation 1 in Cuntz *et al.*, 2021). As a statistical analysis of the data a linear regression was applied. It demonstrated a small overall downward slope of -0.2% per mm that was statistically significant (Cuntz *et al.*, 2021). Overall, however, the average voltage change could be well approximated with the derived **Equation 10**.

For real cells with active membrane kinetics such an analytic solution as in **Equation 11** does not exist though. Active (voltage-dependent) ion channels, together with other non-linear processes in the dendrites, add complexities to the dendritic computation and signal transfer that make it difficult to analyze mathematically. However, in order to describe the voltage signal in a neuron realistically and accurately, ion channels and their dynamics have to be

included in the calculation of the IO function. An important historic approach and model, that includes ion currents, is introduced in the next section.

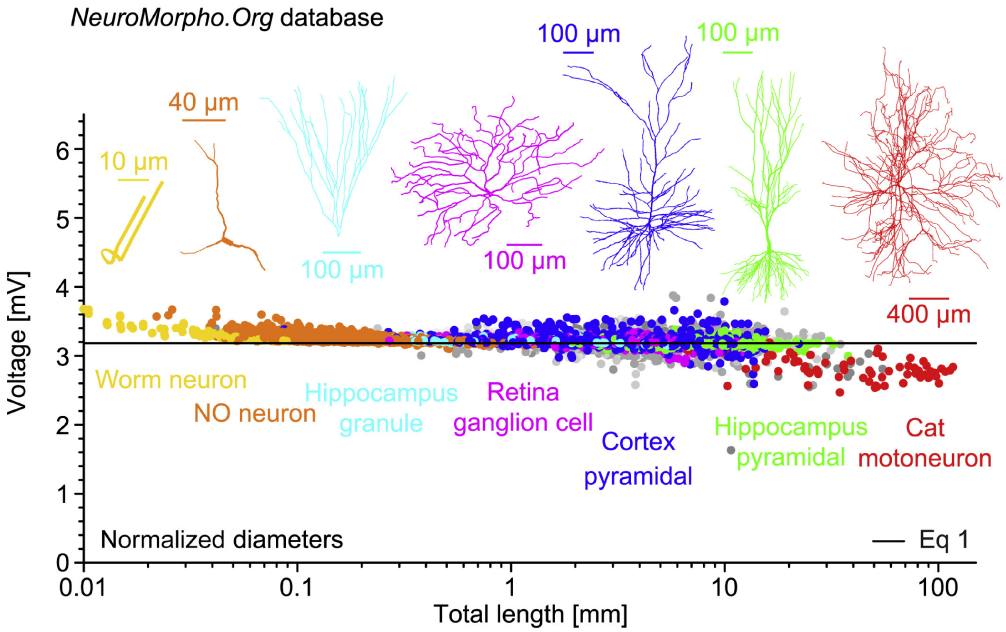

Figure 2. Dendritic constancy leads to striking similarity of the IO function for distributed inputs in passive neurons of different shapes covering orders of magnitude in size

Reproduced Figure 4 A *Top* from "A general principle of dendritic constancy: A neuron's size- and shape-invariant excitability" (Reference: Cuntz *et al.*, 2021, doi: https://doi.org/10.1016/j.neuron.2021.08.028) by Cuntz H, Bird AD, Mittag M, Beining M, Schneider M, Mediavilla L, Hoffmann FZ, Deller T, Jedlicka P in *Neuron, 2021,* and licensed under an Elsevier user license (Copyright Elsevier Inc. 2021, https://www.elsevier.com/about/policies-and-standards/open-access-licenses/elsevier-user):
Somatic voltage change to dendritic inputs in morphologies from *NeuroMorpho.org* including 223 datasets with 9841 reconstructions after diameter normalization ($1\mu m$). Different cell groups are shown in different colors (see labels). The *black* line corresponds to the analytical prediction from **Equation 10** (equation 1 in Cuntz *et al.*, 2021).

3.3 The Hodgkin & Huxley model

A real nerve cell is not just a passive cable. The cell membrane is permeable to several ion species, most notably sodium and potassium, in an activity-dependent manner. Bernstein, Hodgkin, Huxley and Katz (among others) contributed seminal work in the discovery of the importance of ions in membrane mechanisms and action potential (AP) propagation in neurons (Bernstein, 1902; Hodgkin and Katz, 1949; Hodgkin *et al.*, 1952; Hodgkin and Huxley,

1952). When ion currents for sodium and potassium are included in the membrane current, it follows that **Equation 4** from the cable model has to be adapted. For a membrane patch without axial dependence it follows (Nelson *et al.*, 2008; Mallot, 2013):

$$I_m(t) = I_C(t) + I_K(t) + I_{Na}(t) + I_{leak}(t) \tag{12}$$

$$I_m(t) = C_m \frac{dV}{dt}(t) + g_K(V(t) - E_K) + g_{Na}(V(t) - E_{Na}) + g_l(V(t) - E_l) \tag{13}$$

The equilibrium potentials E are a result of the electrochemical gradient due to the concentration differences of the ions inside and outside the membrane, and are calculated by the Nernst potential for each ion species.

For example, the squid giant axon in the experiments by Hodgkin and Huxley (1952) displayed potentials for sodium and potassium at $E_K = -75mV$ and $E_{Na} = 54mV$. This was quite different to the actual potential of the membrane at $E_{rest} = -60mV$, especially for sodium, and was therefore called the sodium anomaly. Inspired by the membrane theory of selective permeability by Bernstein (1902) and as a consequence of the sodium anomaly, Hodgkin and Huxley proposed their ion channel hypothesis: The membrane mechanisms consist of various voltage-gated ion channels, which open and close with a certain probability to let ions flow inside and outside the cell depending on as well as leading to the observed polarisation reversal. Mathematically interpreted, the ion conductances depend on time and voltage ($g(V,t)$, see also $R_{ion}(V,t)$ in **Figure 1 C**). In order to fit the measured, variable conductances to a formula, two experimental techniques had to be employed. First, voltage clamps were developed to maintain the membrane potential at a target voltage. Second, the ion currents were disentangled by controlling the extracellular sodium concentration. Subsequently, the following model consisting of four coupled differential equations was developed by Hodgkin and Huxley (1952):

$$I_m(t) = C_m \frac{dV}{dt}(t) + \bar{g}_K n^4 (V(t) - E_K) + \bar{g}_{Na} m^3 h (V(t) - E_{Na}) + \bar{g}_l (V(t) - E_l) \tag{14}$$

$$\frac{dn}{dt} = \alpha_n(V)(1-n) - \beta_n(V)n \tag{15}$$

$$\frac{dm}{dt} = \alpha_m(V)(1-m) - \beta_m(V)m \tag{16}$$

$$\frac{dh}{dt} = \alpha_h(V)(1-h) - \beta_h(V)h \tag{17}$$

Here, α and β are rate constants that depend only on the voltage, $\bar{g}$ is the maximum of the conductance g, and n, m, h are probabilities that represent the activation and inactivation of the potassium and sodium channels. Hodgkin and Huxley called them gating variables and postulated that they represent the dynamics of the underlying ion channels. Astonishingly, the formulated dynamics indeed fit the underlying structure. For instance, the potassium channel of the squid axon consists of four subunits which are well represented by the fourth power of n. Only when all subunits are open the potassium ions can flow through the membrane.

Taking the passive cable **Equation 5** from Rall and combining it with the model from Hodgkin and Huxley results in the following equation for the total voltage:

$$\frac{1}{R_a}\frac{\partial^2 V}{\partial x^2}(x,t) = C_m\frac{dV}{dt}(t) + \bar{g}_K n^4(V(t)-E_K) + \bar{g}_{Na} m^3 h(V(t)-E_{Na}) + \bar{g}_l(V(t)-E_l) \quad (18)$$

3.4 The compartmental neuron model

The cable equation previously described (see **Equation 6**) with their analytical solution for a dendrite morphology with a branching arbor of cables are only applicable under certain constraints. For instance, it is assumed that the dendrite diameter of the branches follows a power law of $d_{parent}^{3/2} = d_{child1}^{3/2} + d_{child2}^{3/2}$ (Rall, 1959, 1962). Then, the dendritic tree can be mapped to an electrophysiological equivalent (non-branching) cylinder of total length l. Later theoretical work has loosened these geometrical constraints to a certain degree but not completely (Rall and Rinzel, 1973; Goldstein and Rall, 1974). Additionally, for these calculations the dendrites were assumed to be passive and linear, i.e. currents sum linearly. In reality however, morphologies of dendrites come in a variety of shapes and sizes with complex branching patterns. Moreover, actual nerve cells contain several active properties and non-linearities in their dendrites, e.g. voltage-dependent ion channels. The model by Hodgkin & Huxley described above included a sodium, a potassium and a leak channel (mainly due to chloride). The biological complexity is even greater with neurons including dozens of different region-dependent ion channels. Together they result in a non-linear state equation in the shape of 18 which is not solvable by known functions and rules. In order to go beyond the theoretical constraints and to investigate realistic cell reconstructions it is useful to discretize the dendritic tree into multiple isopotential compartments. Within a compartment the various voltage-dependent ion channels contribute to the membrane

current (see $R-C$ unit in **Figure 1 C**). Each individual compartment of a dendrite segment is modeled by a typical cylinder of chosen length $L(x)$ (depending the desired resolution, **Figure 3**) and diameter d which connects with a specific resistance to any number of branching cylinders in the axial direction. Differences in these properties then lead to different potentials between the cylinders. The great advantage of such approach is the possibility to represent any dendritic tree and branching pattern with compartments of different sizes including various non-linearities. Examples of compartmental neuron modelling were developed by Rall (1964); Koch and Segev (1998) and were extended to computational software by Carnevale and Lebeda (1987). In this thesis, the NEURON environment from Carnevale *et al.* (1997) is employed to model the nerve cells.

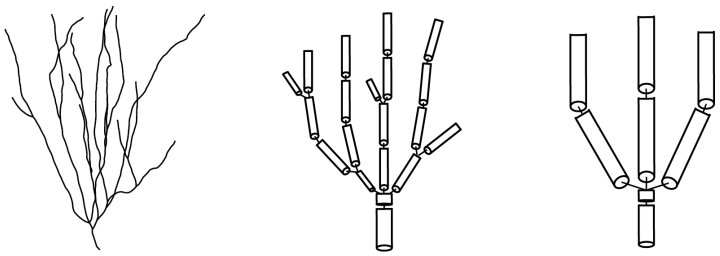

Figure 3. Discretized compartments as morphology representation
From left to right: Schematic of a granule cell (GC) reconstructed with a high number of segments (fine discretization) or low number of segments (coarse discretization). The more number of compartments used the more realistic the cell representation becomes but the more computation is necessary.

For example, a compartmental model of a neuron with just two compartments and two ion channels (sodium and potassium) obeys the **Equations 14** and **18**. In that case, the left side of the equation can be substituted with the axial current between the two compartments defined by the conductance between them, $g_{1,2}$. For the current from compartment 1 to 2 follows:

$$g_{1,2}(V_2 - V_1) = C_{m,1}\frac{dV_1}{dt}(t) + \bar{g}_K n^4(V_1(t) - E_K) + \bar{g}_{Na} m^3 h(V_1(t) - E_{Na}) + \bar{g}_l(V_1(t) - E_l) \quad (19)$$

Additionally, the compartments can include current contributions from the synaptic inputs with $g_{syn}(V,t)(V(t)-E_{syn})$. This equation can be solved numerically by computational models. The compartmental models employed in this thesis (Jarsky *et al.*, 2005 and Poirazi *et al.*, 2003b for PCs, Beining *et al.*, 2017 for GCs) are even more complex including various distance-dependent ion channels. Their implementation and application to investigate the IO function of hippocampal cells is described in detail in the **Methods** section.

3.5 Neurophysiological background: Cells, structure and connectivity of rodent hippocampus

The focus of this dissertation is on single cells and their IO function based in the rodent hippocampus. This includes cells from rats, but mainly from mice. The hippocampal structure in both species is similar. Typically in the rodent brain, the hippocampus is located in the medial region of the temporal lobe and is considered to play an essential role in memory and learning (Kogan *et al.*, 2000; Schimanski and Nguyen, 2004; Opitz, 2014). The general memory hypothesis states that the underlying neural mechanisms for information storage during learning and memory encoding in the brain are due to structural and synaptic changes at the cellular level, called plasticity (Martin *et al.*, 2000; Abraham *et al.*, 2019). The hippocampus in particular is considered to show a great capacity for plastic changes (Leuner and Gould, 2010). For instance, structural changes in the hippocampus occur throughout life and include neurogenesis, i.e. the creation of adult born (ab) cells (Barker *et al.*, 2011; Moreno-Jiménez *et al.*, 2019) with the formation of completely new connections between neurons. In addition to structural plasticity, the experience dependent synaptic plasticity (Snyder *et al.*, 2001) with its interplay between presynaptic and postsynaptic activity leading to changes in synaptic strength is involved in the hippocampal function. These plasticity mechanisms seem to follow rules based on the specific timing of pre- and postsynaptic AP firing. They include the so called spike-time-dependent-plasticity STDP (long-term-potentiation and long-term-depression LTP/LTD, Bliss and Lømo, 1973; Bliss and Collingridge, 1993; Neves *et al.*, 2008; Buchanan and Mellor, 2010; Bliss and Cooke, 2011) and homeostatic regulations such as metaplasticity rules (Abraham and Bear, 1996; Abraham *et al.*, 2001; Benuskova and Abraham, 2007). Episodic memory formation in the hippocampus (long term memory of events and feelings) necessarily consists of the encoding of space and time (Olton *et al.*, 1979; Eichenbaum, 2017; Ekstrom and Ranganath, 2018; Buzsáki and Tingley, 2018). This includes the notable discoveries of functionally specialized cell types (e.g. grid and place cells) as part of the entorhinal–hippocampal system (Moser *et al.*, 2015). It is apparent that the hippocampus is a widely studied brain area across several species (Eichenbaum *et al.*, 1992; Derdikman *et al.*, 2014). Nevertheless, its function is not fully understood yet.

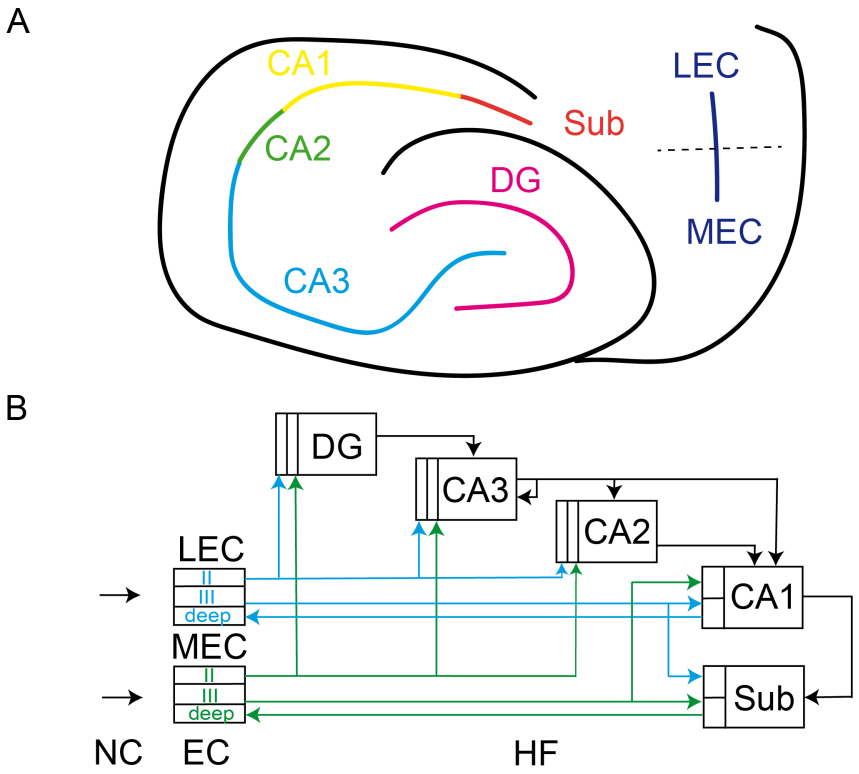

Figure 4. Neuroanatomical structure and connectivity of the rodent hippocampus
A, Schematic of a sagital slice through the rodent hippocampus including cornu ammonis with CA1 (*yellow*), CA2 (*green*), CA3 (*light blue*) and the Sub (*orange*) and DG (*pink*), as well as the EC with its medial (MEC) and lateral (LEC) part (*dark blue*), as described in Cutsuridis *et al.* (2019). **B**, Schematic of main connections (input) between CA1, CA2, CA3, DG and Sub (*black* arrows), between LEC and HF (*blue* arrows), as well as MEC and HF (*green* arrows), as described in Cutsuridis *et al.* (2019). Additionally, the EC receives input from the NC.

In addition to continuous changes due to memory formation within the hippocampus, the main structural organization and connectivity on a microcircuit level with its important input pathways and projections remain constant in a healthy animal. The rodent hippocampus, also known as the hippocampal formation (HF), consists of three main subregions, namely the dentate gyrus (DG), the hippocampus proper (CA1, CA2, CA3 with CA = ”Cornu Ammonis”) and the subiculum (Sub, see **Figure 4 A**), which are three-layered structures (Witter *et al.*, 2017; Cutsuridis *et al.*, 2019). In simple anatomical terms, these three hippocampal subregions form two ”C” shaped structures that are entangled with each other. To understand the HF and the hippocampal memory system, the neighboring area of the entorhinal cortex (EC) is equally important. The EC is mainly divided into a medial (MEC) and a lateral (LEC) part, which consist of six layers. The EC is the principal source of input to the HF. The wide neuronal

projections, called the perforant pathway, project to all subregions of the HF (**Figure 4 B**). Thereby, entorhinal layer II projects to the DG, CA2 and CA3, whereas layer III projects to CA1 and Sub. MEC and LEC reach proximal (e.g. middle third of DG molecular layer) or distal (e.g. outer third of DG molecular layer) laminar depths of the subregions, respectively. DG, CA2 and CA3 have no direct projections back to the EC. However, DG projects to CA3 (strong projection, DG cell axons to CA3 are called mossy fibers), while CA3 and CA2 project to CA1 (Schaffer collaterals pathway from CA3 to CA1) and CA1 in turn to Sub. Eventually, CA1 and Sub project back to the EC. In that indirect way, the connections to DG and CA3 return to the EC.

Not surprisingly, these structures are relevant for both the healthy memory function of the hippocampus as well as several neurological disorders (Anand and Dhikav, 2012). For example, alterations of the perforant pathway to DG and CA1 or the Schaffer collaterals pathway to CA1 can lead to dendritic atrophy during AD (Halliday, 2017; see also **Figure 5** *orange* cell example from Šišková *et al.*, 2014) or after lesions (Vuksic *et al.*, 2011) affecting the normal activity. Therefore, the focus of this dissertation is on these particular pathways for the cell input.

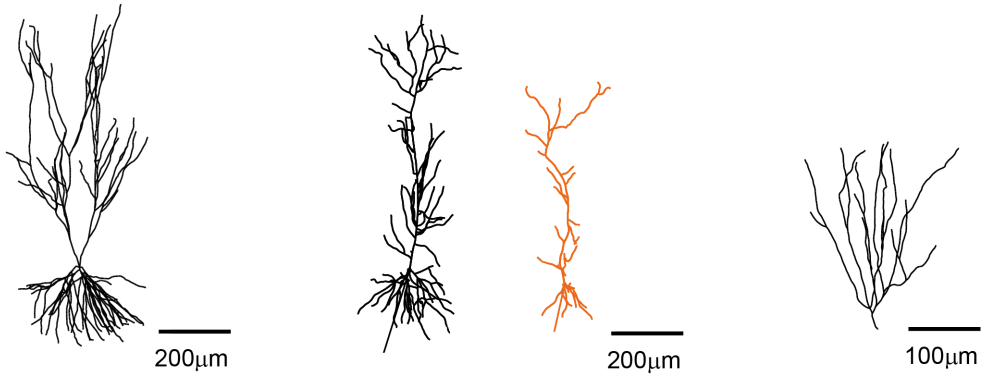

Figure 5. Examples of primary cells of the rodent HF used in this thesis
Left: Typical rat CA1 PC from *NeuroMorpho.Org* (Ascoli *et al.*, 2007), *Middle:* Reconstructed, healthy (*black*) and atrophied (*orange*) mouse CA1 PCs (Šišková *et al.*, 2014) and *Right:* Reconstructed mouse DG GC (Vuksic *et al.*, 2011).

Different brain regions typically contain different cell types. In general, the mammalian brain shows a strong heterogeneity of cells regarding type (Masland, 2004), morphology and physiology (compare e.g. the neuron database *NeuroMorpho.org*, Ascoli *et al.*, 2007). However, in the rodent hippocampus the main type of cell is excitatory (i.e. the probability of postsynaptic firing is increased). In particular, the CA regions consist predominately of pyramidal cells (PCs), which have a soma in the shape of a pyramid and two dendritic parts, the basal dendrites near the soma and the apical dendrites following one major apical branch (Bannister and Larkman, 1995; Megías *et al.*, 2001; Bloss *et al.*, 2016; see **Figure 5**, *left* and *middle*). The DG though mainly consists of GCs which are cone-shaped and smaller than PCs (Claiborne *et al.*, 1990; Schmidt-Hieber *et al.*, 2004, 2007; see **Figure 5**, *right*). In the overlapping area between DG and CA region (the hilus) one can find the mossy cells (MCs, Buckmaster *et al.*, 1996). In addition, inhibitory (i.e. the probability of postsynaptic firing is decreased) interneurons can be found in all regions but to a lesser degree. Neurological disorders can lead to pathological hippocampal cells displaying morphological changes such as dendritic atrophy for PCs (Šišková *et al.*, 2014; see **Figure 5**, *orange* cell example). A more detailed description of the cells employed in this thesis with regards to their morphology and electrophysiological features is given in the Method section, especially in comparison to pathological cells with intrinsic and extrinsic alterations.

3.6 Neurological disorder: Increased excitability in Alzheimer's disease

A prominent pathological cell development examined in chapter two of this dissertation is AD, a neurodegenerative disorder that affects memory and thought processes (Mittag *et al.*, 2023). The investigated cells are particularly from an early stage of the disease progression (Dickerson *et al.*, 2005; Busche and Konnerth, 2015) during which the AD-affected cells show dysfunction by increased excitability (hyperexcitability) and burst firing (Šišková *et al.*, 2014). This neuronal hyperexcitability is a well documented pathological hallmark of AD (Palop and Mucke, 2009; Vossel *et al.*, 2017; Zott *et al.*, 2018; Kazim *et al.*, 2021; Targa Dias Anastacio *et al.*, 2022), which has been observed in human patients (Palop *et al.*, 2007; Vossel *et al.*, 2013; Palop and Mucke, 2016; Horvath *et al.*, 2021; Ranasinghe *et al.*, 2022; Vossel *et al.*, 2021) as well as animal models such as the mouse (Busche *et al.*, 2008, 2012, 2015a,b; Rudinskiy *et al.*, 2012; Grienberger *et al.*, 2012; Scala *et al.*, 2015; Maier *et al.*, 2014; Šišková *et al.*, 2014; Hall *et al.*, 2015; Xu *et al.*, 2015; Liebscher *et al.*, 2016; Keskin *et al.*, 2017; Müller *et al.*, 2021) and the rat (Sosulina *et al.*, 2021). In hippocampal microcircuits of the mouse, the hyperactivity can reach epileptiform seizures and disruptions of neuronal activity (Palop *et al.*, 2007; Palop and Mucke, 2009; Born *et al.*, 2014; Vossel *et al.*, 2021) causing memory deficits.

Importantly, the focus of chapter two in this thesis will not only be on impaired IO function by increased excitability but on the change of firing mode towards stronger bursts with increased frequency. Shifts in firing mode and bursting patterns have been associated with amyloid-beta accumulation during AD (Chen, 2005; Minkeviciene *et al.*, 2009; Kellner *et al.*, 2014). Other neurological disorders such as stress (Okuhara and Beck, 1998) and epilepsy (Sanabria *et al.*, 2001; Wellmer *et al.*, 2002; Pothmann *et al.*, 2019) show similar burst increase.

An established mouse model of AD is the APP/PS1 model. Mice with the APP and PS1 human transgenes contain the APP Swedish mutation and PSEN1 with an L166P mutation. They lead to increased amyloid plaque deposition affecting the surrounding cells (Maia *et al.*, 2013) which is a hallmark of AD (Chen, 2005; Minkeviciene *et al.*, 2009). Experiments of APP/PS1 mice (*in vivo* and *in vitro*, patch-clamp and extracellular recordings) revealed hyperactivity of CA1 PCs with increased mean firing rate as well as enhanced bursting (Šišková *et al.*, 2014). The simulations of AD cells in chapter two of this thesis aim to numerically reproduce the data by Šišková *et al.*, 2014, see **Table 1**. Their main prediction was that denervated and therefore smaller cells would have a higher input resistance and therefore increased excitability. The

modelling of AD in this dissertation complements the modelling by Šišková *et al.* (2014) with more realistic synaptic activation comparing effects of the denervated APP/PS1 cells together with other AD related changes to generally show possible mechanisms of hyperexcitability (described and published in Mittag *et al.*, 2023).

Table 1. Single spikes, bursts and triplets in *in vivo* whole-cell patch-clamp recordings from CA1 PCs in WT and APP/PS1 mice (from Figure 1 B by Šišková *et al.*, 2014). Reproduced from "Modelling the contributions to hyperexcitability in a mouse model of Alzheimer's disease" (doi: https://doi.org/10.1113/JP283401) by Mittag M, Mediavilla L, Remy S, Cuntz H, Jedlicka P and licensed under CC BY 4.0 (Copyright Mittag *et al.*, 2023, http://creativecommons.org/licenses/by/4.0/).

	Singlets (1AP)	**Bursts (>1AP)**	**Triplets (3AP)**
mean value μ_{WT} (Hz)	1.54	0.84	0.16
SEM_{WT}	0.43	0.22	0.04
mean value $\mu_{APP/PS1}$ (Hz)	1.47 n.s.	2.06 s.	0.60 s.
$SEM_{APP/PS1}$	0.51	0.31	0.10

s./n.s. = significant/not significant
Note predominantly burst firing vs. solitary firing in APP/PS1 vs. WT mice, respectively.

There are three major explanations of neuronal hyperexcitability due to alterations in AD currently found in the literature (Ferrao Santos *et al.*, 2010; Zott *et al.*, 2018; Vyas *et al.*, 2020; Maestú *et al.*, 2021; Targa Dias Anastacio *et al.*, 2022): alterations of intrinsic properties by dendritic degeneration or by ion channel changes, or alterations of extrinsic network properties by enhanced synaptic excitation-inhibition (E/I) ratio. These three possible explanations are described below in more detail (see also Mittag *et al.*, 2023).

3.6.1 Morphological changes

A major pathological characteristics of AD is the dendritic structural degeneration of the neurons (Braak and Braak, 1991; Braak *et al.*, 1993; Anderton *et al.*, 1998). It has been shown in humans (Augustinack *et al.*, 2002; Grutzendler *et al.*, 2007; Merino-Serrais *et al.*, 2013) and in animal models (Grutzendler *et al.*, 2007; Le *et al.*, 2001; Tsai *et al.*, 2004; Moolman *et al.*, 2004). Thereby, the progression of AD-related degeneration can be found in areas of the brain (HF with DG, CA1 and Sub) that are important for cognitive functions such as learning and memory (Spires and Hyman, 2004; Grutzendler *et al.*, 2007; Adlard and Vickers, 2002; Falke *et al.*, 2003; Geula *et al.*, 1998). Alterations in morphology with a simultaneous decline in synapse number have previously been linked to AD development (Terry *et al.*, 1991; Masliah

et al., 1994; Cochran *et al.*, 2014). However, the consequences for cell function as a result of these changes are unclear. On the one hand, for APP/PS1 mouse model cells a recent study has suggested that dendritic degeneration in CA1 PCs can potentially lead to enhanced excitability, i.e. increased somatic firing rates due to stronger and more bursting (Šišková *et al.*, 2014). An explanation might be the lower input conductance in a shrunken cell suffering from dendritic degeneration. On the other hand, the known synaptic loss in AD cells might lead to less excitation and therefore counter exactly the excitability increasing effect of the dendritic degeneration; as a result the original excitability is maintained as a form of homeostasis (Platschek *et al.*, 2016, 2017; Cuntz *et al.*, 2021; Mittag *et al.*, 2023). Hence, the AD related loss of synapses and dendritic degeneration are implemented at the same time in this thesis.

3.6.2 Ion channel changes

The pathological development of AD has been associated with alterations in the intrinsic excitability with respect to ion channel contributions (Kerrigan *et al.*, 2014). Previous experiments have shown changes in channel densities in AD cells, such as A-type K^+, voltage-gated Na^+ and delayed-rectifier K^+ channels (Good *et al.*, 1996; Kim *et al.*, 2007; Brown *et al.*, 2011; Scala *et al.*, 2015; Liu *et al.*, 2015; Wang *et al.*, 2016; Ghatak *et al.*, 2019). For instance, for the A-type K^+ current a reduction in channel expression linked to enhanced excitability has been observed in AD cells (Chen, 2005; Morse *et al.*, 2010; Culmone and Migliore, 2012; Scala *et al.*, 2015; Hall *et al.*, 2015; Frazzini *et al.*, 2016; Rodrigues *et al.*, 2017). Further experimental findings have revealed the influence of the small and large calcium-activated K^+ channels in AD mouse models (Beck and Yaari, 2008; Zhang *et al.*, 2014; Wang *et al.*, 2015a,b). Also the disruption of Ca^{2+} signaling and Ca^{2+} channels plays an important role in the pathogenesis of AD (Bezprozvanny and Mattson, 2008; Bojarski *et al.*, 2008; Anekonda *et al.*, 2011; Tan *et al.*, 2012). For AD-related pathologies the L-type Ca^{2+} channel (Anekonda *et al.*, 2011; Berridge, 2014), the A-type K^+ channel (Chen, 2005) and Na^+ channels (Wang *et al.*, 2016; Ghatak *et al.*, 2019; Müller *et al.*, 2021) have been shown to be involved in burst rate amplification. Modelling studies (Medlock *et al.*, 2018; Garg *et al.*, 2021; Mittag *et al.*, 2023) confirm the role of channels for enhanced burst firing. Evidently, the modification of intrinsic excitability due to alterations in ion channel expression is well documented in AD. It is important to note that the effect of every ion channel, on its own and together, on AD development and particularly hyperexcitability is currently unknown. For example, previous studies concerning the

hyperpolarisation-activated H channel show unclear results, i.e. depending the experiment the channel density was lower or higher in AD cells compared to control cells (Musial *et al.*, 2018; Vitale *et al.*, 2021). The interplay of channel alterations with additional synaptic and dendritic changes is investigated in this thesis (see also Mittag *et al.*, 2023).

3.6.3 External network changes

Previous research on AD has further shown alterations in the E/I ratio due to increased glutamatergic excitation (Busche and Konnerth, 2016; Zott *et al.*, 2019) as well as impaired inhibition (Busche *et al.*, 2008, 2012; Takahashi *et al.*, 2010; Schmid *et al.*, 2016; Palop and Mucke, 2016; Ambrad Giovannetti and Fuhrmann, 2019; Xu *et al.*, 2020; Gervais *et al.*, 2022; Ruiter *et al.*, 2020; Melgosa-Ecenarro *et al.*, 2022). Especially, changes in the perisomatic inhibition are noteworthy (Verret *et al.*, 2012) as they can alter the firing pattern towards more bursts (Pouille and Scanziani, 2004). The excitatory drive constitutes one of the main determinants of neuronal firing rate (Frere and Slutsky, 2018). A shift towards synaptic excitation (Roberson *et al.*, 2011) that increases the E/I ratio may therefore explain enhanced firing rates in AD during spontaneous activity. Epileptiform disruption of spontaneous neuronal activity in hippocampal circuits is a typical feature in mouse models of AD (Palop *et al.*, 2007), where sharp synchronous discharges linked to memory deficits have been observed (Born *et al.*, 2014). In line with the relevance of enhanced E/I ratio, recent clinical observations suggest that pharmacological suppression of glutamatergic excitation (by levetiracetam) is a promising way of improving cognition in AD patients with epileptiform hyperexcitability (Vossel *et al.*, 2021). CA1 pyramidal neurons are part of a larger network and receive input from CA3 and the EC. Previous studies have shown hyperactivity in EC for AD pathology models of mice (Khan *et al.*, 2013; Angulo *et al.*, 2017; Petrache *et al.*, 2019) as well as CA3 (Kazim *et al.*, 2017; see also computer AD models containing CA1 and CA3 Świetlik *et al.*, 2019). An increased excitatory network activity in these pre-synaptic areas could therefore spread to CA1 and contribute to the observed hyperexcitability and burstiness in AD cells (Mittag *et al.*, 2023).

Although these three groups of mechanisms have been proposed to account for AD-related hyperexcitability, their contributions and mutual interplay are not fully understood. Therefore, this dissertation takes advantage of the unique feature of biophysical modelling that enables the investigation of isolated and combined parameter changes. The computational approach

allows the possibility to disentangle which changes and their contributions to hyperexcitability in AD are most relevant (Mittag *et al.*, 2023).

3.7 Hippocampal granule cell function: Pattern separation and economy

3.7.1 Pattern separation and information processing

The hippocampus is a brain region associated with encoding memory. One type of memory is spatial navigation which depends strongly on pattern separation. Several experimental studies confirm the potential role of dentate GCs in pattern separation (Leutgeb *et al.*, 2007; Bakker *et al.*, 2008; Neunuebel and Knierim, 2014; Yassa and Stark, 2011; Chavlis and Poirazi, 2017). Thereby, pattern separation is the ability of the GCs to transform similar synaptic inputs into less similar somatic outputs as IO function. In this dissertation, it is investigated how the GC pattern separation function together with energy constraints depends on the underlying biophysical modelling. By comparing the input patterns with the output patterns, a pattern separation measure can be calculated.

Traditional theoretical measures of pattern separation include the reduction in similarity between input and output spike time patterns in the DG (Bird *et al.*, 2024), e.g. orthogonalisation (Marr, 1969; Rolls, 2013) or decorrelation (Madar *et al.*, 2019; Guzman *et al.*, 2021). An increased measure of the distance (e.g. Hamming or Wasserstein) between spike trains is another common way of quantifying the degree of pattern separation (Chavlis *et al.*, 2017). Often these measures include the idea that an increase in sparsity is beneficial for pattern separation. However, it has been shown that increased sparsity in its extreme can lead to a loss of information to the point of a destroyed pattern (Santoro, 2013; Vineyard *et al.*, 2016; Chavlis and Poirazi, 2017; Bird *et al.*, 2024). It seems apparent that a more complete pattern separation measure should therefore include a measure of information content as well. Information as a mathematically describable quantity had been introduced by Shannon (1948). Existing attempts to involve information calculations while investigating the function of the hippocampus still look at both measures, information and pattern separation, separately (Faghihi and Moustafa, 2015; Vineyard *et al.*, 2016). Only recently it has been proposed to directly include information theoretic concepts such as mutual information (MI) or redundancy, that also measure the information content of the input and output spike trains, for the calculation of

the pattern separation function (Bird *et al.*, 2024). Originally, according to Shannon (1948), the expected information $I(X)$ in *bits* of a random variable X can also be called uncertainty or entropy $H(X)$. It is dependent on the probability p (between 0 and 1) of its potential values and defined in the following:

$$H(X) = \mathbb{E}[I(X)] = \mathbb{E}[log_2(\frac{1}{p(X)})] = \mathbb{E}[-log_2 p(X)] = -\sum_{x \in X} p(x) log_2 p(x) \tag{20}$$

Furthermore, the MI of $I(X, Y)$ between variables X and Y measures the decrease of uncertainty over Y by knowing about X or vice versa (Shannon, 1948):

$$I_{(X,Y)} = H(X) - H(X \mid Y) = H(Y) - H(Y \mid X) \tag{21}$$

With $H(X \mid Y)$ being the conditional entropy and with Bayes' rule this yields:

$$I_{(X,Y)} = \sum_x \sum_y p_{(X,Y)}(x, y) log_2 \left(\frac{p_{(X,Y)}(x, y)}{p_{(X)}(x) p_{(Y)}(y)} \right) \tag{22}$$

Here, $p(X, Y)$, $p(X)$ and $p(Y)$ are the joint and marginal distributions respectively. For independent X and Y, $I_{(X,Y)}$ equals 0. This can be applied to neural spike trains with input and output patterns X and Y. For a combined measure of pattern separation and information theory this MI is weighted with the number of spikes m_x and n_y of X and Y to give:

$$\Upsilon_M = \frac{m_x - n_y}{m_x} I_{(X,Y)} \tag{23}$$

Next, the redundancy R_X within input spike trains X is considered as the minimum MI between any part or single train x_i and the rest of the ensemble $X \backslash x_i$ (Williams and Beer, 2010):

$$R_X = \min_{x_i} \sum_{x \in X \backslash x_i} \left(\sum_{y \in x_i} p_{(X \backslash x_i, x_i)}(x, y) log_2 \left(\frac{p_{(X \backslash x_i, x_i)}(x, y)}{p_{(X \backslash x_i)}(x) p_{(x_i)}(y)} \right) \right) \tag{24}$$

The same holds for the output spike trains Y to calculate R_Y. Relative redundancy reduction as a new measure for pattern separation then means to compare both redundancies and weigh them with the MI of $I(X, Y)$:

$$\Upsilon_R = (R_X - R_Y) I_{(X,Y)} \tag{25}$$

In this dissertation, the *Matlab pattern_separation_toolbox* (Bird *et al.*, 2024; see also Eqns. 1, 3, 14 and 16 there) combining information theoretical aspects and traditional distance measures is used to calculate a robust pattern separation quantity in the DG. Thereby, the marginal and joint distributions of the input and output patterns are evaluated. They are detailed in the **Methods** section.

3.7.2 Pareto optimality of economy and function

The function of a neuron mostly involves the electrical response of it in the form of a specific dendritic or somatic potential or firing rate. Such function demands material and energy, e.g. ions have to be transported in and out the cell (Attwell and Laughlin, 2001; Harris *et al.*, 2012). However, naturally their exists only a limited supply of material and energy for a cell at a given moment. The cell is put under a constraint, or in other words, has to find an optimal solution for multiple objectives (Laughlin and Sejnowski, 2003). The neuron can either maximize the function or minimize the material and energy consumption. Multiple tasks present a problem, because it is not possible to be optimal at all tasks simultaneously and hence compromises are necessary. The nerve cell consequently shows trade-offs when performing multiple tasks. Recent studies on Pareto optimality (Szekely *et al.*, 2013; Jedlicka *et al.*, 2022) show that it can be a helpful tool to determine conditions for the best performance of a neuron with multiple tasks and trade-offs, e.g. low energy consumption, defined as high economy, while showing high functionality with as little impairment of either as possible (Yu and Yu, 2017; Remme *et al.*, 2018). The Pareto approach can facilitate the search for optimal solutions by filtering the parameter space of conditions and introducing a geometrical perspective (Alon, 2006; Shoval *et al.*, 2012; Sheftel *et al.*, 2013). The Pareto principle reduces the parameter space of a neuron by removing sub-optimal parameter sets and keeping the parameter sets with an optimal trade-off. At the same time, the feature or performance space of the relating tasks is reduced to a low-dimensional hyperspace of Pareto optimal solutions, the so called Pareto front. A neuron is called Pareto optimal in performance space as well as parameter space when no other neuron can outperform it in all tasks at the same time (Szekely *et al.*, 2013; Jedlicka *et al.*, 2022); the improvement in one task would mean an impairment in another task. By comparing the performance of all possible neurons and applying the Pareto optimal criterion the Pareto front is constructed. For two tasks the Pareto front necessarily is a line which connects both tasks, no matter how many parameters are involved in the optimization.

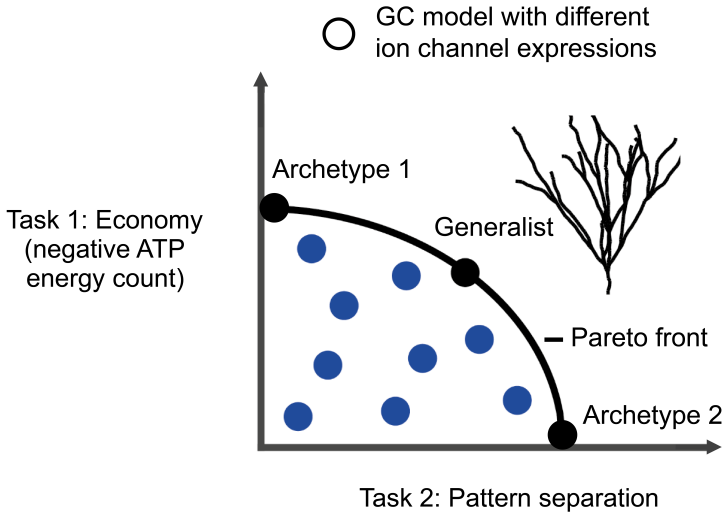

Figure 6. Pareto optimality in performance space for two competing tasks of economy and pattern separation for GCs

Different conditions (e.g. various ion channel configurations in GCs, *circles*) potentially lead to varying performances of the desired tasks (e.g. economy and pattern separation). Optimal conditions cannot be outperformed in all tasks at the same time. They are called Pareto optimal and constitute the Pareto front (*black line*, Jedlicka *et al.*, 2022). The Pareto front is a barrier beyond which by definition no possible solution exists. Extremes favouring one task in particular are called archetypes, other solutions in between and on the front are called generalists.

Figure 6 shows an example of the overall Pareto front (*black*) for the two-task optimisation of economy and pattern separation performance. The different models (*circles*) arise for different parameters of the biophysical features, i.e. ion channel expressions. In this dissertation, the two tasks of energy economy and pattern separation function for dentate GCs are compared for a population of models.

3.7.3 Neurogenesis in the hippocampus

The GCs of the DG, individually and in their integrated network, undergo changes during their lifetime. In this dissertation, for instance, the important process of adult neurogenesis is considered and its effect on excitability and IO function is investigated (Jessberger and Kempermann, 2003; Kempermann *et al.*, 2004). Adult neurogenesis in the DG entails the continuous creation of new GCs (= abGCs) which show different electrophysiological charateristics and increased excitability as well as plasticity (Schmidt-Hieber *et al.*, 2004; Ge *et al.*, 2007; Mongiat *et al.*, 2009; Beining *et al.*, 2017; Doan *et al.*, 2019). Importantly, only few brain areas exhibit neurogenesis. Besides the DG of the hippocampus, it was found to occur also in the lateral subventricular zone, an important area for olfactory function especially in rodents (Alvarez-Buylla and Garcıa-Verdugo, 2002). In humans and other mammals, it is debated if neurogenesis is a lifelong process or possibly stops at some point, which would have severe effects on hippocampal function (Kuhn *et al.*, 1996; Kempermann *et al.*, 2015). In particular, the importance of abGCs is manifested in their functional role in memory formation including pattern separation in the hippocampus (Clelland *et al.*, 2009; Johnston *et al.*, 2016). Impaired neurogenesis therefore is linked to neurological disorders, such as AD and stress, affecting the memory function (Gould and Tanapat, 1999; Moreno-Jiménez *et al.*, 2019). On the good side, neurogenesis can be stimulated and as a result improve function again (Van Praag *et al.*, 1999; Gould *et al.*, 1999). Clearly, neurogenesis is an important process in the brain. However, how newly formed GCs are integrated in the memory and pattern separation function is not fully understood yet (Kempermann, 2002; Lopez-Rojas and Kreutz, 2016; Johnston *et al.*, 2016).
In chapter three of this dissertation, the physiological changes in the DG due to neurogenesis on a single cell level are investigated, particularly the integration of new GCs with regard to their pattern separation performance under energy constraints.

3.8 Scope of the thesis and research questions

The overall aim of this dissertation is to get a deeper understanding of the dependence of the IO relationship in hippocampal nerve cells on dendritic structural differences and intrinsic ion channel mechanisms between neuron morphologies. Therefore, the focus of this dissertation is on finding underlying principles and mechanisms at the intersection of morphological and biophysical compartmental modelling with respect to IO function of hippocampal nerve cells including the polar perspectives of optimal and pathological conditions. This is represented in the three major, complementary investigations in this dissertation.

In chapter one, I investigate the general principle of "dendritic constancy" for several well-known active compartmental models of PCs. It has been shown previously that there exists a passive backbone of equalising neuronal activity independent of dendrite morphology (i.e. dendrite size and shape) under the condition of distributed synaptic activation, called dendritic constancy (Cuntz *et al.*, 2021). However, it is unclear if the dendritic constancy principle holds for more realistic, active models with voltage-dependent ion channels as well. The goal in the first chapter therefore is to test the length- and morphology-invariance in realistic biophysical models. To that end, I implement two compartmental models, namely by Poirazi *et al.* (2003b) and Jarsky *et al.* (2005). Specifically, non-linearities are added to the models such as NMDA synapses and realistic, heterogeneous synaptic weight distributions to examine the robustness of the IO function. In addition to distributed (nonclustered, whole cell) synapse placement, also clustered synapses are added and investigated. Finally, in order to test the generalisation of the dendritic constancy claim, I implement a third compartmental model by Almog and Korngreen (2014) describing cortical PCs. In all conditions in the first chapter, I examine the activity of nerve cells with respect to their dendritic length independence, according to dendritic constancy.

In chapter two, I apply the dendritic constancy principle to pathological cells. In particular, I investigate the enhanced activity (hyperactivity) in an Alzheimer's disease (AD) model in mouse CA1 PCs. It is known, that AD can lead to both, hyperactivity and dendritic atrophy. In this second chapter, I therefore aim to answer the question if there is a causal link between both pathological features. Again, I employ the two compartmental models by Poirazi *et al.* (2003b) and Jarsky *et al.* (2005) from chapter one to perform the simulations. Three major input pathways are investigated separately to check for selective gating of layer-

specific input. Moreover, other intrinsic and extrinsic mechanisms and possible contributors to the AD-related hyperactivity that have been observed in the literature are investigated. In summary, in the second chapter of this thesis I study four distinct modifications of the nerve cells (and their combinations) that may contribute to enhanced firing and bursting: morphological changes (dendritic degeneration), increased network activity that leads to an increased burst input to the neuron, increased excitation to inhibition ratio due to less inhibitory input and concomitant increased network activity via upregulated excitatory input frequency, and intrinsic alterations of the ion channel contributions.

In chapter three, I extend the investigation of the cell function further to the GCs of the DG. The goal is to include information-theoretical and pattern separation measures as well as energy constraints when comparing the IO function of the cells. I use the concept of Pareto optimality to analyse the performance of both pattern separation and economy at the same time as a two-task optimisation problem. To perform the simulations, I implement a compartmental GC model based on Beining *et al.* (2017). It is compared to a population of GC models with varied ion channel compositions but similar somatic behaviour, in line with the concept of degeneracy. In addition, in this third chapter I examine newly formed, abGCs containing intrinsic (ion channel) and extrinsic (synaptic input) alterations compared to the mature and already integrated GCs. Finally, I investigate the underlying mechanisms that influence the optimisation of the IO function of the GCs. The results reveal that the overlap of the potassium and sodium currents play an important role for economy and pattern separation performance.

4 Materials and Methods

The Methods section describes how I investigated the research questions of this dissertation with computational models and what simulations I subsequently performed with them in detail. First, an overview of the morphological data sets employed in each chapter of this thesis is given in 4.1. The reconstructed cells had to undergo some form of manipulation before being usable. The ensuing section 4.2 then gives a specification of how the active ion channel models (four models in total) were inserted into the morphologies. These models depend on the cell type and differ in complexity. They constitute the core modelling part of this dissertation to answer the question of how IO function is affected in particular hippocampal nerve cells. The focus is thereby on realistic synaptic activation. It is described in detail for all three chapters of the thesis in the following section 4.3. For chapter two, intrinsic (ion channel expression) and extrinsic (E/I relation) conditions were manipulated for plausibly explaining hyperexcitability in AD PCs. Hence, all modifications are described in section 4.4. In the final sections (4.5 and 4.6) ATP calculations are derived to asses the energy economy of the cells and a pattern separation measure is applied to the cells to assess their function. Both quantitative measures are important tools for the third chapter to investigate the cells' multi-objective performance.

Morphological analysis was performed in Matlab (Mathworks Inc, version 2018a) using the software package of the TREES toolbox (Cuntz *et al.*, 2011; `www.treestoolbox.org`). All passive and active compartmental model simulations were run in NEURON (Hines and Carnevale, 2004) via a newly developed software to control NEURON with Matlab and the TREES toolbox, the TREES-to-NEURON (T2N) interface (Beining *et al.*, 2017).

4.1 Morphological models

In chapter one of this thesis, reconstructions of rat hippocampal PC morphologies ($n = 105$, examples in **Figure 7 A**) from *NeuroMorpho.Org* (Ascoli *et al.*, 2007) were used, that were of sufficient quality. This entails a complete profile in morphological diameters and enough information in the z-dimension (with no abrupt jumps). After applying these criteria the dendrite diameters were normalised to $1\mu m$ (local diameter divided by total average diameter). To generalize the claim, cortical rat PCs were included with another active biophysical model by Almog and Korngreen (2014). The reconstruction data set ($n = 20$, examples in **Figure 7 B**) from Korngreen available on *NeuroMorpho.Org* was used.

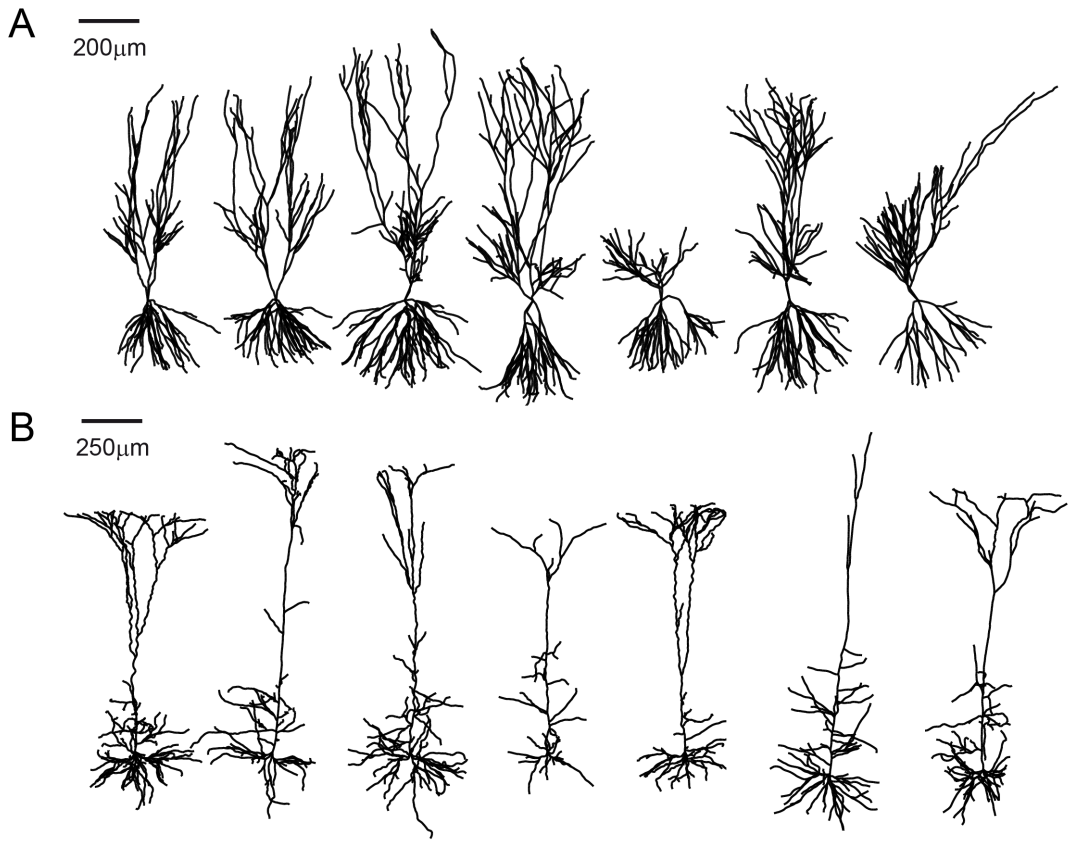

Figure 7. Rat hippocampal and cortical PC dendrite reconstructions used in chapter one
A, Seven example reconstructions of rat hippocampal PC morphologies ($n = 105$ in total) from *NeuroMorpho.Org* (Ascoli *et al.*, 2007). **B**, Seven example reconstructions of rat cortical layer five (L5) PC morphologies ($n = 20$ in total) from *NeuroMorpho.Org* (Ascoli *et al.*, 2007).

In chapter two of this thesis, a data set that included 59 mouse hippocampal CA1 PC morphologies from 10-14 months old WT ($n = 31$) and APP/PS1 ($n = 28$) mice was employed (Šišková *et al.*, 2014). The 3D reconstructions were loaded into Matlab and rigorously reviewed to exclude graphical artefacts and unrealistic morphological inconsistencies. The morphologies therefore had to be prepared before analysis: unrealistic nodes and trifurcations were removed (`repair_tree`, `clean_tree`) and corrected for abrupt shifts in the z-axis (`zcorr_tree`, `smooth_tree`). Separated partial trees of basal and apical regions were concatenated. To map discretised compartments to the original morphology reconstructions, all compartmental nodes were distributed to have equal distance of $1\mu m$ for a high spatial resolution (`resample_tree`). The diameter distribution of the dendrites in each morphology was adjusted to follow realistic values and account for the lack of diameter information in the original data. Therefore the dendrites were tapered (quadratic taper: `quadfit_tree`, `quaddiameter_tree` as in Cuntz *et al.*, 2007). As shown in Mittag *et al.* (2023) and in **Figure 8** statistical comparison of average dendritic path length (WT $5.19 \pm 1.75mm$, APP/PS1 $4.00 \pm 1.22mm$, $p = 0.00380$), number of branching points (WT 52.16 ± 17.79, APP/PS1 41.61 ± 11.67, $p = 0.0100$) and dendrite surface area (WT $0.026 \pm 0.008mm^2$, APP/PS1 $0.02 \pm 0.007mm^2$, $p = 0.00708$) between WT and APP/PS1 model cell groups displayed significant differences. In contrast, the average dendritic diameter was equal for both cell groups (WT $1.6 \pm 0.24\mu m$, APP/PS1 $1.57 \pm 0.23\mu m$, $p = 0.603$). This value is unrealisticly high as PCs typically depict an average dendritic diameter of $0.8\mu m$ (Benavides-Piccione *et al.*, 2020). Consequently, the dendrites were normalized to a reduced average diameter of $1\mu m$ (Cuntz *et al.*, 2021). An artificial cosine shaped soma was added to the dendrites as none of the reconstructions included an original soma. The soma compartments had a surface area of $560\mu m^2$ ($\approx 4 \cdot 137\mu m^2$, which is the soma perimeter) and a maximum diameter of $10\mu m$, corresponding to the typical average size of somata in pyramidal neurons (Benavides-Piccione *et al.*, 2020). An artificial axon was created as well. It consisted of cylindrical compartments totaling a length of $630\mu m$ with an average diameter of $0.5\mu m$. The axon hillock, initial segment, five nodes of Ranvier and myelination were specific sections included in the axon (Benavides-Piccione *et al.*, 2020).

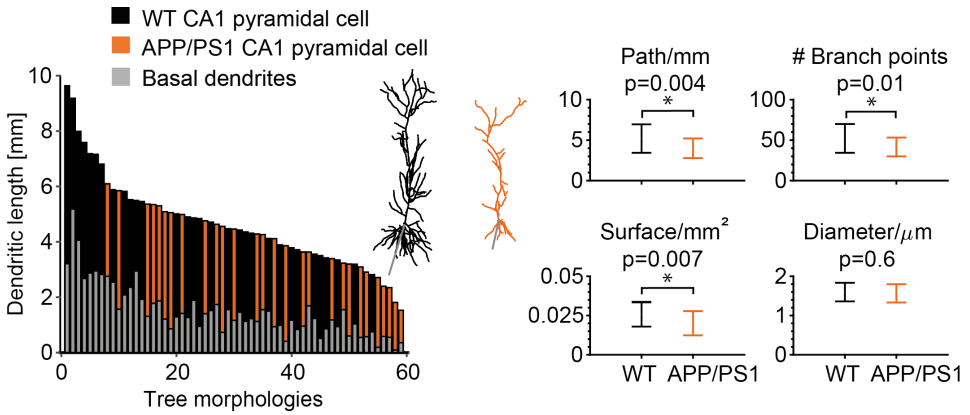

Figure 8. Reconstructed WT and APP/PS1 CA1 mouse PCs and their morphological measures
Reproduced Figure 1 A from "Modelling the contributions to hyperexcitability in a mouse model of Alzheimer's disease" (doi: https://doi.org/10.1113/JP283401) by Mittag M, Mediavilla L, Remy S, Cuntz H, Jedlicka P and licensed under CC BY 4.0 (Copyright Mittag *et al.*, 2023, http://creativecommons.org/licenses/by/4.0/): *Left*, sorted distribution of the dendritic length of all reconstructed PCs (Šišková *et al.*, 2014). *Black* denotes the WT cell, *orange* the APP/PS1 cell and *grey* is the basal portion. *Right*, the comparison of average dendritic path length, number of branching points and dendrite surface area shows significant differences depicted by the asterisks.

Most published cell models have been created by inserting ion channels into just one specific cell. However, one of the tasks of this thesis was to investigate the effect of morphological differences of many cells. In order to apply ion channel models for various morphologies of different sizes and shapes, the passive and active mechanisms must be distributed in a coherent manner. Therefore boundaries for the anatomical layers of the hippocampus and regions of the dendritic tree, in which the ion channels are embedded, had to be defined in a normalised way. Accordingly, the layers stratum oriens (SO), stratum radiatum (SR) and stratum lacunosum-moleculare (SLM) comprised 40%, 40% and 20% of the cell's dendritic length (Bannister and Larkman, 1995; Trommald *et al.*, 1995; Megías *et al.*, 2001). Below the SO/SP axis reside the basal dendrites, above the apical dendrites. Within the apical dendrites the dendritic portion between SO/SP boundary and SR/SLM limit was $2/3$ of the total apical length. Important points for distance dependent electrotonic properties and active channels along the somato-dendritic axis are present at approximately 8% (proximal SR), 48% (middle SR), 67% (distal SR, same as the SR/SLM boundary) and 85% of total apical length (based on experiments from Carnevale *et al.*, 1997; Pyapali *et al.*, 1998; Megías *et al.*, 2001; Golding *et al.*, 2005; Bezchlibnyk *et al.*, 2017; found on *NeuroMorpho.Org*). Branches with a majority of nodes below the SR/SLM boundary were part of the trunk subregion for the main apical dendrite or

peritrunk/oblique with further orthogonal distance to the trunk (after $50\mu m$). Branches with most nodes above the SR/SLM limit were part of the tuft.

The data used in chapter three of this research thesis came from $2-4$ months old $C57BL/6$ mice ($n = 8$, Schmidt-Hieber *et al.*, 2007) and $11-12$ months old adult male $Thy1-GFP$ transgenic mice ($n = 15$, Vuksic *et al.*, 2011) as shown in **Figure 9** A and B respectively. The compartmental model by Beining *et al.* (2017) was implemented for the mature GCs (mGCs). An altered model version was used for the newborn GCs (same morphologies with modified channel expression and synaptic connectivity). The abGCs are highly dynamic in their dendritic structure during maturation. Between $4-6$ weeks after birth the total dendritic length stabilises and the cells show increased plasticity (Ge *et al.*, 2007; Kim *et al.*, 2012). At around 8 weeks they are fully matured and integrated in the GC network. Therefore, the time period considered here in the thesis for abGCs is between $4-8$ weeks from birth. The GCs from the Schmidt-Hieber lab had reconstructions that contained dendrites, somas and axons. The GCs from the Vuksic lab however only contained reconstructed dendrites and somas. For that reason, the same example axon coming from the Schmidt-Hieber data was accordingly attached to all dendrites from the Vuksic data set. GCs typically show a layered structure (granule cell layer and inner-, middle- and outer molecular layer) which was added to all cells according to Beining *et al.* (2017). This is important to insert region dependent ion channel densities. Finally, similar as in part one and two of the thesis for PCs, also the GCs were normalised to $1\mu m$ regarding the average dendritic diameter.

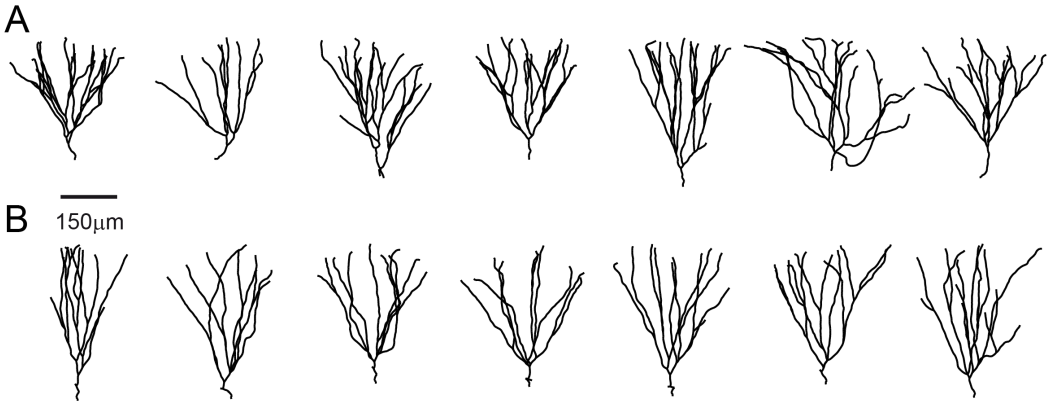

Figure 9. Mouse hippocampal GC dendrite reconstructions used in chapter three

A, Seven example reconstructions of mouse hippocampal GC morphologies ($n = 8$ in total) from Schmidt-Hieber *et al.* (2007). **B**, Seven example reconstructions of mouse hippocampal GC morphologies ($n = 15$ in total) from Vuksic *et al.* (2011).

4.2 Compartmental cell models

4.2.1 CA1 models by Poirazi et al. and Jarsky et al.

First, a biophysically realistic model based on the model developed by Poirazi *et al.* (2003b,a) was implemented (see model #20212 in ModelDB Hines and Carnevale, 2004; McDougal *et al.*, 2017) and ported to T2N as in Cuntz *et al.* (2021) and Mittag *et al.* (2023). The model by Poirazi consisted of active and passive membrane mechanisms. In total, it included 16 different ion channels which were mostly heterogeneously distributed with dendritic distance to soma (see region dependence in **Figure 10** A and C). The maximum length of the apical trunk of the original cell model by Poirazi was $423.75\mu m$, a point at which the conductance values of the distance dependent channels reached a maximum. According the subregion devision above, this value was different for each of the reconstructed cells. Every individual cell received a rescaled channel distribution in order to have a distance relation of the channel conductances that would lead to identical channel densities at the beginning (soma) and end (tuft) of the apical depth compared to the original cell (**Figure 10 B**). The division of the dendritic tree into subregions necessary for channel distribution followed the typical regions in PCs: basal dendrites, soma, trunk, apical dendrites (oblique, peritrunk, tuft) and axon.

Second, a further CA1 PC model by Jarsky *et al.* (2005) was implemented (see model #116084 in ModelDB and the publications Cuntz *et al.*, 2021 and Mittag *et al.*, 2023). The properties consist of homogeneous passive parameters for the whole cell and four active ion channels, namely a voltage-gated sodium conductance, a delayed-rectifier potassium conductance and a proximal and distal A-type potassium conductance (increased half-inactivation voltage). Both A-type potassium conductances followed a channel distribution depending on apical path distance from the soma with a maximum conductance in the tuft that was six times higher than in the soma (**Figure 11**). Therefore, different morphologies had a different slope of the ascending channel distribution which was rescaled in a similar manner as the distance dependent channels in the model by Poirazi *et al.* (2003b) as described above. The sodium and delayed rectifier conductances however had a simple homogeneous distribution with low excitability.

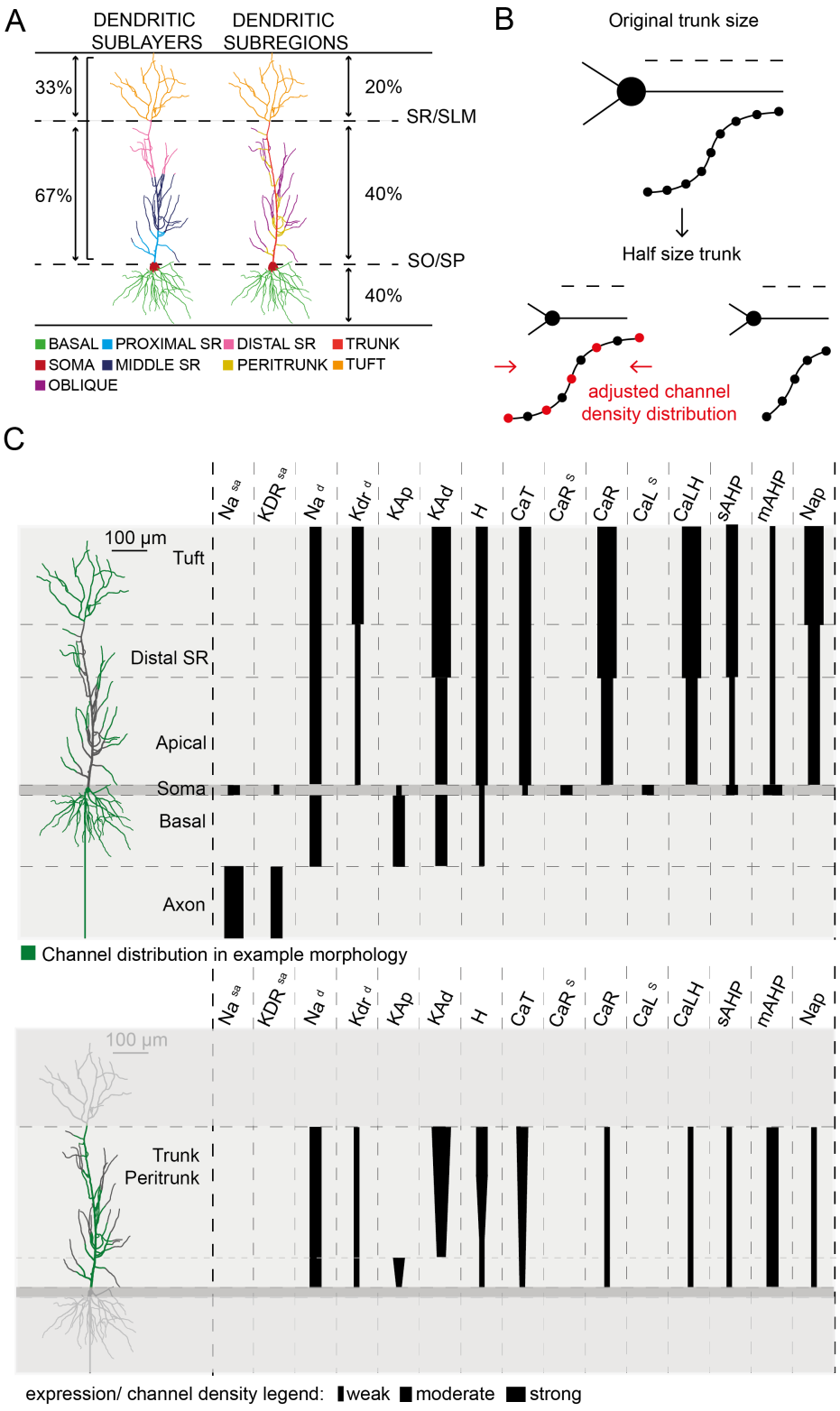

Figure 10. Ion channel distribution according to the model by Poirazi *et al.* (2003b)

Reproduced Figure 2 from "Modelling the contributions to hyperexcitability in a mouse model of Alzheimer's disease" (doi: https://doi.org/10.1113/JP283401) by Mittag M, Mediavilla L, Remy S, Cuntz H, Jedlicka P and licensed under CC BY 4.0 (Copyright Mittag *et al.*, 2023, http://creativecommons.org/licenses/by/4.0/): **(See next page)**

Figure 10. (continued) A, Division of the dendritic tree into layers and subregions. The boundaries between different parts correspond to changes in the electrotonic properties and ion channel densities. **B**, Ion channels are non-linearly distributed depending on the distance to soma. For diverse CA1 PCs with different morphologies and sizes the channel distribution had to be rescaled accordingly. *Top*: Trunk of the original cell. *Bottom left*: cell with an apical trunk half the size of the original. Resampling of the original laminar depth. *Bottom right*: Adjustment of the laminar depth to fit the new trunk size. **C**, Ion channel distribution within the CA1 PC depending on dendritic region according to the biophysical model by Poirazi *et al.* (2003b). *Left*: exemplary morphology. *Right*: Distribution of ion channel density. The relative thickness of the lines indicates the channel density.

All NEURON channel models were used with no modification. The division of the dendritic tree into subregions needed for the models channel distribution followed the typical sublayer division of PCs as described above: basal dendrites, soma, proximal SR, middle SR, distal SR, tuft and axon. Furthermore, the model by Jarsky *et al.* (2005) consisted of a passive method to correct for the missing implementation of actual spines: the specific membrane capacitance was scaled with 2 and the specific membrane resistance for regions above the distal SR with 0.5.

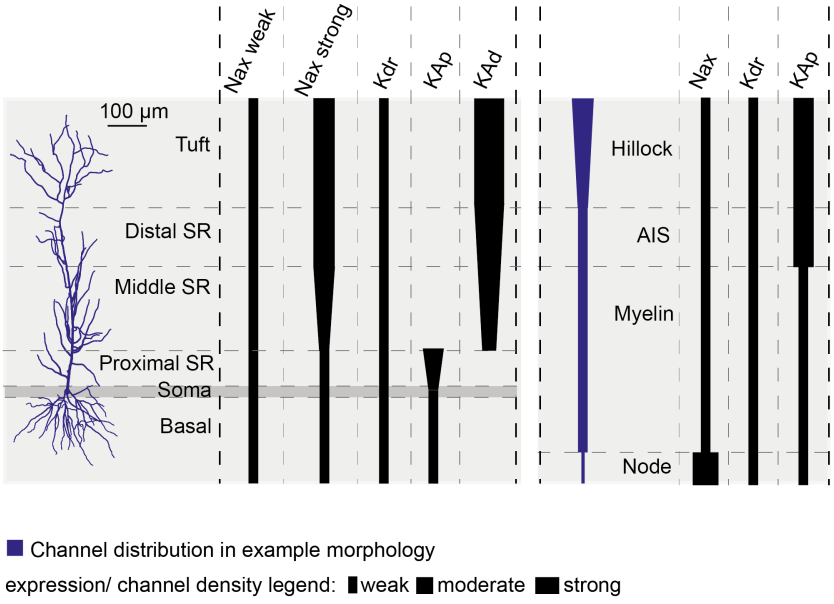

Figure 11. Ion channel distribution according to the model by Jarsky *et al.* (2005)

Reproduced Figure 3 A from "Modelling the contributions to hyperexcitability in a mouse model of Alzheimer's disease" (doi: https://doi.org/10.1113/JP283401) by Mittag M, Mediavilla L, Remy S, Cuntz H, Jedlicka P and licensed under CC BY 4.0 (Copyright Mittag *et al.*, 2023, http://creativecommons.org/licenses/by/4.0/): Ion channel distribution within the CA1 PC depending on dendritic region according to the biophysical model by Jarsky (Jarsky *et al.*, 2005). *Left*: exemplary morphology. *Right*: Distribution of ion channel density. The relative thickness of the lines indicates the channel density.

Both models (Jarsky *et al.*, 2005; Poirazi *et al.*, 2003a,b) have been tested and verified during their development via comparison to *in vitro* experiments. In this thesis however, a different computational tool is used (T2N, Beining *et al.*, 2017; Cuntz *et al.*, 2021; Mittag *et al.*, 2023). Therefore, it was important to test the behaviour of the implemented models to match the original ones and get equal results with no significant differences. In total, ten electrophysiological properties were calculated and analyzed between the cell models built in NEURON and T2N resulting in comparable values with small deviation (see **Table 2**). Furthermore, both models were implemented in an additional set of rat hippocampal CA1 PC morphologies (acquired 2018 *NeuroMorpho.org* database) and compared to experiments (acquired at *NeuroElectro.org* database).

Table 2. Comparison of electrophysiological features between the original NEURON models (Poirazi *et al.*, 2003a,b; Jarsky *et al.*, 2005) and their T2N versions, and between NeuroMorpho models and NeuroElectro data. Adapted from "A general principle of dendritic constancy: A neuron's size- and shape-invariant excitability" (Reference: Cuntz *et al.*, 2021, doi: https://doi.org/10.1016/j.neuron.2021.08.028) by Cuntz H, Bird AD, Mittag M, Beining M, Schneider M, Mediavilla L, Hoffmann FZ, Deller T, Jedlicka P in *Neuron, 2021,* and licensed under an Elsevier user license (Copyright Elsevier Inc. 2021, https://www.elsevier.com/about/policies-and-standards/open-access-licenses/elsevier-user).

Spiking features	**Poirazi: Original model (rat)**	**Poirazi: T2N version**	**Poirazi: *Neuro-Morpho* model**	**Jarsky: Original model (rat)**	**Jarsky: T2N version**	**Jarsky: *Neuro-Morpho* model**	***Neuro-Electro* data (rat)**
Input Resistance ($M\Omega$)	65.25	64.16	53.92 $\pm$14.21	67.72	68.46	70.37 $\pm$40.64	107.00 $\pm$77.58
Total Capacitance (pF)	115.60	110.88	232.20 $\pm$61.11	81.84	80.93	143.10 $\pm$43.71	89.80 $\pm$53.65
Time Constant (ms)	11.02	12.68	9.70 $\pm$ 1.12	7.74	7.59	9.34 $\pm$ 1.67	24.50 $\pm$21.49
Resting Potential (mV)	$-$68.40	$-$68.40	$-$69.13 $\pm$ 0.28	$-$71.95	$-$72.25	$-$73.21 $\pm$ 0.37	$-$65.23 $\pm$ 4.89
Spike Threshold (mV)	$-$58.60	$-$58.51	$-$42.84 $\pm$ 0.53	$-$62.92	$-$62.30	$-$50.75 $\pm$ 1.64	$-$47.60 $\pm$ 7.73
Spike Amplitude (mV)	80.00	77.88	35.74 $\pm$ 1.61	97.93	97.51	83.65 $\pm$ 2.00	86.36 $\pm$12.26
Spike Peak (mV)	21.11	19.33	$-$7.01 $\pm$ 1.61	34.93	35.05	32.90 $\pm$ 2.83	31.74 $\pm$13.29
Spike Width (ms)	1.77	1.75	1.10 $\pm$ 0.06	0.82	0.82	0.81 $\pm$ 0.06	1.32 $\pm$ 0.61
AHP [1] Amplitude (mV)	1.67	1.30	2.01 $\pm$ 1.36	5.80	7.28	16.03 $\pm$ 4.02	6.96 $\pm$ 5.22
Rheobase (pA)	120	130	460 $\pm$ 110	130	150	440 $\pm$ 140	189 $\pm$ 287

[1] Afterhyperpolarisation

Subsequently, the two validated biophysical models by Jarsky *et al.* (2005) and Poirazi *et al.* (2003b) were implemented in reconstructed morphologies from WT and APP/PS1 mice (see **Table 3** for their electrophysiological features and Šišková *et al.*, 2014) and used in all simulations in chapter two of this thesis (Mittag *et al.*, 2023).

Table 3. Major electrophysiological features of the two biophysical models (Poirazi *et al.*, 2003a,b; Jarsky *et al.*, 2005) implemented in reconstructed WT and APP/PS1 PC morphologies (mice) using T2N. Reproduced from "Modelling the contributions to hyperexcitability in a mouse model of Alzheimer's disease" (doi: https://doi.org/10.1113/JP283401) by Mittag M, Mediavilla L, Remy S, Cuntz H, Jedlicka P and licensed under CC BY 4.0 (Copyright Mittag *et al.*, 2023, http://creativecommons.org/licenses/by/4.0/).

Spiking features	**Poirazi: WT model cells**	**Poirazi: APP/PS1 model cells**	**Jarsky: WT model cells**	**Jarsky: APP/PS1 model cells**
Input resistance ($M\Omega$)	117.04 ± 22.11	133.70 ± 33.15	212.05 ± 60.74	262.68 ± 94.45
Total Capacitance (pF)	96.92 ± 31.55	75.85 ± 20.42	54.22 ± 18.88	41.68 ± 12.37
Time Constant (ms)	9.29 ± 1.10	8.34 ± 0.90	12.51 ± 1.30	12.90 ± 1.92
Resting Potential (mV)	-68.39 ± 0.20	-68.40 ± 0.34	-71.38 ± 0.29	-71.38 ± 0.47
Spike Threshold (mV)	-60.07 ± 0.34	-59.99 ± 0.16	-53.80 ± 5.30	-55.57 ± 5.98
Spike Amplitude (mV)	81.04 ± 3.02	82.25 ± 3.26	89.56 ± 5.75	91.37 ± 6.11
Spike Peak (mV)	20.97 ± 3.05	22.25 ± 3.30	35.75 ± 1.66	35.80 ± 1.17
Spike Width (at $-30mV$, in ms)	1.46 ± 0.11	1.43 ± 0.06	0.79 ± 0.05	0.79 ± 0.04
AHP [1] Amplitude (mV)	1.40 ± 0.20	1.31 ± 0.26	17.05 ± 5.83	14.91 ± 6.90
Rheobase (pA)	33 ± 14	28 ± 12	119 ± 38	95 ± 35

4.2.2 Cortical cell model by Korngreen et al.

Additionally to the two hippocampal models by Jarsky *et al.* (2005) and Poirazi *et al.* (2003b), a third active model for PCs was implemented. The model by Almog and Korngreen (2014) was ported to *T2N* in a similar manner as the models above. A specific feature of this model is to produce dendritic and NMDA spikes in cortical rat L5 PCs which has been shown in previous experiments. As described in Cuntz *et al.* (2021), the model includes eight voltage- and calcium-gated ion channels: a slow inactivating K^+ channel, a fast inactivating K^+ channel,

a hyperpolarisation-activated Ih channel, a Na^+ channel, a high voltage-activated (HVA) Ca^{2+} channel, a medium voltage-activated (MVA) Ca^{2+} channel, a small-conductance Ca^{2+}-gated K^+ (SK) channel and a large-conductance Ca^{2+}-gated K^+ channel (BK). The conductance distribution in the dendrites decreases exponentially with somatic distance for the potassium channels and the h channel. The remaining channels show a linear decrease with somatic distance. Again, the channels were adapted in a similar manner as with the models above in order to ensure the same distance relation and maximum values in all cells with different morphologies and sizes. Note, though, that in contrast to the hippocampal models the distance dependent conductances here in the cortical model decay with increasing distance to soma, partially in an exponential and not linear way. The passive and active model parameters fall within the values of Almog and Korngreen (2014) and lead to similar behaviour (compare electrophysiological features and model validation in **Table 4**). Though the capacitance is higher and input resistance lower, respectively, in the original cell, since it was much bigger than the average of the data set used here.

Table 4. Spiking features of the model by Almog and Korngreen (2014). Reproduced from "A general principle of dendritic constancy: A neuron's size- and shape-invariant excitability" (Reference: Cuntz *et al.*, 2021, doi: https://doi.org/10.1016/j.neuron.2021.08.028) by Cuntz H, Bird AD, Mittag M, Beining M, Schneider M, Mediavilla L, Hoffmann FZ, Deller T, Jedlicka P in *Neuron, 2021,* and licensed under an Elsevier user license (Copyright Elsevier Inc. 2021, https://www.elsevier.com/about/policies-and-standards/open-access-licenses/elsevier-user).

Spiking features	**Original model**	***T2N* version**	**L5 morphologies**
Input resistance ($M\Omega$)	6.56	6.16	21.35 ± 9.3
Total Capacitance (pF)	111.72	112.61	53.10 ± 22.42
Time Constant (ms)	1.3	1.43	1.31 ± 0.26
Resting Potential (mV)	-71.3	-71.03	-69.84 ± 6.5
Spike Threshold (mV)	-67.5	-66.6	-64.9 ± 0.84
Spike Amplitude (mV)	75.6	75	85.7 ± 4.5
Spike Peak (mV)	8.1	8.35	20.8 ± 5.1
Spike Width (at $-30mV$, in ms)	0.68	0.64	2.03 ± 0.74
AHP [1] Amplitude (mV)	1.65	2.1	3.6 ± 0.84
Rheobase (pA)	500	500	270 ± 90

4.2.3 GC model by Beining et al.

For the GCs the compartmental model from Beining *et al.* (2017) was used. It consists of 16 voltage-gated ion channels including region- and voltage-dependent Na^+, K^+ and Ca^{2+}

channels as well as calcium-dependent K^+ channels (SK, BK). Ion channel distribution and layer dependence is shown in **Figure 12**. This GC model was further employed to create a population of models to study the impact of the model itself on the GC function. In total, 20000 GC models were generated by variation of 27 parameters, especially the channel conductances, in a range of $[0, 2]$ times the original value, as shown in Schneider *et al.* (2023). Approximately 7% of the model population could be considered "good" regarding a $Fitness$ function ($F < 2$) that calculated the closeness of the electrophysiological behaviour to experiments (Schneider *et al.*, 2023). Additionally, reduced and valid models of just 9 channels were generated and compared. From 20000 reduced GC models only 3% had a $Fitness$ function of $F < 2$. The robustness, i.e. the ability of the model to still generate realistic behaviour under perturbations, of each model set and performance was investigated. Thereby, channel noise of $\pm 5\%$, $\pm 15\%$ to $\pm 25\%$ and $\pm 45\%$ to $\pm 55\%$ was added respectively. In order to simulate abGCs, the same reconstructed morphologies as for the mGCs were applied but with decreased synaptic density (40%, see schematic in **Figure 28** top) and (partially) blocked channels (Kir, Kv, BK channels) according to literature (Mongiat *et al.*, 2009; Beining *et al.*, 2017). **Table 5** shows electrophysiological features comparing the mGC and abGC models.

4.2.4 Leaky-integrate-fire model

As a fast toy model without actual ion channels but with the dendritic morphology included, a leaky-integrate-fire (LIF) model was implemented by using the *LIF_tree* function from the *TREES* toolbox (Cuntz *et al.*, 2007). The LIF model induced distributed synaptic conductances into the morphologies and calculated the resulting local voltage change. Synaptic conductances followed a double exponential ($\tau_1 = 0.4ms$, $\tau_2 = 2.5ms$). G_{syn} was scaled with G_{scale} according to **Equation 10**. Time constant τ_2 and membrane conductance G_m were varied with $scale = [0.2, 0.5, 1, 2, 3]$ to generate a population of LIF models. When the voltage at the root exceeded the threshold of $V_{th} = 10mV$ an AP was generated; afterwards the voltage was set again to $V_r = 0mV$.

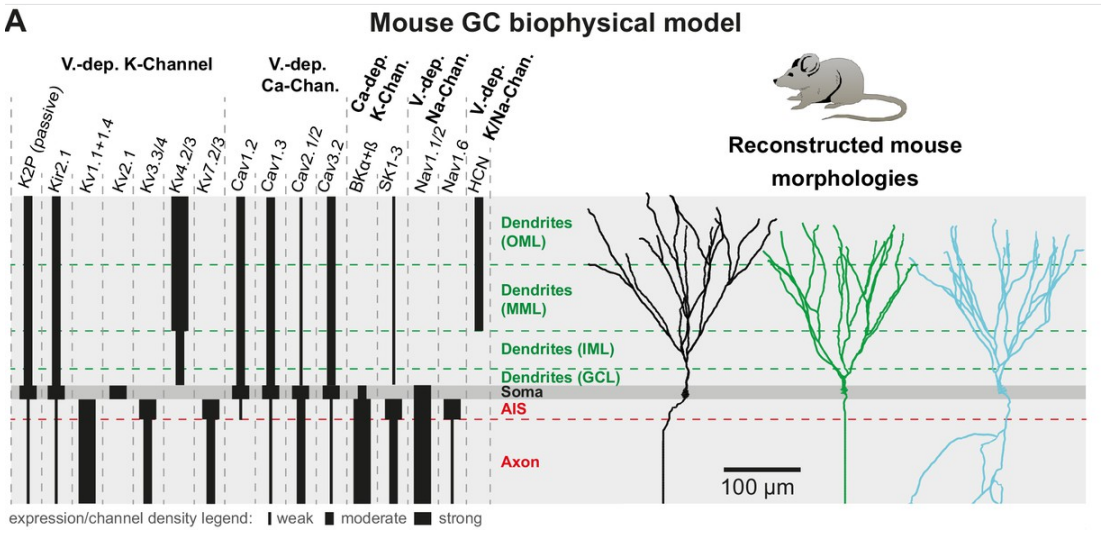

Figure 12. Ion channel distribution according to the model by Beining *et al.* (2017)

Reproduced Figure 2 A from "T2N as a new tool for robust electrophysiological modeling demonstrated for mature and adult-born dentate granule cells" (doi: https://doi.org/10.7554/elife.26517) by Beining M, Mongiat LA, Schwarzacher SW, Cuntz H, Jedlicka P and licensed under CC BY 4.0 (Copyright Beining *et al.*, 2017, http://creativecommons.org/licenses/by/4.0/): **A**, *Left*: Ion channel distribution within the GC from the mouse DG depending on cell region (OML, outer molecular layer; MML, middle molecular layer; IML, inner molecular layer; soma; axon; AIS, axon initial segment). The relative thickness of the lines indicates the channel density. *Right*: Three exemplary reconstructed mouse GC morphologies from Schmidt-Hieber *et al.* (2007).

Table 5. Spiking features of several GC model cells with Beining *et al.* (2017) implementation

Spiking features	**Schmidt-Hieber GCs**	**Vucsic et al. WT GCs**	**adult born GCs**
Input resistance ($M\Omega$)	207.92 ± 17.93	214.83 ± 10.93	208.59 ± 17.55
Total Capacitance (pF)	50.79 ± 7.99	45.81 ± 4.70	50.88 ± 8.03
Time Constant (ms)	25.03 ± 0.77	25.54 ± 0.49	25.25 ± 0.89
Resting Potential (mV)	-89.79 ± 0.04	-89.82 ± 0.04	-87.43 ± 0.04
Spike Threshold (mV)	-44.61 ± 1.10	-44.04 ± 0.30	-44.61 ± 1.20
Spike Amplitude (mV)	76.55 ± 9.30	86.37 ± 7.95	76.68 ± 9.02
Spike Peak (mV)	31.94 ± 9.72	42.33 ± 7.91	32.07 ± 9.50
Spike Width (at $-30mV$, in ms)	1.54 ± 0.42	1.16 ± 0.24	1.52 ± 0.41
AHP [1] Amplitude (mV)	5.87 ± 0.17	5.65 ± 0.12	5.19 ± 0.16
Rheobase (pA)	55.75 ± 9.38	49.27 ± 5.12	46.50 ± 7.62

4.3 Excitatory and inhibitory synapses and their activation

In both active compartmental CA1 PC models by Jarsky *et al.* (2005) and Poirazi *et al.* (2003b), the cortical L5 PC model by Almog and Korngreen (2014) and the DG GC model by Beining *et al.* (2017) excitatory, glutamate Alpha-amino-3-hydroxy-5-Methyl-4-isoxazole-Propionic Acid (AMPA) synapses were implemented along the dendrites. They constitute the main signal transfer of the neurons. The synapses were realised as time-dependent conductances following a dual-exponential with rise time constant of $\tau_1 = 0.2ms$ and decay time constant of $\tau_2 = 2.5ms$ (Cuntz *et al.*, 2021; Mittag *et al.*, 2023). Thereby, the reversal potential sat at $0mV$ (`Exp2Syn` NEURON object). In chapter one of this thesis, for all simulations with homogeneous synapse distribution, the synaptic weights had a strength between $0.2nS$ (low conductance) and $0.8nS$ (high conductance state) and the synapse density was $1 \cdot synapse/\mu m$. In chapter two, the synaptic weights were reduced to $0.1nS$ and the density to $0.5 \cdot synapse/\mu m$.

With increased model complexity more biological details were incorporated. Consequently, N-Methyl-D-Aspartate (NMDA, another glutamate receptor) synapses were included with a voltage-dependence that is non-linear. They consisted of a magnesium block which could be released with strong enough depolarisation. Compared to AMPA synapses the NMDA synapses had slower exponentials with rise time constant of $\tau_1 = 0.33ms$ and decay time constant of $\tau_2 = 50ms$ with the same reversal potential of $0mV$ (`Exp2nmda2` NEURON object based on Krueppel *et al.*, 2011). The NMDA synapses resided at the same location as the AMPA synapses and therefore had the same density distribution and were excited by the same presynaptic Poisson input. In chapter two, as a control experiment, the decay time constant τ_2 was increased as a possible consequence of amyloid-β accumulation.

As a third group of synapses, inhibitory GABA-A (Gamma-Aminobutyric Acid) synapses were added. They were modeled with the `Exp2Syn` function (similar to AMPA synapses) but with a negative equilibrium potential. In chapter one, their reversal potential varied between $-80mV$ and $-65mV$ as a control experiment (Cuntz *et al.*, 2021). In chapter two, it was constant at $-70mV$. The weights of the GABA-A synapses in chapter one had, as a simplification, the same strength as the AMPA synapses. In chapter two, a more realistic strength of $2nS$ was implemented (Bloss *et al.*, 2016; Mittag *et al.*, 2023). In chapter three no inhibition was added.

For chapter one, with respect to the theoretical calculations (see Introduction), it was necessary to employ a homogeneous synapse distribution. For chapter two and three, more realistic, inhomogeneous synaptic distributions for the densities of the AMPA, NMDA and GABA-A synapses were implemented. Each subregion of the dendritic tree displayed a different synaptic density with respect to experimental data from Megías *et al.* (2001); Šišková *et al.* (2014); Bloss *et al.* (2016) for the hippocampal PCs and proportional to Schmidt-Hieber *et al.* (2007) for the dentate GCs. For pathological AD cells in APP/PS1 morphologies the AMPA density in the tuft region was reduced to 82.3% of WT synapse density as seen in experiments by Šišková *et al.* (2014). Furthermore, the synaptic weights were inhomogeneously distributed as well. The apical synaptic weights in CA1 PCs generally increase for AMPA synapses and simultaneously decrease for NMDA synapses with increased path length to soma (Magee and Cook, 2000; Katz *et al.*, 2009; Kim *et al.*, 2015; Mittag *et al.*, 2023). Therefore, in chapter one, the AMPA synapses were scaled linearly with a factor between 0.8 and 1.2 of the original value along the apical center line with the maximum value at the longest distance from soma (Cuntz *et al.*, 2021). In chapter two, the AMPA synapses increased with the relation $g_{AMPA} = (0.4 + p) \cdot scale_{AMPA}$ for the conductance values with $scale_{AMPA} = 0.1nS$ and p the path-length from soma to synapse location x divided by the maximum path-length of the PC $p = path(x)/max(path(cell))$. Additionally, the NMDA synapses decreased with the relation $g_{NMDA} = (1.2 - 0.4 \cdot p) \cdot scale_{NMDA}$ with $scale_{NMDA} = 0.1nS$ (Mittag *et al.*, 2023). The respective slopes of the weight distributions were calculated beforehand by injecting depolarising inputs to the PC trunks. Subsequently the weights were changed with respect to soma distance to ensure similar somatic answers and EPSPs. This is in accordance with experiments and the principle of dendritic democracy (Magee and Cook, 2000; Häusser, 2001). In contrast, synaptic weights in the tuft area of CA1 PCs are constant (Bittner *et al.*, 2012) and take the maximum value of the AMPA and NMDA conductances as calculated above. Finally, in chapter two and three, lognormal (hippocampal PCs: $\mu = -1.5, \sigma = 0.9$, dentate GCs: $\mu = -2.2, \sigma = 0.5$) distributions were added to the excitatory conductances (weighted with $scale_{AMPA}/2$ and $scale_{NMDA}/2$ respectively) to increase their variability and convert the weights into a more realistic distribution with mostly weak and just a few strong synapses (Mittag *et al.*, 2023, PCs: Ballesteros-Yáñez *et al.*, 2006; Arellano *et al.*, 2007; Katz *et al.*, 2009; Benavides-Piccione *et al.*, 2013; Bromer *et al.*, 2018, GCs: Jungenitz *et al.*, 2018).

Table 6. Hippocampal CA1 PC model synapse densities based on data from Megías *et al.* (2001), Bloss *et al.* (2016) and Šišková *et al.* (2014). Reproduced from "Modelling the contributions to hyperexcitability in a mouse model of Alzheimer's disease" (doi: https://doi.org/10.1113/JP283401) by Mittag M, Mediavilla L, Remy S, Cuntz H, Jedlicka P and licensed under CC BY 4.0 (Copyright Mittag *et al.*, 2023, http://creativecommons.org/licenses/by/4.0/).

Dendritic region	**AMPA,NMDA** $synapse/\mu m$	**GABA** $synapse/\mu m$
Proximal basal	0.1	0.3
Middle basal	0.3	0.2
Distal basal	2.0	0.06
Proximal apical trunk	0.3	0.3
Distal apical trunk	3.5	0.06
Proximal apical oblique	2.2	0.05
Distal apical oblique	2.7	0.05
Proximal tuft	1.2	0.2
Distal tuft	0.8	0.2

Table 7. Dentate Gyrus GC synapse densities.

Dendritic region	GCL	IML	MML	OML
AMPA,NMDA $synapse/\mu m$	0.05	0.1	0.2	0.05

Activation of the synapses was implemented via `VecStim` point processes. These can be seen as artificial point neurons that induce input spike trains to the synapses (T2N function `t2n_poissonSpikeGen`: APs from a presynaptic spike generator with Poisson distribution). For each chapter of this thesis, different input frequencies for the Poisson spike trains were implemented. In all simulations however, the cells were subject to ongoing background activity generated randomly (Poisson distribution) with an average spiking frequency that ranged from $0.1Hz$ to $15Hz$. In chapter one, clustered stimulations of only a subgroup of synapses in the basal or apical dendrites of PCs was added to test the limits of the dendritic constancy hypothesis (Cuntz *et al.*, 2021). In chapter two, the addition of strong perisomatic inhibition in the high γ range of $50-100Hz$ (Craig and McBain, 2015; Strüber *et al.*, 2017; Mittag *et al.*, 2023) created spontaneous burst firing patterns (inter-spike-interval $ISI \leq 13.3ms$), a typical firing mode in AD cells (Šišková *et al.*, 2014). More importantly, neuronal firing of the cells was induced by the major input pathways from the surrounding network. In addition to background activation, correlated theta input of $5Hz$ was included to the excitatory synapses in tuft (perforant pathway), basal (Schaffer collateral basal pathway) and apical (Schaffer collateral apical pathway) dendritic regions of the CA1 PCs in chapter two (Bannister and Larkman, 1995; Megías *et al.*, 2001; Ang *et al.*, 2005; Manns *et al.*, 2007; Takahashi and Magee, 2009; López-Madrona *et al.*, 2021). In chapter three, perforant pathway input (from

EC) to the GCs was implemented. In order to have a specific correlation of the input spike trains for each pathway, a spike generator was created that copied a random spike train with a probability equal to the target correlation for the input spike train of another synapse (`t2n_poissonSpikeGen2`). In chapter three, the selection of the input spike trains was even more careful. In order to create an ensemble of spike trains with specific train number, Poisson frequency, phase and correlation the *pattern separation toolbox* was used (Bird *et al.*, 2024). This was necessary to compare input ($5 - 8$ random key input synapses in the outer molecular layer) and output (evaluated at soma) spike trains for the pattern separation measure as described below. The detailed activation frequencies of the experiments are mentioned in the corresponding section and figure.

4.4 AD-related extrinsic (network) and intrinsic (ion channel) modifications

As described in detail in the paper by Mittag *et al.* (2023), a total of eleven possible configurations of parameter changes and their effects on simulated synaptic activation of APP/PS1 CA1 PCs were explored (see **Table 8**). These configurations included observed extrinsic alterations of excitatory, inhibitory and network inputs as well as intrinsic alterations of ion channel densities, and all their possible combinations, as listed below:

1. *Excitation*: increased frequency + correlation of Poisson input to AMPA/NMDA synapses
2. *Burst input*: increased presynaptic burst frequency and pattern
3. *Inhibition*: decreased GABAergic synaptic input
4. *Channels*: scaling of the channel densities I_{AHP}, I_{Nap}, I_{Na} and I_{CaT}
5. *E/I imbalance (enhanced excitation, reduced inhibition)*,
6. *Burst input plus inhibition*,
7. *Channels plus excitation*,
8. *Channels plus inhibition*,
9. *Channels plus E/I*,
10. *Burst input plus channels*,
11. *Burst input plus inhibition and channels*.

A 4-step system of incremental alterations of parameters from P1 to P4 was implemented

with increasing distance to the control value for each of the configurations. Starting with the parameter setup for the WT cell group, the respective parameters in the APP/PS1 cell group were progressively modified to eventually achieve a similar spike rate and pattern as in the data from Šišková *et al.* (2014). Further variation of the parameters was continued until the firing rate and burst rate diverged again from the data.

Configuration *Excitation*: the Poisson frequency of the excitatory input to the AMPA/NMDA synapses was enhanced from the control "$P0$" value of $1Hz$ to $P1$ of $1.1Hz$, up to $P4$ of $1.8Hz$; meanwhile the input correlation ranged from $P1$ of 0.7 to $P4$ of 1.

Configuration *Inhibition*: the GABA synapse density was reduced step-wise from $P1$ of 75% to $P4$ of 35%.

Configuration *Burst input*: spike trains of elevated burst activity were fed to 4% of excitatory synapses. In line with the range of firing rates and burst patterns from *in vivo* patch-clamp recordings in healthy cells (Šišková *et al.*, 2014), the WT and control ("$P0$") APP/PS1 model cells received four singlets and one doublet per two seconds per synapse (input frequency $3Hz$, input burst frequency $0.5Hz$, ISI $10ms$). Whereas the modified APP/PS1 model cells received more and stronger bursts from $P1$ (input frequency $4Hz$, input burst frequency $1Hz$) to $P4$ (input frequency $8.5Hz$, input burst frequency $2.5Hz$). The input pattern can be seen in **Figure 21 C**. The coefficient of variation (cv) for the input frequency per cell in all cases was 0, since all stimulated synapses received the same number of input spikes.

The other configurations regarding combinations of changes included also combined alterations of the same parameters. In these cases, the individual parameters were varied less strongly but within the same range. A complete overview of all parameter configurations is given in **Table 8** and Mittag *et al.* (2023).

Table 8. All explored extrinsic and intrinsic parameter configurations. Reproduced from "Modelling the contributions to hyperexcitability in a mouse model of Alzheimer's disease" (doi: https://doi.org/10.1113/JP283401) by Mittag M, Mediavilla L, Remy S, Cuntz H, Jedlicka P and licensed under CC BY 4.0 (Copyright Mittag *et al.*, 2023, http://creativecommons.org/licenses/by/4.0/).

Configuration	Feature	Control	Variation P1	Variation P2	Variation P3	Variation P4
Excitation	input frequency	$1Hz$	$1.1Hz$	$1.3Hz$	$1.6Hz$	$1.8Hz$
	input correlation	0.4	0.7	0.8	0.9	1
Inhibition	% GABA activation	100	75	60	45	35
Scenario 1: E/I imbalance	input frequency	$1Hz$	$1.1Hz$	$1.3Hz$	$1.3Hz$	$1.3Hz$
	input correlation	0.4	0.7	0.8	0.9	1
	% GABA activation	100	50	75	60	50
Channels	scale I_{Na}	1	1.1	1.3	1.5	3
	scale I_{Nap}	1	2.5	2.5	2.5	3
	scale I_{CaT}	1	2.5	2.5	2.5	3
	scale I_{AHP}	1	0.8	0.5	0.3	0.1
Channels plus excitation	input frequency	$1Hz$	$1.1Hz$	$1.2Hz$	$1.3Hz$	$1.3Hz$
	input correlation	0.4	0.7	0.8	0.9	0.9
	scale I_{Na}	1	1.3	1.3	1.3	1.5
	scale I_{Nap}	1	2.5	2.5	2.5	2.5
	scale I_{CaT}	1	2.5	2.5	2.5	2.5
	scale I_{AHP}	1	0.5	0.5	0.5	0.3
Channels plus inhibition	% GABA activation	100	70	60	50	50
	scale I_{Na}	1	1.3	1.3	1.3	1.5
	scale I_{Nap}	1	2.5	2.5	2.5	2.5
	scale I_{CaT}	1	2.5	2.5	2.5	2.5
	scale I_{AHP}	1	0.5	0.5	0.5	0.3
Scenario 2: Channels plus E/I imbalance	input frequency	$1Hz$	$1.1Hz$	$1.1Hz$	$1.1Hz$	$1.3Hz$
	input correlation	0.4	0.7	0.7	0.8	0.9
	% GABA activation	100	60	70	60	75
	scale I_{Na}	1	1.3	1.5	1.5	1.3
	scale I_{Nap}	1	2.5	2.5	2.5	2.5
	scale I_{CaT}	1	2.5	2.5	2.5	2.5
	scale I_{AHP}	1	0.5	0.3	0.3	0.8
Scenario 3: Burst input	input frequency	$3Hz$	$4Hz$	$6Hz$	$7Hz$	$8.5Hz$
	input burst frequency	$0.5Hz$	$1Hz$	$2Hz$	$2.5Hz$	$2.5Hz$

Continuation of Table 8

Configuration	Feature	Control	Variation P1	Variation P2	Variation P3	Variation P4
Burst input plus inhibition	input frequency	$3Hz$	$6Hz$	$6Hz$	$7Hz$	$7Hz$
	input burst frequency	$0.5Hz$	$2Hz$	$2Hz$	$2.5Hz$	$2.5Hz$
	% GABA activation	100	80	50	80	50
Burst input plus channels	input frequency	$3Hz$	$4Hz$	$6Hz$	$7Hz$	$7.5Hz$
	input burst frequency	$0.5Hz$	$1Hz$	$2Hz$	$2.5Hz$	$2.5Hz$
	scale I_{Na}	1	1.3	1.3	1.3	1.3
	scale I_{Nap}	1	2.5	2.5	2.5	2.5
	scale I_{CaT}	1	2.5	2.5	2.5	2.5
	scale I_{AHP}	1	0.5	0.5	0.5	0.5
Burst input inhibition and channels	input frequency	$3Hz$	$4Hz$	$6Hz$	$6Hz$	$7Hz$
	input burst frequency	$0.5Hz$	$1Hz$	$2Hz$	$2Hz$	$2.5Hz$
	% GABA activation	100	80	80	50	50
	scale I_{Na}	1	1.3	1.3	1.3	1.3
	scale I_{Nap}	1	2.5	2.5	2.5	2.5
	scale I_{CaT}	1	2.5	2.5	2.5	2.5
	scale I_{AHP}	1	0.5	0.5	0.5	0.5

4.4.1 Configurations of hyperexcitability scenarios

After investigation of all possible parameter configurations of observed extrinsic and intrinsic alterations, three scenarios were identified showing increased firing rates and the change in the firing mode from singlets to bursts (Mittag *et al.*, 2023) as measured in Šišková *et al.* (2014).

Scenario 1 (*E/I imbalance*): a close match to the data was achieved by the parameter variation $P3$ via increased Poisson input frequency (from $1Hz$ to $1.3Hz$) and stronger spike train correlations (increased from 0.4 to 0.9) combined with diminished inhibitory inputs (40% decrease of dendritic and somatic inhibition). The cv of the input per cell was 0.41 (in WT), 0.41 (in APP/PS1) and 0.16 ($P3$ of APP/PS1) respectively. This was due to higher mean input frequency and smaller variation. A further increase of input frequency or impairment of inhibition in $P4$ of Scenario 1 worsened the reproduction with data (Mittag *et al.*, 2023).

Scenario 2 (*Channels plus E/I*): a close match to the data was achieved by the parameter variation $P4$ (Mittag *et al.*, 2023), which was comparable to Scenario 1 but with a milder reduction of inhibition (25% decrease in GABA density) and additional scaling of ion channel densities (1.3 for I_{Na}, 0.8 for I_{AHP} and 2.5 for I_{Nap} and I_{CaT}). The cv per cell input was 0.41 (WT), 0.41 (APP/PS1) and 0.17 ($P4$ of APP/PS1).

Scenario 3 (*Burst input*): a presynaptic network with burst input to 4% of the AMPA/NMDA synapses was implemented using four singlets and one doublet per two seconds in the control condition $P0$. Subsequently, enhanced network burst input was modelled using an increasing number of bursts in the parameter variations $P1$ to $P4$. A close match with the data was seen for $P3$ with synaptic input of one singlet, two doublets and three triplets per two seconds (Mittag *et al.*, 2023). Importantly, a different input spike train of one less burst or one more singlet ($P2$ and $P4$) showed a higher error and no change in the firing mode from singlets to bursts as shown in **Figures 20** and **21**.

4.4.2 Ion channel configurations

Ion channel alterations were modelled by modifying their respective conductances according to observed experiments in AD research and the *in silico* investigations (Mittag *et al.*, 2023) in this thesis. Ion channel expression was reduced or its density increased with a scaling factor to the maximum channel conductance. For example, the voltage-dependent sodium channel I_{Na} in the axon (Liu *et al.*, 2015; Wang *et al.*, 2016; Ghatak *et al.*, 2019) was scaled up in the range $[1, 2]$ and the persistent sodium channel I_{Nap} in the soma (Williams and Stuart, 1999; Yue *et al.*, 2005; Beck and Yaari, 2008) was scaled up in the range $[1, 3]$. At the same time the medium AHP calcium-activated potassium channel I_{AHP} in the soma and apical dendrites was scaled down in the range $[0.3, 1]$ in line with experimental values (Beck and Yaari, 2008; Zhang *et al.*, 2014; Wang *et al.*, 2015b,a; Niday and Bean, 2021). Meanwhile the T-type calcium channel I_{CaT} in dendrites (Yaari *et al.*, 2007; Beck and Yaari, 2008; Cain and Snutch, 2013; Medlock *et al.*, 2018; Garg *et al.*, 2021) was scaled up in the range $[1, 3]$. Altogether these changes yielded a four-dimensional parameter space of the corresponding four channels. Subsequently, the parameter space was scanned and the firing behaviour of the altered AD cells compared to the Šišková *et al.* (2014) data by implementing a cost/error function that measured the distance to the data. The dependence of each channel scaling on the other channels was illustrated

in **Figure 20**. A distinct minimum of the error for the chosen parameter range was found at a scaling of 1.3 for I_{Na}, 0.5 for I_{AHP} and 2.5 for I_{Nap} and I_{CaT}. A targeted sensitivity check was performed by looking at the vicinity of the ion channel scaling that increased bursting and lowered the error, in particular $[1.1, 1.2, 1.3, 1.4, 1.5]$ for I_{Na} and $[0.35, 0.45, 0.5, 0.55, 0.65]$ for I_{AHP}. Values beyond 3 for I_{Nap} and I_{CaT} were not considered as they seemed biologically unrealistic and not supported by the literature, though it is entirely possible that such scaling could induce hyperexcitability as well. The focus was rather on the possibility of channel changes influencing and enhancing burst firing at all, which was ultimately observed in the chosen range in line with the literature (and see Mittag *et al.*, 2023).

Configuration *Channels*: the result of the ion channel conductance scan was applied to the simulations containing ion channel changes. The variation of parameters ranged from $P1$ (scaling $I_{Na} = 1.1$, $I_{AHP} = 0.8$, $I_{CaT} = I_{Nap} = 2.5$) to $P4$ (scaling $I_{Na} = 3$, $I_{AHP} = 0.1$, $I_{CaT} = I_{Nap} = 3$). A complete list of all configurations of channel parameters is given in **Table 8** and Mittag *et al.*, 2023.

4.4.3 Cost functions

In order to compare the results of the simulations with the experimental results of Šišková *et al.* (2014), an error function (*Error*) was introduced which measured the distance between simulation (*Sim*) and experiment (*Exp*) via a root mean squared error normalised by the root of the squared standard error of the mean (*SEM*) (Borst and Haag, 1996; Mittag *et al.*, 2023):

$$Error_{Sim} = \sum^{Firingmode} (\mu_{Firing,Sim} - \mu_{Firing,Exp})^2 \tag{26}$$

$$Error_{Exp} = \sum^{Firingmode} (SEM_{Firing,Exp})^2 \tag{27}$$

$$Error = (Error_{Sim}/Error_{Exp})^{1/2} \tag{28}$$

This sum over firing modes included singlets ($1AP$), bursts ($> 1AP$) and triplets ($3AP$). The experimental values were taken from **Table 2** (Šišková *et al.*, 2014). Additionally, the error included the change in the firing mode from singlets to bursts with a preference of enhanced bursting (Mittag *et al.*, 2023, see an application in **Figure 20 D**, *right*):

$$\mu_{Singlet} > \mu_{Bursts} \rightarrow mode = 1 \tag{29}$$

$$\mu_{Singlet} < \mu_{Bursts} \rightarrow mode = -1 \tag{30}$$

This was considered in the evaluation and interpretation of simulations since data show a distinct mode transition from singlets to bursts (Šišková *et al.*, 2014). Therefore, models with a clear qualitative transition to bursts represent a better match to the data than models with a small quantitative error in firing rates, but a preferred firing mode of mainly singlets. Both costs were analysed together.

4.5 ATP consumption

In order to calculate the energy of the cell activity an ion counting system was used in chapter three. The Na^+ ions needed for the postsynaptic currents and APs are the main contributors to the energy budget (Attwell and Laughlin, 2001). For example, after a concentration change due to the flux of Na^+ and K^+ for an AP generation, the ion concentrations have to be restored again by ion pumps. In general, the Na^+/K^+ pump extrudes three Na^+ and imports two K^+ ions per one adenosine triphosphate (ATP) molecule (Post and Jolly, 1957). Therefore, for the calculation of the energy the ATP consumption can be used with the following relations, similar to Remme *et al.* (2018):

Na^+/K^+ pump with $1ATP$ consumption $\equiv 3$ Na^+ ions extrusion.
Na^+/Ca^{2+} exchange with 1 Ca^{2+} ion $\equiv 3$ Na^+ ions.
Charge Q of $1C$ of Na^+ with $6.24 \cdot 10^{18}$ particles.
Charge Q of $2C$ of Ca^{2+} with $6.24 \cdot 10^{18}$ particles.

All currents of the I_{Ca} channels were read out directly with the code. The sodium current however consisted of several contributions:

$$I_{Na} = I_{Na,channels} + I_{Na,syns} + I_{Na,leak} + I_{Na,h} \tag{31}$$

For the first term, the sodium channels were read out with the code. The other three terms were determined by the following calculations, e.g. synaptic transmission:

$$I_{syns} = I_{Na,syns} + I_{K,syns} + (I_{Ca,syns}) \tag{32}$$

The synaptic transmission included cations only. In AMPA synapses the Ca^{2+} ions could be neglected (see Harris *et al.*, 2015).

Similarly, the Leak current consisted of several contributions:

$$I_{leak} = I_{Na,leak} + I_{K,leak} + (I_{Ca,leak} + I_{Cl,leak}) \tag{33}$$

External Ca^{2+} was neglected as it only indirectly influences the leak sodium channel (see Lu *et al.*, 2010). Chloride was neglected as well since its influence occurs via GABA synapses which were not included in the set up. With Ohms law and the synaptic current the following expression was derived:

$$g_{syns} = g_{Na,syns} + g_{K,syns} \tag{34}$$

$$I_{syns} = g_{Na,syns}(V - V_{Na}) + g_{K,syns}(V - V_K) = g_{syns}(V - V_{syns}) \tag{35}$$

With the equilibrium potential for the synapses at $V_{syns} = 0$. Setting $V = 0$:

$$g_{Na,syns} = g_{syns}\frac{V_K}{(V_K - V_{Na})} \tag{36}$$

It follows for $I_{Na,syns}$:

$$I_{Na,syns} = g_{syns}\frac{V_K}{(V_K - V_{Na})}(V - V_{Na}) \tag{37}$$

With $g_{syns} = g_{AMPA}$.
Under the assumption of minimal Ca^{2+} entry through NMDA, the same expression for $I_{Na,NMDA}$ with $g_{syns} = g_{NMDA}$ follows.

The same derivation as for $I_{Na,syns}$ can be done for the sodium contributions of $I_{Na,leak}$ and $I_{Na,h}$ (leak and HCN channel):

$$I_{Na,leak} = g_{leak}\frac{(V_K - V_{rest})}{(V_K - V_{Na})}(V - V_{Na}) \tag{38}$$

$$I_{Na,h} = g_h \frac{(V_K - V_h)}{(V_K - V_{Na})}(V - V_{Na}) \tag{39}$$

With the equilibrium potentials at $V_{Na} = 87.76mV$, $V_K = -93mV$ and $V_h = -41.9mV$ respectively.

With the total sodium current I_{Na} and calcium current I_{Ca} per time step, consequently, the time dependent integral over the whole stimulation period T can be computed to get the charge:

$$\int_{t_0=0}^{T} I_{Na} dt = Q_{Na} \tag{40}$$

The same goes for Q_{Ca}.

With the relations above $ATP = ATP_{Na} + ATP_{Ca}$ can be calculated. One charge of sodium relates to $1/3 \cdot 6.24 \cdot 10^{18}$ ATP molecules and two charge of calcium relate to $6.24 \cdot 10^{18}$ ATP molecules, yielding:

$$ATP = (\frac{1}{3} Q_{Na} + \frac{1}{2} Q_{Ca}) \cdot 6.24 \cdot 10^{18} \tag{41}$$

4.6 Pareto optimality of economy and pattern separation

Known input frequencies of GCs in DG projecting from the EC were used (the perforant pathway with *theta* and *beta* signals between $5Hz$ and $20Hz$, Quintanilla *et al.*, 2022). In detail, two different frequencies with three different spike train patterns respectively were successively fed into five key input synapses of the GC outer molecular layer: phase-locked spike ensemble with three component trains, a spiking rate of $10Hz$ and $20Hz$, a correlation strength of 0.7 and a phase rate of $6Hz$. The different spike trains were generated with the *pattern separation toolbox* by Bird *et al.* (2024). The somatic output spikes were recorded at the same time. By comparing input and output spike patterns via the *pattern separation toolbox* by Bird *et al.* (2024) the relative redundancy reduction and sparsity weighted MI could be calculated as in **Equations 23** and **25** to get the pattern separation measure. During the simulation time of $2s$ the ATP (energy used for the extrusion of sodium and calcium as in **Equation 41**) with contributions from the channels and synapses (**Equation 37**) was recorded. For all valid GC models (Schneider *et al.*, 2023) the economy of energy and the pattern separation performance were calculated and compared. A model was decided to be on the Pareto front if it could not be outperformed by any other model in both, economy and pattern separation, at the same time. Additionally, the "efficiency" was defined and calculated: pattern separation divided by ATP use; as well as the "robustness": efficiency under noise divided by efficiency with no added noise. This is in similarity to commonly defined metabolic efficiency of MI/energy as for example in Stone (2018). Thereby, the added channel noise was homogeneously distributed between $\pm 5\%$ and $\pm 15\%$ to $\pm 25\%$ respectively; and an input noise (input loss due to deleted spikes) of 25% and 50% was integrated. The change in Pareto front was analysed under these conditions in chapter three in **Figure 27**. Furthermore, a systematic search for an improved Pareto front was set out. An optimisation algorithm was used to perturb the channel conductances (27 in total for all regions) one by one and in combination ($\pm 5\%$ each step) to find improved performances regarding economy and pattern separation, individually and simultaneously, for the experimentally validated GC model by Beining *et al.* (2017) in the $10Hz$ input condition. Resulting mechanisms were applied to the $20Hz$ condition as well. Importantly, the electrophysiological somatic *Fitness* of a model was not a constraint of the optimisation.

5 Results

5.1 Simulations and investigated questions

The main objective of this dissertation is to investigate the IO function of hippocampal nerve cells with a specific focus on their different morphological structures and intrinsic ion channels. How do these physiological differences and mechanisms affect the IO function? As a result, this dissertation uncovers an underlying principle for the cells' invariant activity. Furthermore, mechanisms for particular activity modification as well as optimisation are revealed. These are exemplified and investigated in two prominent cases: the pathological feature of AD hyperexcitability for CA1 PCs and the important memory function of pattern separation for DG GCs. In the following sections, the $T2N$ ported morphological and compartmental single cell models are applied. They are the main investigative *in silico* tools in this thesis, and their simulation results are presented here:
In chapter one (section 5.2), I investigate the hypothesis of invariant IO function for synaptic activation as a passive backbone and general activity-equalising principle of all cells, independent of their morphology or size. This is the dendritic constancy principle. Does the dendritic constancy claim still hold for realistic, active compartmental models including multiple computational non-linearities?
In chapter two (section 5.3), I investigate the dendritic constancy principle for pathological cells during AD progression. Here, I investigate the effect of dendritic retraction on the IO function in form of increased burst firing. If the dendritic remodeling does not cause the hyperexcitability then what other intrinsic (e.g. ion channels) or extrinsic (e.g. excitation and inhibition network) alterations during AD could be possible causes?
Finally, in chapter three (section 5.4), I focus on the GCs of the DG, an important area involved in memory formation. Here, I investigate the actual firing patterns of the cells with respect to the specific GC pattern separation IO function. How do various, valid cell models with different intrinsic ion channel expressions influence the GCs function of pattern separation and economy of energy simultaneously? Are there differences in IO function and underlying mechanisms for mGCs and newly formed abGCs?

5.2 Chapter 1: Dendritic constancy in active compartmental models

The main idea for the dendritic constancy hypothesis relates to the intuition that larger cells have a smaller input resistance and are therefore less excitable, but at the same time they also have more synaptic input and are therefore more excited. Ideally, both compensate each other for realistic synaptic activation. Indeed, the recent paper by Cuntz *et al.* (2021) showed analytically and numerically for a large data set from *NeuroMorpho.Org* (Ascoli *et al.*, 2007, 9841 reconstructions) that for passive dendrites under the condition of same average dendritic diameter for homogeneously distributed synaptic activation the voltage change at the soma is roughly the same. Consequently, the aim of this first chapter was to see if the results could be transferred to more realistic, active compartmental models that include voltage-dependent ion channels and other non-linearities. Hence, two well-known and validated CA1 PC models were implemented (Jarsky *et al.*, 2005 and Poirazi *et al.*, 2003b) to perform simulations of activated distributed synapses and to verify the results were model-independent. First, reconstructions of CA1 PCs from the *NeuroMorpho.Org* data set were investigated including mechanisms by Jarsky ($n = 105$, example morphology and simulation schematic in **Figure 13 A**, see also Cuntz *et al.*, 2021). The dendrites were stimulated with different input frequencies ($1Hz$ and $2Hz$) and synapse strengths (AMPA with $0.2nS, 0.4nS, 0.8nS$). For the results, the cell activity is shown versus dendritic path length, and the average value for the whole group is shown by a dashed line. In nearly all cases the firing rate was independent of the dendritic length and cell size (see **Figure 13 B** and **Table 9**). In addition to whole cell activation, more realistic clustered stimulation was investigated such as only distal apical dendrites (simulating the perforant pathway from EC), only basal dendrites (simulating the Schaffer Collateral pathway from CA3), 30% subtrees ($1Hz$) or hotspots (patches of 0.2% or 20 normalized synapses in the middle apical dendrite with $50Hz$) as shown in **Figure 13 C**. Again, the firing rate was independent of cell length in all examples. Second, the reconstructions of CA1 PCs were investigated with a different model by Poirazi *et al.* (2003a). For both, low and high conductance activation ($1Hz$ and $3.5Hz$), the somatic firing rate was independent of dendritic length. The model by Poirazi *et al.* (2003a) is known for producing dendritic spikes in addition to somatic events (see voltage traces in **Figure 13 D**). These dendritic events were largely independent of cell size as well. Even when there was a significant increase of the linear regression, the slope was quite small with only 3% rise per mm length (Cuntz *et al.*, 2021).

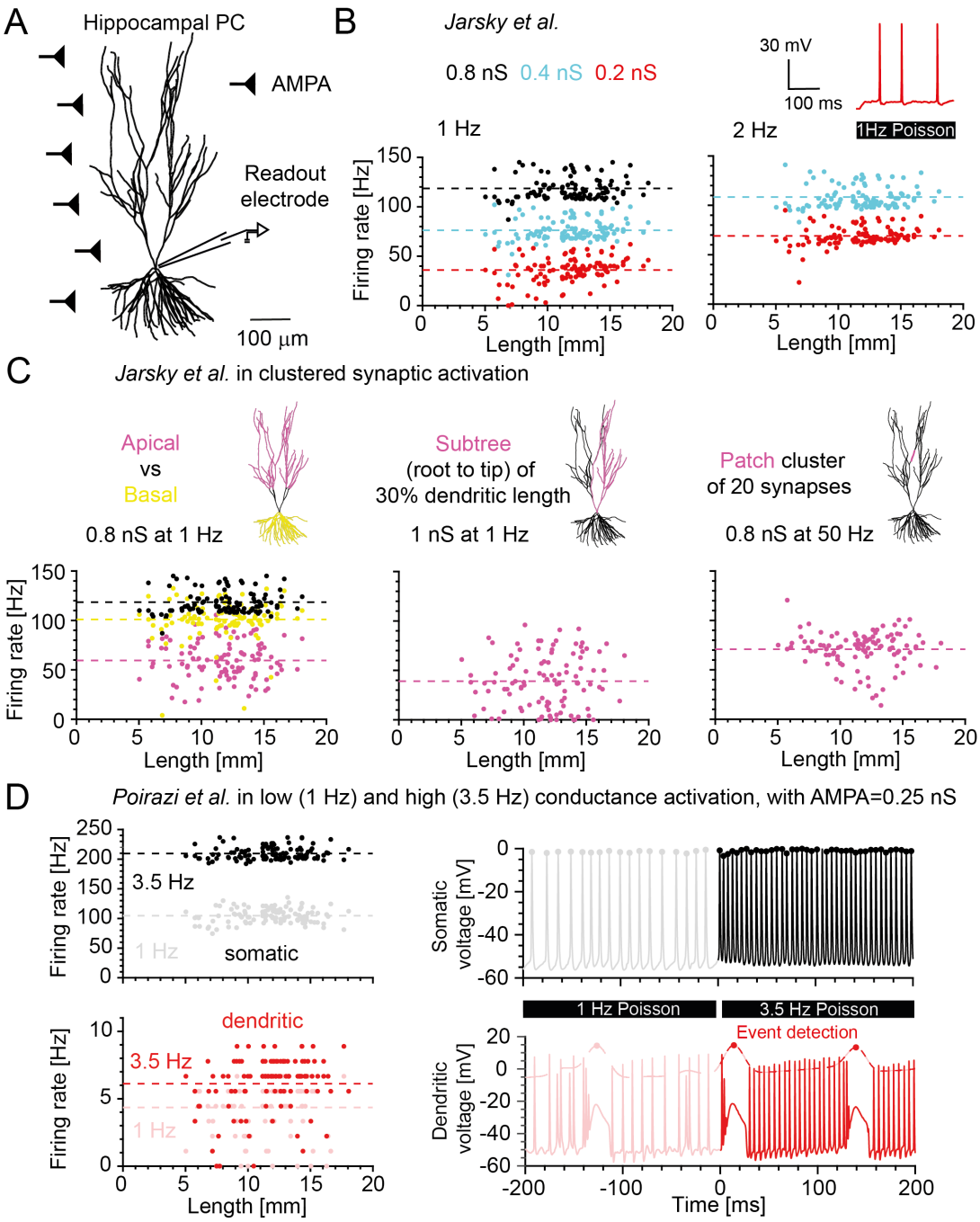

Figure 13. Distributed synaptic inputs in CA1 PCs with active biophysical compartmental models by Jarsky *et al.* (2005) and Poirazi *et al.* (2003b) lead to similar size-independent responses

A, Example morphology of hippocampal PC from *NeuroMorpho.Org* database (Ascoli *et al.*, 2007). **B**, Somatic firing rate responses to distributed AMPA inputs for three different synaptic strengths ($0.8nS$ *black*, $0.4nS$ *blue*, $0.2nS$ *red*) and two input frequencies ($1Hz$ *left*, $2Hz$ *right*) for PCs with channels by Jarsky *et al.* (2005). **C**, Synaptic activation of clusters. *Left*, apical vs. basal activation and their firing rate responses. *Middle*, activation of a subtree containing 30% of total dendritic length. *Right*, cluster of 20 synapses (normalized for total dendritic length) is activated. **D** *Top*, Somatic firing rate responses to low ($1Hz$, *black*) and high ($3.5Hz$, *grey*) activation of AMPA synapses for PCs with channels by Poirazi *et al.* (2003b). *Bottom*, same activation as above but for the dendritic responses.
(See next page)

Figure 13. (continued) Panels **B** *left*, **C** *left* and *right* adapted from "A general principle of dendritic constancy: A neuron's size- and shape-invariant excitability" (Reference: Cuntz *et al.*, 2021, doi: https://doi.org/10.1016/j.neuron.2021.08.028) by Cuntz H, Bird AD, Mittag M, Beining M, Schneider M, Mediavilla L, Hoffmann FZ, Deller T, Jedlicka P in *Neuron, 2021,* and licensed under an Elsevier user license (Copyright Elsevier Inc. 2021, https://www.elsevier.com/about/policies-and-standards/open-access-licenses/elsevier-user).

Further complexities and non-linearities were added to the morphology models in order to make them more realistic and test the robustness of the dendritic constancy principle. On top of AMPA synapses also NMDA synapses were put (consisting of double exponentials for rise and decay time, and a voltage dependent magnesium block). Additionally, 20% of the total number of synapses were turned into inhibitory GABA synapses. For different reversal potentials of the inhibition (see **Figure 14 A**) and different strength of the NMDA synapses (see **Figure 14 B**) the firing rate remained independent of cell length (Cuntz *et al.*, 2021, compare also the *black* dots for the models with only AMPA synapses). Notably, the added non-linearities did not diminish the dendritic constancy principle but consolidated its general rule.

As seen in the mathematical analysis (e.g. **Equation 10** and Cuntz *et al.*, 2021) of the passive dendrites, the somatic voltage for synaptic inputs depends on the average dendritic diameter. The reconstructed diameters are mostly unreliable and were normalized in the preprocessing of the morphologies. Therefore, simulations with original reconstructed diameters were compared to normalized diameters (see **Figure 14 C**). The firing rate varied greatly among different dendrites but remained independent of dendritic length.

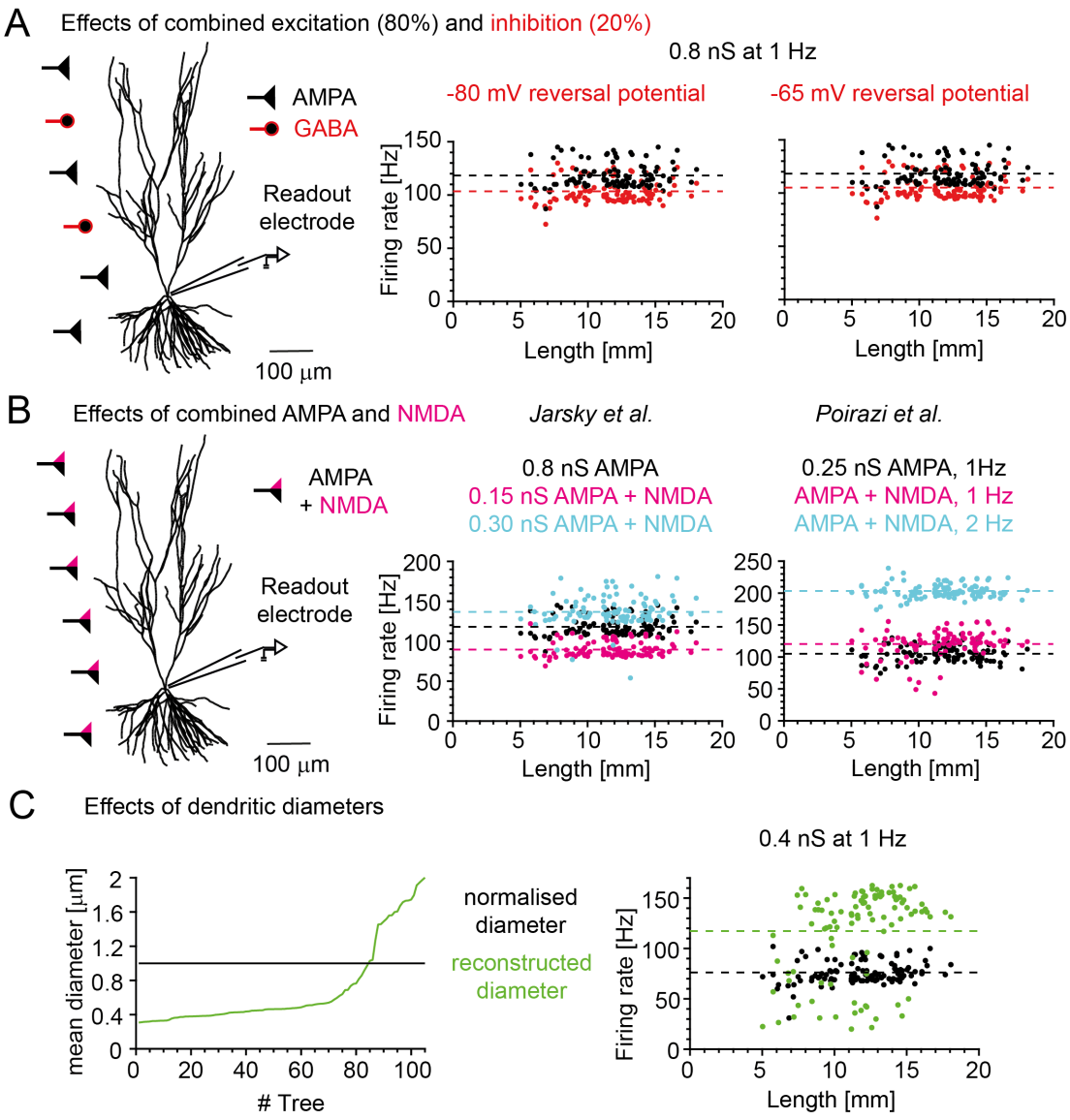

Figure 14. Distributed synaptic inputs to CA1 PC model cells with active biophysics and complex synapses (NMDA, GABA) can lead to similar size-independent responses

A, Example morphology as in **Figure 13** but with inhibitory GABA synapses added. 20% of the total synapses were chosen randomly and turned into GABA synapses by changing the reversal potential to $-80mV$ (*middle red*) and $-65mV$ (*right red*) respectively. Compare the *black* dots showing the pure AMPA stimulation as in **Figure 13**. **B**, Example morphology as in **Figure 13** but with NMDA synapses added to the AMPA synapse locations. Firing rate responses to different AMPA and NMDA strength combinations (*middle*) and input frequencies (*right*) are shown. **C**, Comparison of normalized average dendritic diameter ($1\mu m$, see also **Equation 11** for diameter dependence) to the original (unreliable) diameter reconstruction (in *green*). Panels **A** *middle* and *right* and **C** *right* adapted from "A general principle of dendritic constancy: A neuron's size- and shape-invariant excitability" (Reference: Cuntz *et al.*, 2021, doi: https://doi.org/10.1016/j.neuron.2021.08.028) by Cuntz H, Bird AD, Mittag M, Beining M, Schneider M, Mediavilla L, Hoffmann FZ, Deller T, Jedlicka P in *Neuron, 2021,* and licensed under an Elsevier user license (Copyright Elsevier Inc. 2021, https://www.elsevier.com/about/policies-and-standards/open-access-licenses/elsevier-user).

Finally, a third active ion channel compartmental model was incorporated for cortical PCs. As with the two active hippocampal models, the cortical model by Almog and Korngreen (2014) showed independence of dendritic length and size for several input frequencies of synaptic activation (**Figure 15**, see also Cuntz *et al.*, 2021).

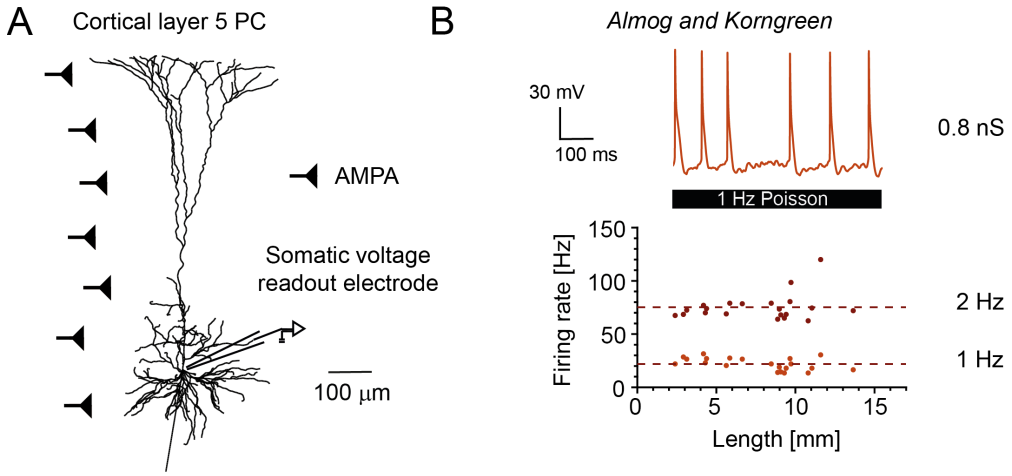

Figure 15. Distributed synaptic inputs to cortical PCs in a model by Almog and Korngreen (2014) lead to size-independent responses

A, Example morphology of a cortical L5 PC from the Korngreen dataset ($n = 20$) available on *NeuroMorpho.Org*. **B**, Firing rate responses to different input frequencies ($1Hz$ *light brown*, $2Hz$ *dark brown*) are depicted.

Panel **B** adapted from "A general principle of dendritic constancy: A neuron's size- and shape-invariant excitability" (Reference: Cuntz *et al.*, 2021, doi: https://doi.org/10.1016/j.neuron.2021.08.028) by Cuntz H, Bird AD, Mittag M, Beining M, Schneider M, Mediavilla L, Hoffmann FZ, Deller T, Jedlicka P in *Neuron, 2021,* and licensed under an Elsevier user license (Copyright Elsevier Inc. 2021, https://www.elsevier.com/about/policies-and-standards/open-access-licenses/elsevier-user).

Table 9. Linear regression and slope of data

Figure panel	**p value**	**slope** $[\%/mm]$	**Figure panel**	**p value**	**slope** $[\%/mm]$
13B Jarsky $0.2nS$	0.004	3.1	13D dendritic $1Hz$	0.09	0.6
13B Jarsky $0.4nS$	0.08	0.9	13D dendritic $3.5Hz$	0.005	3.2
13B Jarsky $0.8nS$	0.19	0.4	14A GABA $E = -80mV$	0.17	0.5
13B Jarsky $2Hz, 0.4$	0.4	-0.2	14A GABA $E = -65mV$	0.14	0.5
13B Jarsky $2Hz, 0.2$	0.3	0.4	14B Jarsky NMDA $0.15nS$	0.28	0.4
13C apical cluster	0.87	-0.2	14B Jarsky NMDA $0.3nS$	0.24	0.5
13C basal cluster	0.3	0.7	14B Poirazi NMDA $1Hz$	0.66	0.2
13C subtree cluster	0.55	1.4	14B Poirazi NMDA $2Hz$	0.99	-0.002
13C patch cluster	0.44	-0.7	14C Jarsky real diameter	0.13	1.8
13D Poirazi $1Hz$	0.37	0.4	15B Korngreen $1Hz$	0.13	-5.1
13D Poirazi $3.5Hz$	0.46	0.1	15B Korngreen $2Hz$	0.92	0.2

Taken together, the results from chapter one of this dissertation demonstrate that the dendritic constancy principle holds for a variety of active compartmental models and cells with realistic biophysics including voltage-dependent ion channels and AMPA, NMDA and GABA synapses (Cuntz *et al.*, 2021). It is a general principle. An important next step is: can it be applied to specific examples? For instance, many neurological pathologies such as AD are characterised by morphological changes. Can the dendritic constancy principle help to investigate the functional effects of these structural changes? This, among other intrinsic and extrinsic AD alterations, is the topic of the next chapter.

5.3 Chapter 2: AD hyperexcitability scenarios in CA1

One of the prominent features of AD pathology is morphological remodeling of the cells in the form of dendritic degeneration (Baloyannis, 2009). Furthermore, it has been observed that the neuronal excitability is increased in AD cells in CA1 (Vossel *et al.*, 2017). This increase is shown predominantly in the boosted burst firing of the cells (Šišková *et al.*, 2014). The question arises if morphological changes and altered firing behaviour of the AD cells are linked together (Mittag *et al.*, 2023). The dendritic constancy results from the previous investigation in chapter one suggest that the altered size of the AD-affected cells should in principle not lead to a change in the IO function. The consequences of dendritic degeneration and the possible causes of hyperexcitability in AD are clearly not yet fully understood. One of the aims of the dissertation in this chapter was therefore to investigate whether dendritic remodeling alone could lead to the experimentally attested simultaneous increase in excitability. In order to examine the IO behaviour, biophysically realistic and anatomically detailed compartmental models were implemented for the reconstructed morphological data provided by the Šišková *et al.* (2014) lab. The data consisted of control (wild type, WT) and APP/PS1 CA1 mouse PCs. An example morphology for each cell group is shown in **Figure 16 A**. Similar to chapter one of this thesis, the cell activity (voltage change or firing rate) is shown versus dendritic path length, whereby the group average is depicted by a dashed line.

5.3.1 Dendritic degeneration alone does not account for synaptically driven hyperexcitability in APP/PS1 CA1 PC models

Firstly, the behaviour of the AD cells for electrically passive dendrites in the context of morphological alterations was investigated. A statistical comparison of morphological measures between WT and APP/PS1 PCs showed clear and significant differences in cell sizes (see **Figure 8** in **Methods**). The simulation result of the passive modelling was, that the observed dendritic degeneration in the APP/PS1 morphology group did not lead to an increase in the somatic voltage responses (**Figure 16 B**, cross markers, see also Mittag *et al.*, 2023). This occurred even though the reduction in cell size generally increases the cell's input resistance and somatic excitability. In fact, the APP/PS1 cell group showed on average a reduced voltage change when compared to the WT group (mean voltage passive model: WT $6.45 \pm 0.67mV$, APP/PS1 $5.74 \pm 0.80mV$, the asterisk depicts $p = 0.000467$).

Secondly, in order to explore neuronal excitability in more realistic and active dendrites, active ion channels from a well established biophysical CA1 PC model were inserted (Poirazi *et al.*, 2003b, ion channel composition in **Figure 10** in **Methods**). A previously established scaling method was used for transferring distance-dependent ion channel densities to multiple CA1 PC morphologies (Cuntz *et al.*, 2021; Mittag *et al.*, 2023). After insertion of active ion channels, the subthreshold behaviour of the neurons in response to synaptic activation showed a reduction and equalising of the voltage responses for both morphology groups (**Figure 16 B**, circle markers, mean voltage subthreshold active model: WT $1.47 \pm 0.17mV$, APP/PS1 $1.41 \pm 0.51mV$, Mittag *et al.*, 2023). In the next step the synaptic activation was increased to reach suprathreshold behaviour, i.e. the cells were spiking. The firing behaviour was comparable across both cell groups, shown by the overlapping firing curves (**Figure 16 C** left) and nearly identical average firing rates (**Figure 16 C** right). Both cell groups displayed no dependency of the firing rate on dendritic length ($0.8Hz$ input: WT $17.35 \pm 5.29Hz$, APP/PS1 $15.40 \pm 7.72Hz$; $4.4Hz$ input: WT $69.91 \pm 7.23Hz$, APP/PS1 $68.29 \pm 9.41Hz$, Mittag *et al.*, 2023) even though at the extreme limit of very small cells the firing was smaller for the $4.4Hz$ input condition. This independence was preserved for other morphological measures such as branch points and surface area (**Figure 16 D**).

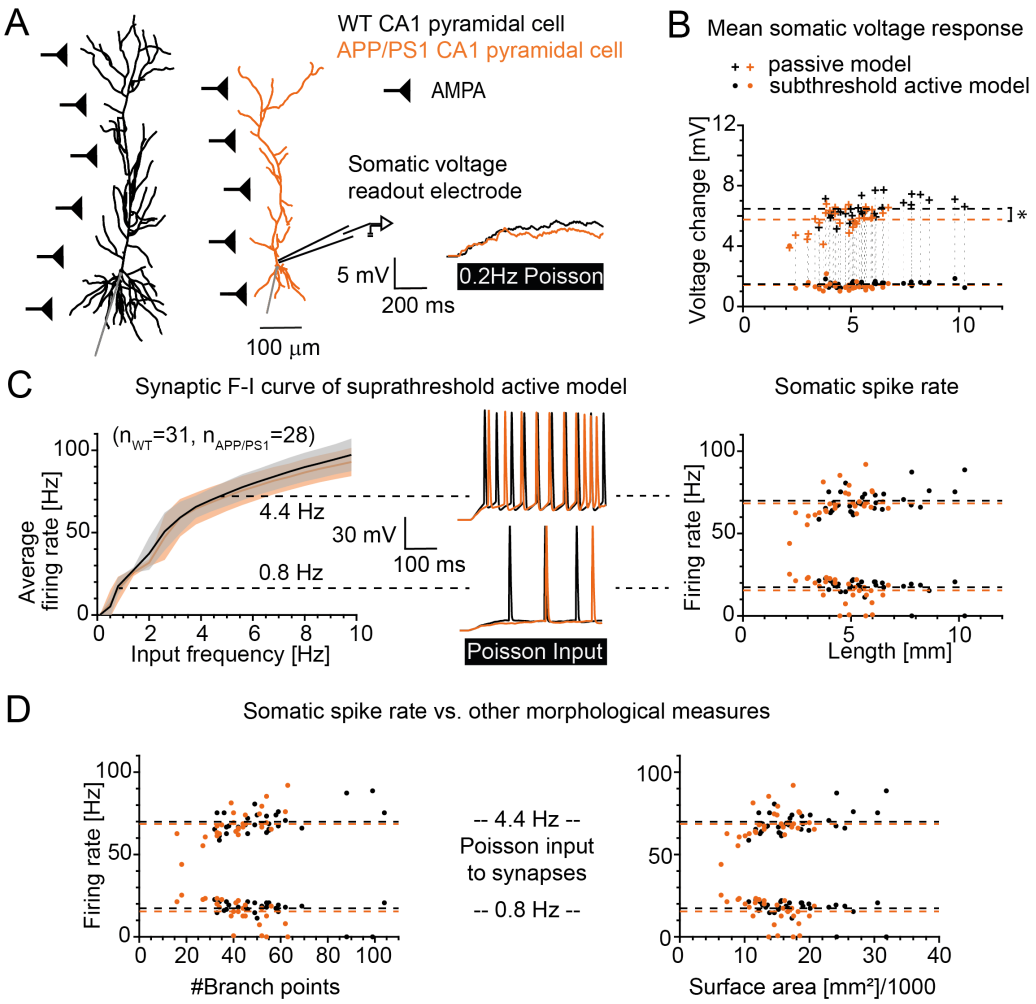

Figure 16. Dendritic degeneration in APP/PS1 model PCs leads to similar responses and does not cause hyperexcitability for distributed synaptic (AMPA) inputs

Combined Figure 7 and Figure 1 C from "Modelling the contributions to hyperexcitability in a mouse model of Alzheimer's disease" (doi: https://doi.org/10.1113/JP283401) by Mittag M, Mediavilla L, Remy S, Cuntz H, Jedlicka P and licensed under CC BY 4.0 (Copyright Mittag *et al.*, 2023, http://creativecommons.org/licenses/by/4.0/): **A**, Morphology examples of reconstructed wildtype (WT, *black*) and APP/PS1 (*orange*) CA1 PCs. AMPA synapses are homogeneously distributed (*black* triangles) and receive Poisson input. **B**, Somatic voltage changes of all cells with respect to their dendritic length after $0.2Hz$ Poisson input to AMPA synapses for the model by Poirazi *et al.* (2003b). WT group is shown in *black* ($n = 31$), APP/PS1 in *orange* ($n = 28$), passive model with *crosses* and the subthreshold active model with *dots*. Throughout the thesis, the dashed lines depict the mean. The asterisk indicates $p = 0.000467$. **C** *Left*, Average somatic firing rate of all WT and APP/PS1 cells versus synaptic input frequency for the active model by Poirazi *et al.* (2003b). Voltage traces with spikes are shown for the two sample cells for input frequencies of $0.8Hz$ and $4.4Hz$. *Right*, Firing rate is plotted against dendritic length for the data points with input frequency of $0.8Hz$ and $4.4Hz$ as seen *left*. **D**, Same data as in **C** *right* but versus number of branch points and surface area.

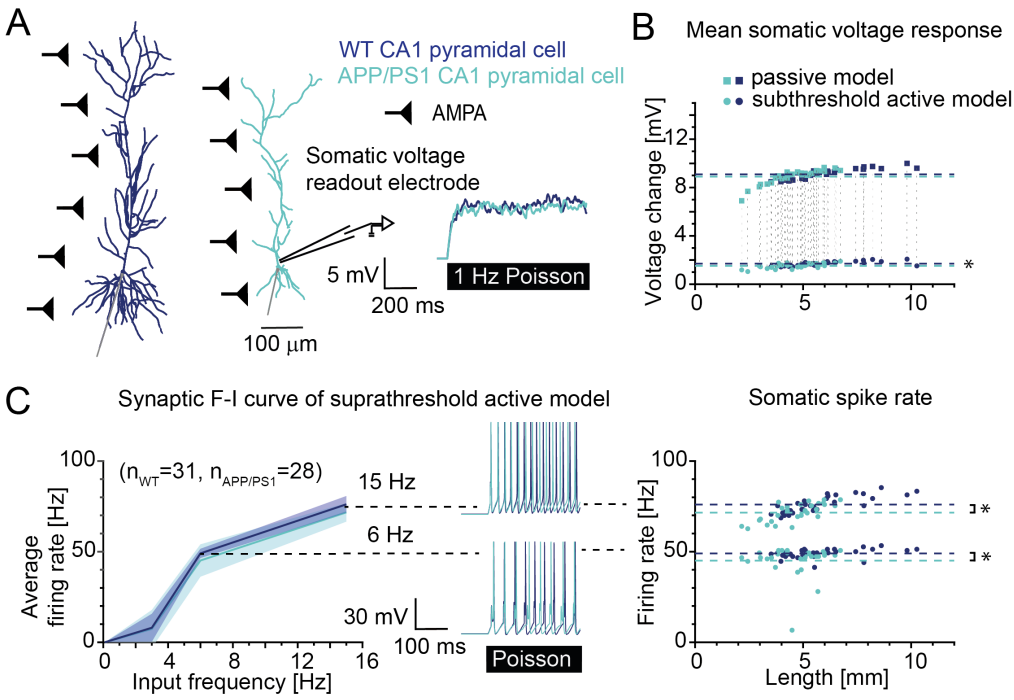

Figure 17. Dendritic degeneration in APP/PS1 PCs with the model by Jarsky *et al.* (2005) does not cause hyperexcitability for distributed synaptic (AMPA) inputs

Reproduced Figure 3 B-E from "Modelling the contributions to hyperexcitability in a mouse model of Alzheimer's disease" (doi: https://doi.org/10.1113/JP283401) by Mittag M, Mediavilla L, Remy S, Cuntz H, Jedlicka P and licensed under CC BY 4.0 (Copyright Mittag *et al.*, 2023, http://creativecommons.org/licenses/by/4.0/): **A**, Same experimental setup as **Figure 16 A** but with ion channel model by Jarsky *et al.* (2005) (WT in *dark blue*, APP/PS1 in *light blue*). The inset shows voltage traces of the two sample cells for the passive model with whole cell distributed AMPA stimulation of $1Hz$ Poisson inputs. **B, C**, Same passive and active model simulations as in **Figure 16 B, C** depicting voltage change response and firing rate versus dendritic length and input frequency respectively with the model by Jarsky *et al.* (2005). Mean voltage passive model: WT $9.11 \pm 0.43mV$, APP/PS1 $8.91 \pm 0.64mV$; mean voltage subthreshold active model: WT $1.69 \pm 0.18mV$, APP/PS1 $1.53 \pm 0.22mV$, the asterisk depicts $p = 0.00360$; output firing rate to $6Hz$ input: WT $49.05 \pm 2.52Hz$, APP/PS1 $45.12 \pm 8.9Hz$, $p = 0.0217$; $15Hz$ input: WT $76.11 \pm 4.58Hz$, APP/PS1 $71.66 \pm 5.07Hz$, $p = 0.000817$.

In summary, the results from whole-cell synaptic activation show that the dendritic degeneration observed in the APP/PS1 group does not lead to a stronger synaptic integration for either the passive or active neuron model, when compared to their WT counterparts. These results were further confirmed by using a second and simpler CA1 PC biophysical model (Jarsky *et al.*, 2005, **Figure 17**). Taken together, these results suggest that other mechanisms are necessary to account for the cellular hyperexcitability observed in the APP/PS1 mouse model (Mittag *et al.*, 2023).

5.3.2 Dendritic degeneration can affect CA1 PC excitability by selective gating of layer-specific inputs

Previous research has shown that some dendritic subregions are affected by dendritic degeneration more than others. For example, basal dendrites are generally lost before the more peripheral portions of the apical tree in CA1 PCs (Scheibel, 1979; Šišková *et al.*, 2014). These observations open the question whether subregion-specific dendritic degeneration leads to a change in CA1 PC behaviour in response to layer-specific input pathways. To address this, a more realistic distribution of synaptic inputs based on anatomical synaptic data was implemented: layer-specific synapse densities as well as distance-dependent and lognormal synaptic weight distributions were incorporated based on Magee and Cook (2000); Megías *et al.* (2001); Katz *et al.* (2009); Šišková *et al.* (2014); Kim *et al.* (2015); Bloss *et al.* (2016). NMDA and GABA synapses were added to the AMPA synapses; a weight distribution example for AMPA is shown in the schematic in **Figure 18 A** *right insets*. Three major layer-specific input pathways to the CA1 cells were explored: the perforant pathway and the apical and basal Schaffer collateral pathways (**Figure 18 C**, *top*).

Initially, only synaptic background activity (Poisson-like) targeting all dendritic regions did not lead to an increased excitability in the APP/PS1 cell group. Moreover, the spiking behaviour still remained independent from the cell's dendritic length (**Figure 18 B**, WT $25.24 \pm 6.74 Hz$, APP/PS1 $23.69 \pm 3.87 Hz$; see comparison with **Figure 16 C)**.

In order to simulate the input coming from each different pathway, correlated synaptic activity was introduced, separately targeting layer-specific subregions within the dendritic tree. In this way, "clustered" synaptic activation coming from particular input pathways could be studied (Mittag *et al.*, 2023). Would they lead to a difference in the response behaviour between the two morphology groups? Thus, rhythmic activation of the synapses was simulated in each of the three input areas (EC input, CA3 input to oblique and basal dendrites, see **Figure 18 C, D**) at a theta frequency ($5 Hz$), which resembled a prominent behavioural input pattern received by the hippocampus (Bannister and Larkman, 1995; Megías *et al.*, 2001; Ang *et al.*, 2005; Manns *et al.*, 2007; Takahashi and Magee, 2009; López-Madrona *et al.*, 2021).

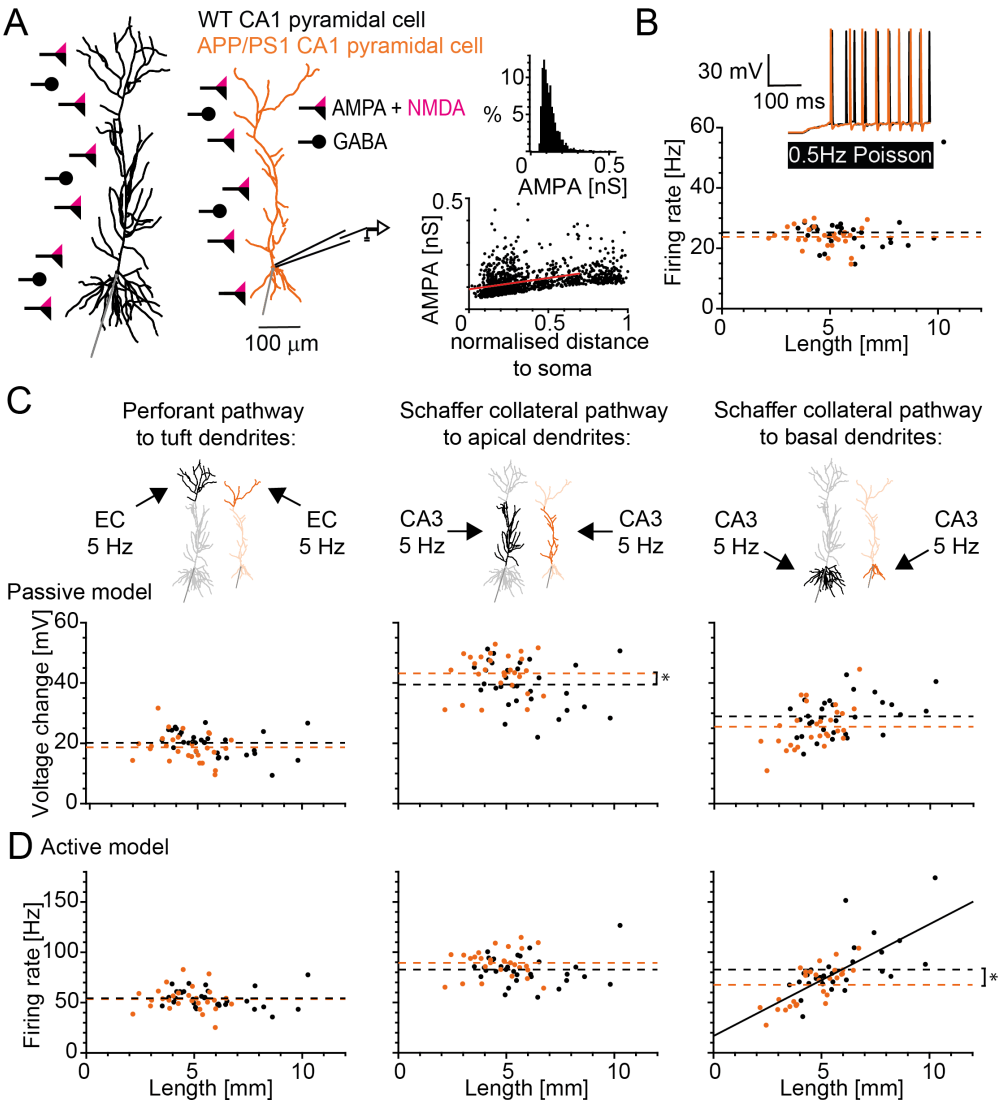

Figure 18. Dendritic degeneration can cause alterations in excitability in APP/PS1 model cells via input gating for synaptic activation (AMPA, NMDA and GABA) of the major layer-specific pathways

Reproduced Figure 8 from "Modelling the contributions to hyperexcitability in a mouse model of Alzheimer's disease" (doi: https://doi.org/10.1113/JP283401) by Mittag M, Mediavilla L, Remy S, Cuntz H, Jedlicka P and licensed under CC BY 4.0 (Copyright Mittag *et al.*, 2023, http://creativecommons.org/licenses/by/4.0/): **A**, Example cells of CA1 PCs (WT in *black*, APP/PS1 in *orange*) with AMPA (*black triangle*), NMDA (*magenta triangle*) and GABA (*black circle*) synapses. *Right* shows the distribution of AMPA strengths regarding distance to the soma. **B**, Firing rate responses vs. dendritic length of WT and APP/PS1 PCs for synaptic Poisson input stimulation at $0.5Hz$ in an active model by Poirazi *et al.* (2003b). **C**, Voltage change responses vs. dendritic length of WT and APP/PS1 PCs for three pathway stimulations (Perforant pathway, Schaffer collateral apical and basal pathway) of $5Hz$ for the passive model by Poirazi *et al.* (2003b). The dashed lines show the mean voltage responses (the asterisk depicts $p = 0.0456$). **D**, Same as in **C** but for the active model by Poirazi *et al.* (2003b). Firing rate responses vs. dendritic length of WT and APP/PS1 PCs. The dashed lines show the mean firing rate (the asterisk depicts $p = 0.0169$).

The passive cell model without active channels was used first and the response to the different input pathways was investigated (**Figure 18 C**). It resulted in similar voltage changes for passive WT and APP/PS1 cells evoked by the perforant pathway stimulation (**Figure 18 C**, *Left panel:* WT $20.12 \pm 4.05mV$, APP/PS1 $18.68 \pm 4.72mV$). However, when stimulating the Schaffer collateral inputs on the apical dendrites, the results were slightly larger voltage changes in the APP/PS1 cell group (**Figure 18 C**, *Middle panel:* WT $39.48 \pm 7.63mV$, APP/PS1 $43.26 \pm 6.48mV$; $p = 0.0456$). Interestingly, this behaviour was reversed for the voltage change caused by the Schaffer collateral inputs to the basal dendrites (**Figure 18 C**, *Right panel:* WT $28.86 \pm 6.31mV$, APP/PS1 $25.53 \pm 7.10mV$, $p = 0.0618$). The insertion of active conductances into the cell model (Poirazi *et al.*, 2003b) was the next step and it led to comparable results as for the passive model case (compare **Figure 18 C** and **Figure 18 D**). The perforant pathway input resulted in similar firing rates across the WT and APP/PS1 cell groups (**Figure 18 D**, *Left panel:* WT $54.07 \pm 9.38Hz$, APP/PS1 $53.62 \pm 12.47Hz$). For the apical Schaffer collateral pathway, the APP/PS1 cells displayed marginally larger firing rates when compared to the WT cells (**Figure 18 D**, *Middle panel:* WT $84.38 \pm 14.44Hz$, APP/PS1 $90.31 \pm 13.27Hz$, $p = 0.107$). In contrast, the Schaffer collateral inputs to the basal dendrites led to a strong correlation between the cell's firing rate and dendritic length, displaying a significant decrease in the average firing rate in APP/PS1 neurons when compared to WT controls (**Figure 18 D**, *Right panel:* WT $82.44 \pm 27.70Hz$, APP/PS1 $67.11 \pm 18.79Hz$, asterisk depicts $p = 0.0169$, see also Mittag *et al.*, 2023).

A possible explanation for these pathway-dependent differences in somatic excitability could be due to the variability found in basal/apical dendritic length ratios across the data set (**Figure 19 A**, mean ratio WT 0.55 ± 0.26, APP/PS1 0.39 ± 0.22, asterisk depicts $p = 0.0126$). A cell with a smaller basal/apical ratio receives relatively less basal input per total dendritic length, and experiences a larger inactivated apical region that acts as a voltage sink, which could then lead to the differences in the firing output (Mittag *et al.*, 2023).

For the purpose of testing this idea, morphological modelling was performed via scaling of the WT and APP/PS1 cell morphologies to a fixed $30/70$ basal/apical ratio (**Figure 19 A**, *right panel, purple*). After this structural scaling, the strong correlation between the cell's output and dendritic length was lost, leading to an almost identical average voltage change and firing rate for both morphology groups (**Figure 19 B**, *left*: perforant pathway, WT $18.99 \pm 4.02mV$, APP/PS1 $16.93 \pm 3.91mV$, *middle*: apical Schaffer collateral, WT $41.15 \pm 8.88mV$, APP/PS1

$41.09 \pm 7.73mV$, *right*: basal Schaffer collateral, WT $28.88 \pm 7.25mV$, APP/PS1 $28.92 \pm 7.10mV$ and **Figure 19 C**, *left*: perforant pathway, WT $52.18 \pm 9.34Hz$, APP/PS1 $52.40 \pm 11.79Hz$, *middle*: apical Schaffer collateral, WT $87.28 \pm 16.62Hz$, APP/PS1 $87.33 \pm 12.12Hz$, *right*: basal Schaffer collateral, WT $78.02 \pm 23.16Hz$, APP/PS1 $80.10 \pm 20.41Hz$, Mittag *et al.*, 2023).

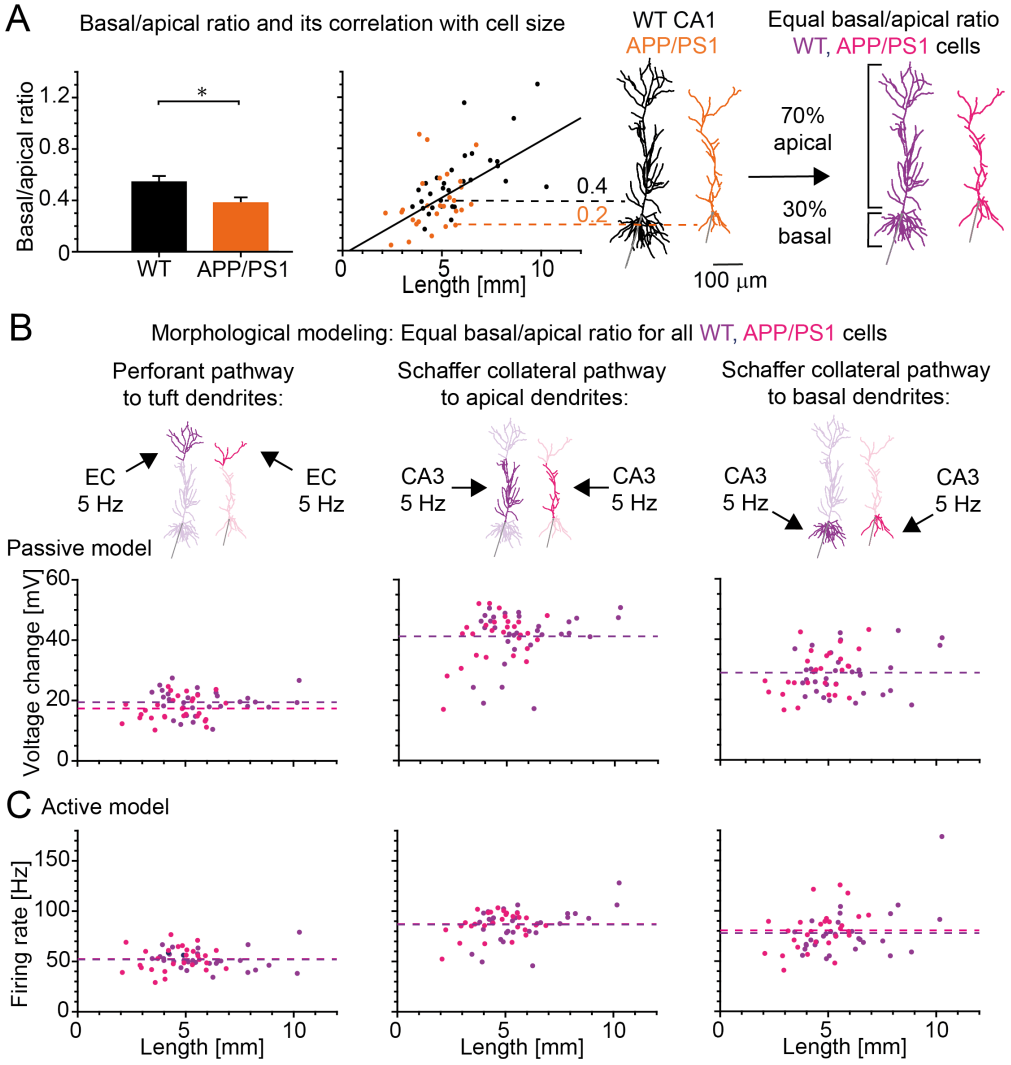

Figure 19. Equalizing the ratio of basal/apical dendrite length equalizes the responses of WT and APP/PS1 model cells for the synaptic activation of the major input pathways

Reproduced Figure 9 from "Modelling the contributions to hyperexcitability in a mouse model of Alzheimer's disease" (doi: https://doi.org/10.1113/JP283401) by Mittag M, Mediavilla L, Remy S, Cuntz H, Jedlicka P and licensed under CC BY 4.0 (Copyright Mittag *et al.*, 2023, http://creativecommons.org/licenses/by/4.0/): **A**, *Left*: Different basal/apical ratio between WT and APP/PS1 cells due to denervation (asterisk depicts $p = 0.0126$). *Middle*: The basal/apical ratio vs. total dendritic length. *Right*: PCs remodeled to have equal basal/apical ratio (30%/70%) for all morphologies (*dark purple*: WT, *light purple*: APP/PS1). **B, C**, as in **Figure 18 C, D** for remodeled morphologies with equal basal/apical ratio (30%/70%).

Overall, the results in **Figure 18** and **Figure 19** indicate that the stronger degeneration of basal dendrites compared to apical dendrites observed in APP/PS1 cells may lead to increased firing as a response to the activation of CA3 Schaffer collateral inputs on the oblique dendrites, while leading to decreased firing as a response to the activation of CA3 Schaffer collateral inputs on the basal dendrites (Mittag *et al.*, 2023). Importantly though, the APP/PS1 cells had no significant increase in firing for the active models, in particular, no burst increase was shown. Taken together, these results suggest that the morphological changes observed in AD are not responsible for the concurrent increase in firing and bursting. It follows, that other mechanisms are necessary to account for the hyperexcitability (Mittag *et al.*, 2023). These mechanisms are investigated in the next section.

5.3.3 Concomitant network and intrinsic cell changes lead to enhanced excitability in APP/PS1 cells

Although dendritic degeneration can modulate CA1 PC excitability by selectively gating layer-specific inputs, it cannot fully account for the hyperexcitability observed in APP/PS1 mice (Mittag *et al.*, 2023). Besides the discussed morphological changes, pathological alterations in the network input as well as in the intrinsic properties of APP/PS1 CA1 PCs could be responsible for their enhanced firing and bursting. Thus, the focus of the next investigation in this dissertation was to clarify the relative contribution of changes in the E/I balance and ion channel densities in order to predict which changes may be most relevant for AD. The computational analysis was able to disentangle the various mechanisms for hyperexcitability previously observed in AD mouse models (Mittag *et al.*, 2023).

The transition in the firing mode of pyramidal neurons from solitary spiking to burst firing is the most important feature of the increased firing in AD-related cells and has been shown experimentally (Chen, 2005; Minkeviciene *et al.*, 2009; Kellner *et al.*, 2014; Berridge, 2014; Ghatak *et al.*, 2019; Müller *et al.*, 2021). This shift of the firing mode towards spike bursts has been previously detected in CA1 PCs in the APP/PS1 mouse model of AD (Šišková *et al.*, 2014). Nevertheless, the mechanism for this is unclear. So far, the results in this chapter showed that morphological changes alone cannot fully explain cellular hyperexcitability in AD mouse models. Alternatively, the effects of several different configurations of AD-related changes and all their possible combinations potentially leading to hyperexcitability and especially enhanced bursting were investigated: observed extrinsic alterations of excitatory, inhibitory or network inputs as well as intrinsic alterations of ion channel densities (Mittag *et al.*, 2023).

The goal was to identify those scenarios that could explain the observed findings in Šišková *et al.* (2014). Therefore, each configuration (eleven in total, **Figure 20** D, middle) was quantified using an error function (root-mean-squared error: **Equations 26-28**) that compared the *in silico* results with existing data regarding firing rate and mode (Šišková *et al.*, 2014; compare **Table 2** and **Figure 20**). Following this approach, it was eventually possible to identify three scenarios where an increased burst firing was observed without changes in solitary spike firing (**Figure 21 A-C**), as shown experimentally in APP/PS1 PCs in mice. These three scenarios are detailed below (see also Mittag *et al.*, 2023).

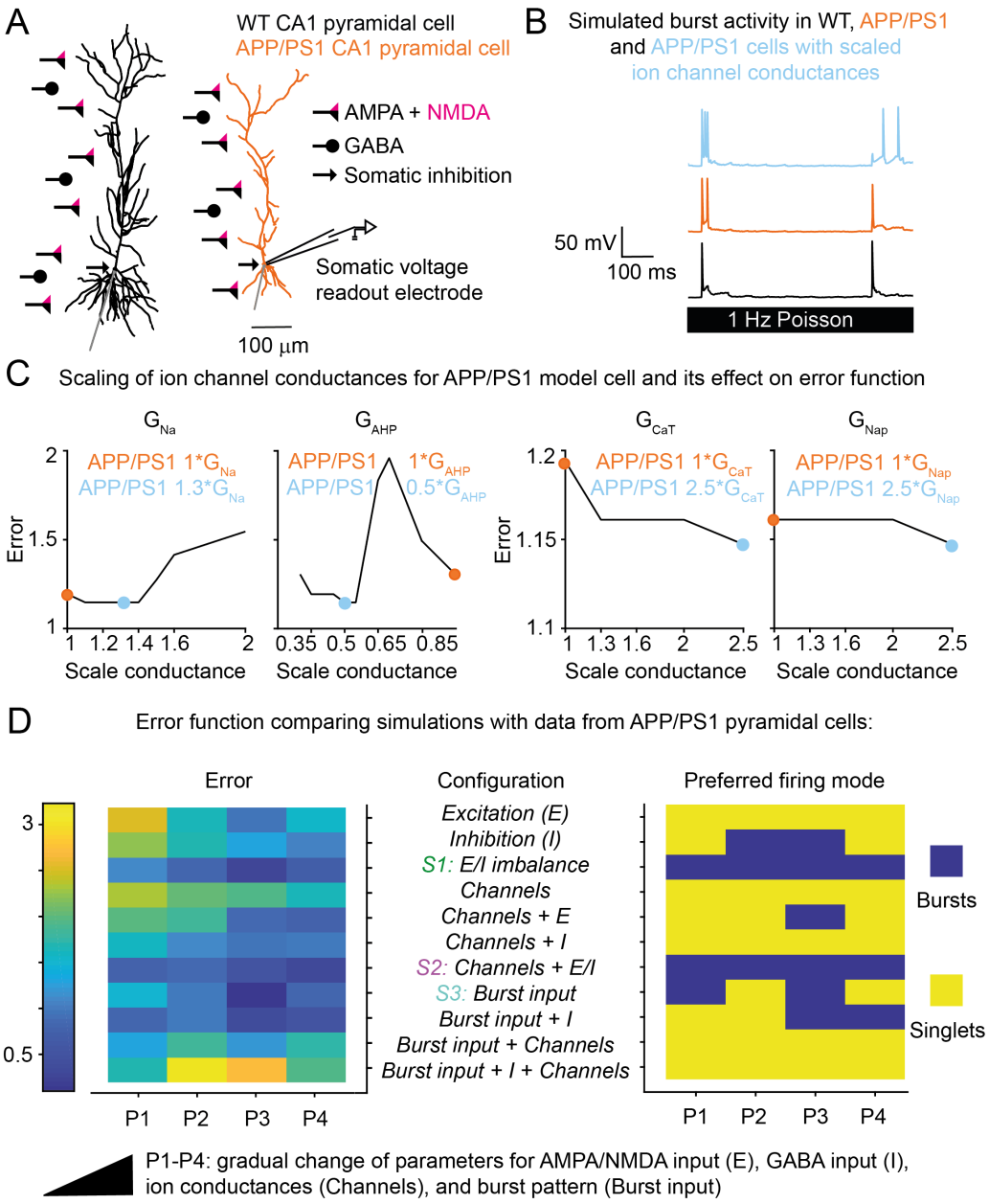

Figure 20. Systematic examination of AD-related extrinsic and intrinsic alterations that potentially cause enhanced burst firing in APP/PS1 model cells

Reproduced Figure 10 from "Modelling the contributions to hyperexcitability in a mouse model of Alzheimer's disease" (doi: https://doi.org/10.1113/JP283401) by Mittag M, Mediavilla L, Remy S, Cuntz H, Jedlicka P and licensed under CC BY 4.0 (Copyright Mittag *et al.*, 2023, http://creativecommons.org/licenses/by/4.0/): **A**, *Left*: **A**, Same example morphologies and model setup as in **Figure 18 A** with GABA synapses inhibiting the soma region as well. **B**, Voltage responses (traces) of WT (*black*), APP/PS1 (*orange*) and APP/PS1 morphology with modified ion channels (*blue*) for $1Hz$ Poisson activation. **C**, An error function was introduced (**Equations 26-28**, see also **Table 2**, small error equals small distance to data). Here, the error function is shown for the firing rate responses for APP/PS1 cells with changes in the ion channel conductances (i.e. I_{Na}, I_{AHP}, I_{CaT} and I_{Nap} channels). The original conductance is indicated in *orange* and the conductance leading to the smallest error in *blue*. **(See next page)**

Figure 20. (continued) D, Error function matrix (*left*) and matrix of preferred firing mode (*right*) for all configurations (11 rows) of intrinsic and extrinsic model modifications (*middle*). The model scan covers 4 incremental changes in parameters (P1 to P4 columns, details in **Methods**). The highlighted configurations S1, S2 and S3 show a good match with data (low error left) with a simultaneous transition to preferred burst firing in APP/PS1 cells (right). Ion channel modifications alone (**C** and 4th row in **D**) do not fully account for the data, especially there is no change in firing mode (right).

Scenario 1: Increased E/I ratio with increased excitatory and decreased inhibitory input

Enhancement of excitatory glutamatergic transmission (Busche and Konnerth, 2016; Zott *et al.*, 2019) as well as impairment of inhibitory GABAergic transmission have been shown to contribute to neuronal network dysfunction in AD (Busche *et al.*, 2008; Schmid *et al.*, 2016; Palop and Mucke, 2016; Ambrad Giovannetti and Fuhrmann, 2019; Xu *et al.*, 2020; Hijazi *et al.*, 2020; Gervais *et al.*, 2022; Ruiter *et al.*, 2020; Melgosa-Ecenarro *et al.*, 2022). Based on an incremental parameter scan (**Figure 20 D**), an increased E/I ratio (*E/I imbalance*) due to reduced GABAergic inhibition combined with enhanced glutamatergic input was able to reproduce experimental data (Šišková *et al.*, 2014, **Table 2**). Consequently, this configuration was identified as a successful *Scenario 1 (green)*. In contrast, the configurations of increased *Excitation* and decreased *Inhibition* could not separately reproduce the data with low errors (**Figure 20 D**, *left*), although a decrease of GABAergic inhibition alone led to a shift in the preferred firing mode towards bursts (**Figure 20 D**, *right*), with a modestly increased firing rate. In Scenario 1 the overall firing rate (**Figure 21 A**, *Left*: WT $3.35 \pm 1.87Hz$, APP/PS1 $2.46 \pm 1.48Hz$, P3 of APP/PS1 in Scenario 1 $9.42 \pm 3.76Hz$ with $p < 1 \cdot 10^{-4}$) and especially the number of bursts (**Figure 21 A**, *Middle*: WT $0.68 \pm 0.59Hz$, APP/PS1 $0.52 \pm 0.52Hz$, P3 of APP/PS1 in Scenario 1 $1.98 \pm 0.65Hz$ with $p < 1 \cdot 10^{-4}$) were significantly increased in the modified APP/PS1 cell group without affecting the single spike rate (**Figure 21 A**, *Middle*: WT $1.40 \pm 0.99Hz$, APP/PS1 $1.09 \pm 0.56Hz$, P3 of APP/PS1 in Scenario 1 $1.67 \pm 0.98Hz$) exactly as reported in experiments of Šišková *et al.* (2014). The rate of triplets for the parameter configuration P3 (**Figure 21 A**, *Right*: WT $0.23 \pm 0.34Hz$, APP/PS1 $0.08 \pm 0.25Hz$, P3 of APP/PS1 in Scenario 1 $0.44 \pm 0.49Hz$ with $p = 0.0964$ compared to WT) was not significantly higher but the trend was similar to the data in Šišková *et al.* (2014). Interestingly, it could be significantly increased with a simultaneous increase in single spike rate in the parameter configuration $P4$ (**Figure 21 A**: singlets $2.07 \pm 1.11Hz$ with $p = 0.0146$, triplets $0.5 \pm 0.44Hz$ with $p = 0.0143$). Thus, given its successful replication of the transition to the bursting mode (**Figure 20 D**, *right*), Scenario 1 with the parameter configuration $P3$ was found to provide a

good qualitative and a medium quantitative match with data (Mittag *et al.*, 2023).

Scenario 2: Increased extrinsic E/I ratio plus intrinsic ion channel alterations

Alterations of ion channel contributions constitute another potential mechanism of AD-associated neuronal hyperexcitability (Yaari *et al.*, 2007; Beck and Yaari, 2008; Zhang *et al.*, 2014; Wang *et al.*, 2015a,b; Liu *et al.*, 2015; Wang *et al.*, 2016; Ghatak *et al.*, 2019; Niday and Bean, 2021; Garg *et al.*, 2021). A targeted parameter scan and sensitivity analysis for the up- or downscaling of four ion channel conductances known to play a role in AD-linked hyperexcitability was performed (see **Methods**). Importantly, the simulation results confirmed the findings from previous experimental studies: by decreasing the I_{AHP} channel density and increasing the density of I_{Nap}, I_{Na} and I_{CaT} channels in sample APP/PS1 morphologies, the output firing rate and burst rate increased, leading to a minimum in the error function (**Figure 20 C**, marked with *blue circles*). The corresponding channel values for the minimized error were applied to all APP/PS1 morphologies and the four ion channel conductances were scaled accordingly (incremental scaling P1-P4 in the configuration *Channels* in **Figure 20 D**, *left*). This led to enhanced firing rates and burst rates, but not to a transition from solitary to burst firing, even when the conductances were scaled to extreme values (**Figure 20 D**, *right*). However, in combination with the change in *E/I* balance, the ion channel modifications were able to reproduce the experimental data (*Channels plus E/I* in **Figure 20 D**, compare **Table 2**). Therefore, this configuration was identified as a successful *Scenario 2 (purple)*. Similarly as in Scenario 1, also in Scenario 2 the overall firing rate (**Figure 21 B**, *Left*: WT $3.35 \pm 1.87Hz$, APP/PS1 $2.46 \pm 1.48Hz$, P4 of APP/PS1 in Scenario 2 $8.96 \pm 3.51Hz$ with $p < 1 \cdot 10^{-4}$) and burst rate were increased (**Figure 21 B**, *Middle*: WT $0.68 \pm 0.59Hz$, APP/PS1 $0.52 \pm 0.52Hz$, P4 of APP/PS1 in Scenario 2 $1.88 \pm 0.63Hz$ with $p < 1 \cdot 10^{-4}$). At the same time, in line with data from Šišková *et al.* (2014), the single spike rate remained similar (**Figure 21 B**, *Middle*: WT $1.40 \pm 0.99Hz$, APP/PS1 $1.09 \pm 0.56Hz$, P4 of APP/PS1 in Scenario 2 $1.60 \pm 0.66Hz$). Interestingly and most importantly, compared to the previous Scenario 1, changes in the intrinsic excitability added to changes in *E/I* led to a significant boost in the triplet firing frequency (**Figure 21 B**, *Right*: WT $0.23 \pm 0.34Hz$, APP/PS1 $0.08 \pm 0.25Hz$, P4 of APP/PS1 in Scenario 2 $0.56 \pm 0.60Hz$ with $p = 0.0125$), which improved the quantitative match with electrophysiological data (Šišková *et al.*, 2014, Mittag *et al.*, 2023, and **Table 2**).

Scenario 3: Increased excitatory network burst input

The PCs of the hippocampal CA1 region do not exist in isolation but are embedded in a wider network. Parts of the network can show hyperexcitability before the pathology propagates to other parts (Palop and Mucke, 2016; Zott *et al.*, 2018; Selkoe, 2019; Kazim *et al.*, 2021). For instance, it has been shown that EC or CA3 hyperactivity can occur during AD pathology (Khan *et al.*, 2013; Angulo *et al.*, 2017; Petrache *et al.*, 2019) and possibly spread towards its post-synaptic CA1 area. As a consequence of these observations, increased network activity with enhanced bursting was examined and whether it would transfer to increased burst firing in model neurons (configuration *Burst input* in **Figure 20 D**). The simulations revealed that presynaptic input spike trains containing bursts (P3 in **Figure 21 C**, *Top*) could evoke CA1 PC responses that were consistent with experimental data (**Table 2**). Consequently, this configuration was identified as a successful *Scenario 3 (turquoise)*. The output pattern was sensitive to the input pattern inasmuch as one less burst or one more singlet in the input spike train (P2 and P4 in **Figure 21 C**, *Top*) failed to provoke a firing mode change towards bursts (**Figure 20 D**, *right*). Modifications in network activity in Scenario 3 on average led to an increase of firing frequency in APP/PS1 cells, when compared to the behaviour of the cell groups with a non-hyperexcitable (control) network input (**Figure 21 C**, *Left*: WT $4.74 \pm 2.08Hz$, APP/PS1 $3.65 \pm 1.43Hz$, P3 of APP/PS1 in Scenario 3 $7.89 \pm 2.36Hz$ with $p < 1 \cdot 10^{-4}$). This overall increase in the cell's excitability was due to a transition from solitary action potentials ($1APs$) to burst firing of more than one AP (**Figure 20 D**, *Right* and **Figure 21 C**, *Middle*: WT $1.02 \pm 0.51Hz$, APP/PS1 $0.83 \pm 0.48Hz$, P3 of APP/PS1 in Scenario 3 $1.99 \pm 0.69Hz$ with $p < 1 \cdot 10^{-4}$). Most notably, in line with experimental data in Šišková *et al.* (2014), a significant increase of the number of triplets was displayed (**Figure 21 C**, *Right*: WT $0.32 \pm 0.35Hz$, APP/PS1 $0.38 \pm 0.32Hz$, P3 of APP/PS1 in Scenario 3 $0.79 \pm 0.62Hz$ with $p = 3.64 \cdot 10^{-4}$), while the single AP firing rate remained constant (**Figure 21 C**, *Middle*: WT $1.66 \pm 0.68Hz$, APP/PS1 $1.32 \pm 0.58Hz$, P3 of APP/PS1 in Scenario 3 $1.43 \pm 0.83Hz$). This indicates a change of firing mode from predominantly single spikes to burst firing in APP/PS1 cells with increased network activity input in Scenario 3 ($p_{1AP,>1AP} = 0.00801$, Mittag *et al.*, 2023). Interestingly, bursty input in combination with reduced inhibition (*Burst input plus inhibition*) yielded comparable results to the ones observed for the bursts alone (**Figure 20 D**). This configuration can be seen as a particular version of *E/I imbalance* with the increased excitatory input due to bursts.

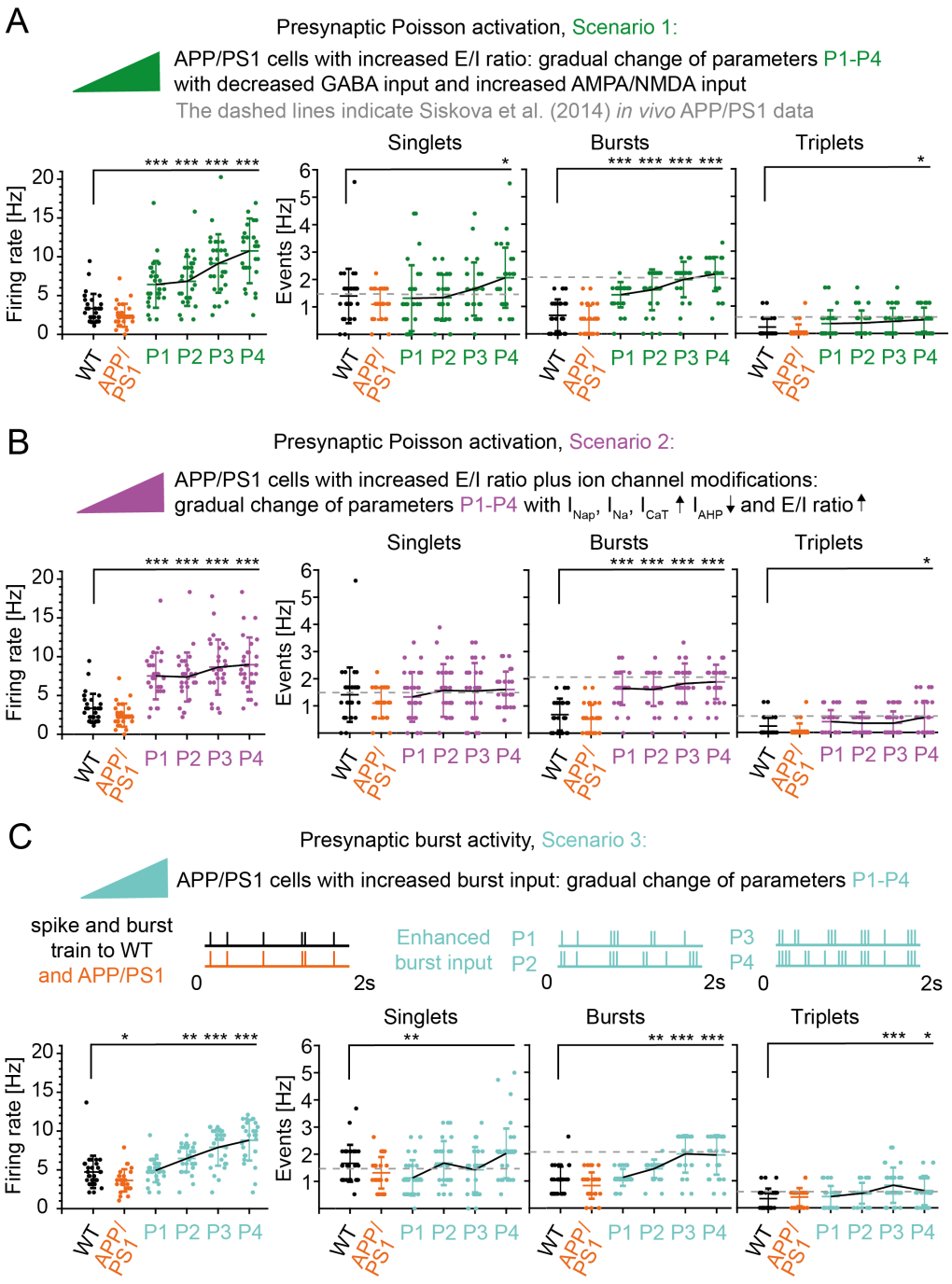

Figure 21. Hyperexcitability and transition to preferred burst firing mode in APP/PS1 cells in consequence to extrinsic (network) and accompanied by intrinsic neuronal alterations

Reproduced Figure 11 from "Modelling the contributions to hyperexcitability in a mouse model of Alzheimer's disease" (doi: https://doi.org/10.1113/JP283401) by Mittag M, Mediavilla L, Remy S, Cuntz H, Jedlicka P and licensed under CC BY 4.0 (Copyright Mittag *et al.*, 2023, http://creativecommons.org/licenses/by/4.0/): **A**, Scenario 1: Overall firing rate, single APs, bursts ($> 1AP$, $ISI \leq 13.3ms$) and triplets ($3APs$) in WT (*black*), APP/PS1 (*orange*) and in APP/PS1 PCs with gradually increased E/I ratio (P1-P4, *green*, details in **Methods**). **(See next page).**

Figure 21. (continued) B, Scenario 2: Overall firing rate, single APs, bursts and triplets in WT (*black*), APP/PS1 (*orange*) and APP/PS1 PCs with gradually increased E/I ratio plus experimentally observed ion channel changes (P1-P4, *purple*: increased I_{Nap}, I_{Na}, I_{CaT} densities, decreased I_{AHP} density). **C**, Scenario 3: Overall firing rate, single APs, bursts and triplets in WT (*black*), APP/PS1 (*orange*) and APP/PS1 PCs with gradually increased burst input (P1-P4, *turquoise*). *Top*, exact input pattern of singlets, doublets, triplets and quadruplets for P1-P4 conditions. Throughout the figure the dashed lines in *grey* indicate the mean event rate according to Šišková *et al.* (2014), the single asterisk indicates a significant value of $p < 0.05$, two asterisks indicate $p < 0.01$ and three asterisks indicate $p < 0.001$.

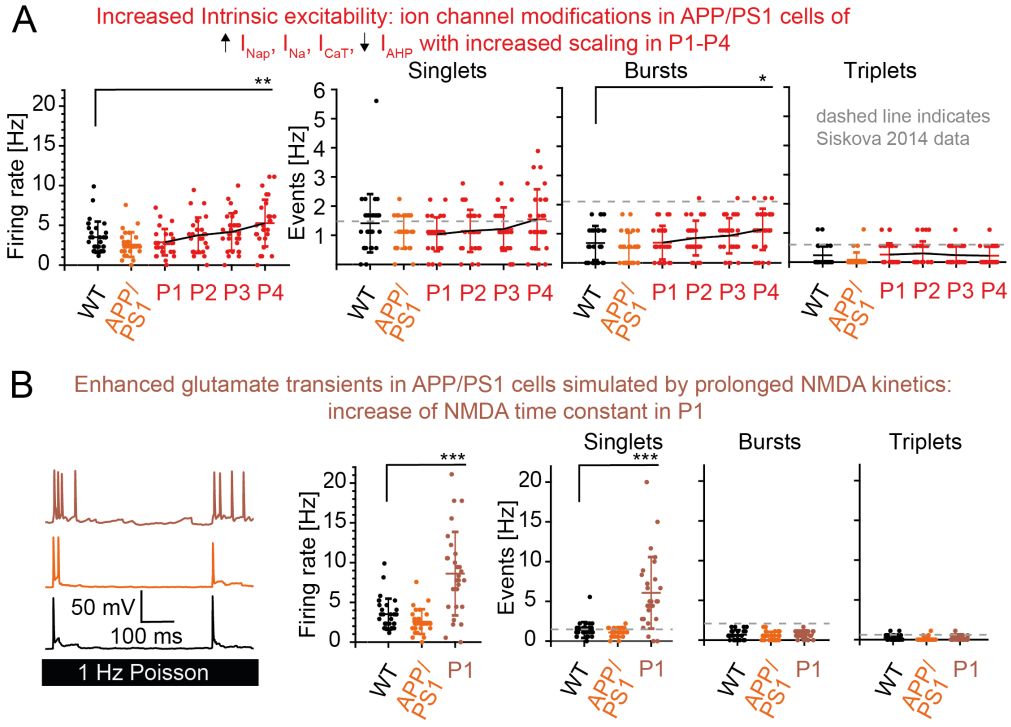

Figure 22. Enhanced burst firing but no transition to preferred burst mode in APP/PS1 PCs in consequence to isolated ion channel modifications and no increase in burst firing for extended NMDA kinetics

Reproduced Figure 4 from "Modelling the contributions to hyperexcitability in a mouse model of Alzheimer's disease" (doi: https://doi.org/10.1113/JP283401) by Mittag M, Mediavilla L, Remy S, Cuntz H, Jedlicka P and licensed under CC BY 4.0 (Copyright Mittag *et al.*, 2023, http://creativecommons.org/licenses/by/4.0/): **A**, Overall firing rate, single APs, bursts ($> 1AP$) and triplets in WT (*black*), APP/PS1 (*orange*) and APP/PS1 PCs with intrinsic ion channel modifications (P1-P4, *red*: increased I_{Nap}, I_{Na}, I_{CaT} channel densities, decreased I_{AHP} density; see details in **Table 6**). The asterisks denote a significant increase in firing rate ($p = 0.00301$) and burst rate ($p = 0.0112$) between WT and P4 configuration. **B**, *Left*, Examples of voltage traces for WT (*black*), APP/PS1 (*orange*) and APP/PS1 PCs with enhanced NMDA decay time constant ($P1$, *brown*: $\tau_{P1,NMDA} = 2 \cdot \tau_{WT,NMDA}$). *Middle*, Overall firing rate, single APs, bursts and triplets of the *left* cell groups. The asterisks denote $p < 0.0001$ for increased single spike rate and overall firing rate between WT and P1 configuration with increased NMDA decay.

In the configuration *Channels*, with solely modifications to the ion channel conductances, the firing rate and burst rate were enhanced with increased scaling of ion channels (see $P4$ in **Figure 22 A**: the asterisks denote $p = 0.00301$ and $p = 0.0112$ for firing rate and burst rate, respectively), though, importantly, no mode change towards bursts was noticed (Mittag *et al.*, 2023) even when scaling the conductances to extreme values (compare also **Figure 20 D**, right).

In addition, control simulations were performed by applying the same AD-related ion channel and network modifications from above to all of the WT morphologies as well. As a result, an even higher increase in burst firing than in APP/PS1 morphologies could be registered for the different scenarios (see **Figure 23**: extrinsic changes in Scenario 1 for WT $2.22 \pm 0.85Hz$ and APP/PS1 $1.61 \pm 0.75Hz$, $p = 0.00469$; and extrinsic/intrinsic changes in Scenario 2 for WT $2.46 \pm 0.95Hz$ and APP/PS1 $1.88 \pm 0.63Hz$, $p = 0.00939$). Since WT cells have larger sizes than APP/PS1 cells (due to the lack of dendritic degeneration), the differences in morphological structure and dendritic length between those groups could be an explanation. This is in agreement with previous studies showing elevated burst firing for larger cells (van Elburg and van Ooyen, 2010). Accordingly, a smaller dendritic size would reduce synaptically driven burst firing suggesting that dendritic degeneration may serve as a compensatory mechanism (Mittag *et al.*, 2023).

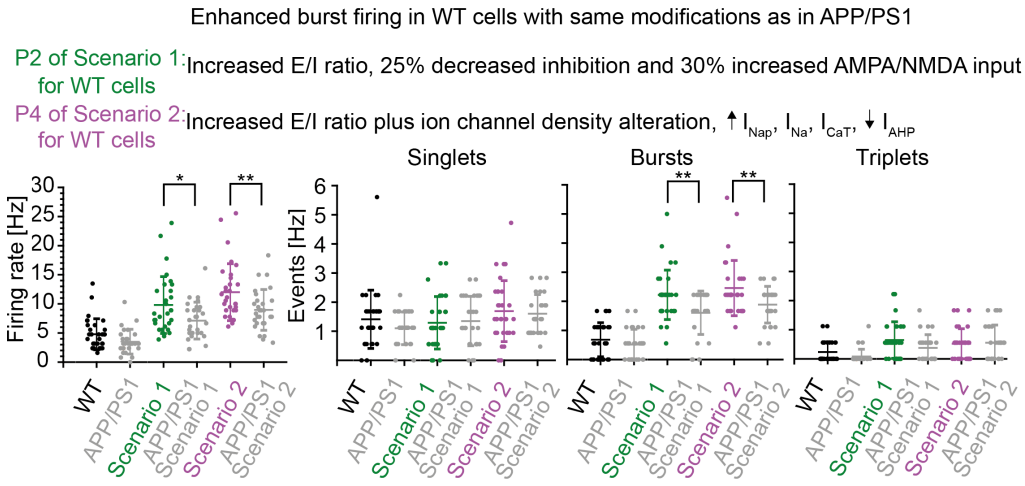

Figure 23. WT morphologies show a greater transition from single to burst firing than APP/PS1 PCs for extrinsic (network) and intrinsic (ion channel) modifications

Reproduced Figure 5 from "Modelling the contributions to hyperexcitability in a mouse model of Alzheimer's disease" (doi: https://doi.org/10.1113/JP283401) by Mittag M, Mediavilla L, Remy S, Cuntz H, Jedlicka P and licensed under CC BY 4.0 (Copyright Mittag *et al.*, 2023, http://creativecommons.org/licenses/by/4.0/): Overall firing rate, single APs, bursts ($> 1AP$) and triplets for original WT PCs (*black*), Scenario 1 for WT PCs (*green*, extrinsic changes) and Scenario 2 for WT PCs (*purple*, extrinsic/intrinsic changes). The original APP/PS1 PCs and the modified APP/PS1 PCs of Scenario 1 and 2 are shown in *grey*. The asterisks indicate that the modified WT PCs of Scenario 1 ($p = 0.0164$) and Scenario 2 ($p = 0.00871$) show a greater increase in overall firing rate than the respective modified APP/PS1 PCs. Concomitantly, for burst firing, the asterisks indicate that the modified WT PCs of Scenario 1 ($p = 0.00469$) and Scenario 2 ($p = 0.00939$) show a greater increase in burst rate than the respective modified APP/PS1 PCs.

In summary, the results for E/I imbalance and network and ion channel changes, separately and in combination (**Figure 20** and **21**), lead to the conclusion that the mode transition from solitary to burst firing that has been observed in APP/PS1 CA1 pyramidal neurons (Šišková *et al.*, 2014) can be explained by changes in E/I balance (Scenario 1), joint changes in E/I balance and ion channels (Scenario 2), or modified input network dynamics (Scenario 3), see Mittag *et al.* (2023). The role and interplay of intrinsic and extrinsic mechanisms in pathological AD hyperexcitability as an example of impaired IO function is more understood now. But what about the implications of these mechanisms regarding optimal IO function? This is investigated for the specific example of GC pattern separation under energy constraints in the next chapter.

5.4 Chapter 3: GC economy and pattern separation

The third chapter of this dissertation focused on the specific IO relationship of the GCs as a prominent hippocampal function, concentrating on biophysical modelling and optimisation. The main function of the GCs of the DG is their ability to perform pattern separation. They convert similar synaptic input into less similar somatic output on the single cell level as well as separating network input within GC circuits (Leutgeb *et al.*, 2007; Bakker *et al.*, 2008; Neunuebel and Knierim, 2014; Yassa and Stark, 2011; Chavlis and Poirazi, 2017). At the same time, biological functions are costly with respect to metabolic demands while their resources are limited. The cell therefore has to perform its function under energy constraints (Attwell and Laughlin, 2001; Harris *et al.*, 2012). Here, I investigated if and how the GC is optimized for the simultaneous performance of its pattern separation function in the form of relative redundancy reduction (**Equation 25**) and economy in the form of energy efficiency (negative ATP count: **Equation 41**) via the Pareto perspective. To answer this research question, the default GC model (Beining *et al.*, 2017) was compared to a population of GC models (Schneider *et al.*, 2023) whose ion channels were randomly modified and whose somatic behaviour had been previously inspected. The electrophysiological features of the somatic APs in all population models were similar to the experimentally validated (original) GC model ($Fitness < 2$). This means the models showed degeneracy with respect to their ion channel composition as many different compositions led to the same somatic output. Further constraints and functions, such as economy and pattern separation, could potentially separate the degenerate population models. The Pareto perspective helped to identify those models within the population that could be considered optimal due to their location on the Pareto front. Astonishingly, the original GC model was on the Pareto front and therefore seems to be Pareto optimal. A possible explanation for high performance was investigated with respect to the underlying sodium and potassium currents. The results revealed that a small temporal overlap of these currents was beneficial. As a test for the robustness of the results, input and channel noise were added which influenced the GC performance and the Pareto front. Finally, the important process of neurogenesis was included in the pattern separation evaluation (Kempermann *et al.*, 2004; Johnston *et al.*, 2016).

5.4.1 The original GC model lies on the Pareto front for simultaneous optimisation of economy and pattern separation

For the simulation of the information flow in GCs, known inputs to the GCs of the DG coming from the perforant pathway were investigated (*theta* and *beta* input between $5Hz$ and $20Hz$, Quintanilla *et al.*, 2022). Here, phase-locked spike ensembles with three component trains (i.e. three patterns, Bird *et al.*, 2024) were fed to the key input synapses of the GC outer molecular layer consisting of a spiking rate of $10Hz$ and $20Hz$, a correlation strength of 0.7 and a phase rate of $6Hz$ (schematic in **Figure 24 A**). When comparing the synaptic input with the somatic output to measure the performance, the original GC model (Beining *et al.*, 2017) was found to be on the Pareto front for the simultaneous maximisation of pattern separation and economy (*triangles* in **Figure 24 B**, *top*) compared to all other valid GC models (*dots*, $Fitness < 2$, see **Methods**) in a random population of GC models (Schneider *et al.*, 2023). Thereby, the original GC model neither showed the highest economy nor the highest pattern separation performance on its own but for both tasks together it was among the best performing models shown by its location on the Pareto front. It was Pareto optimal. This was true for the comparison with all valid 15 channel models as well as for the reduced model with only 9 channel models (**Figure 24 B**, *bottom*) and for the information transmission measure in form of the MI.

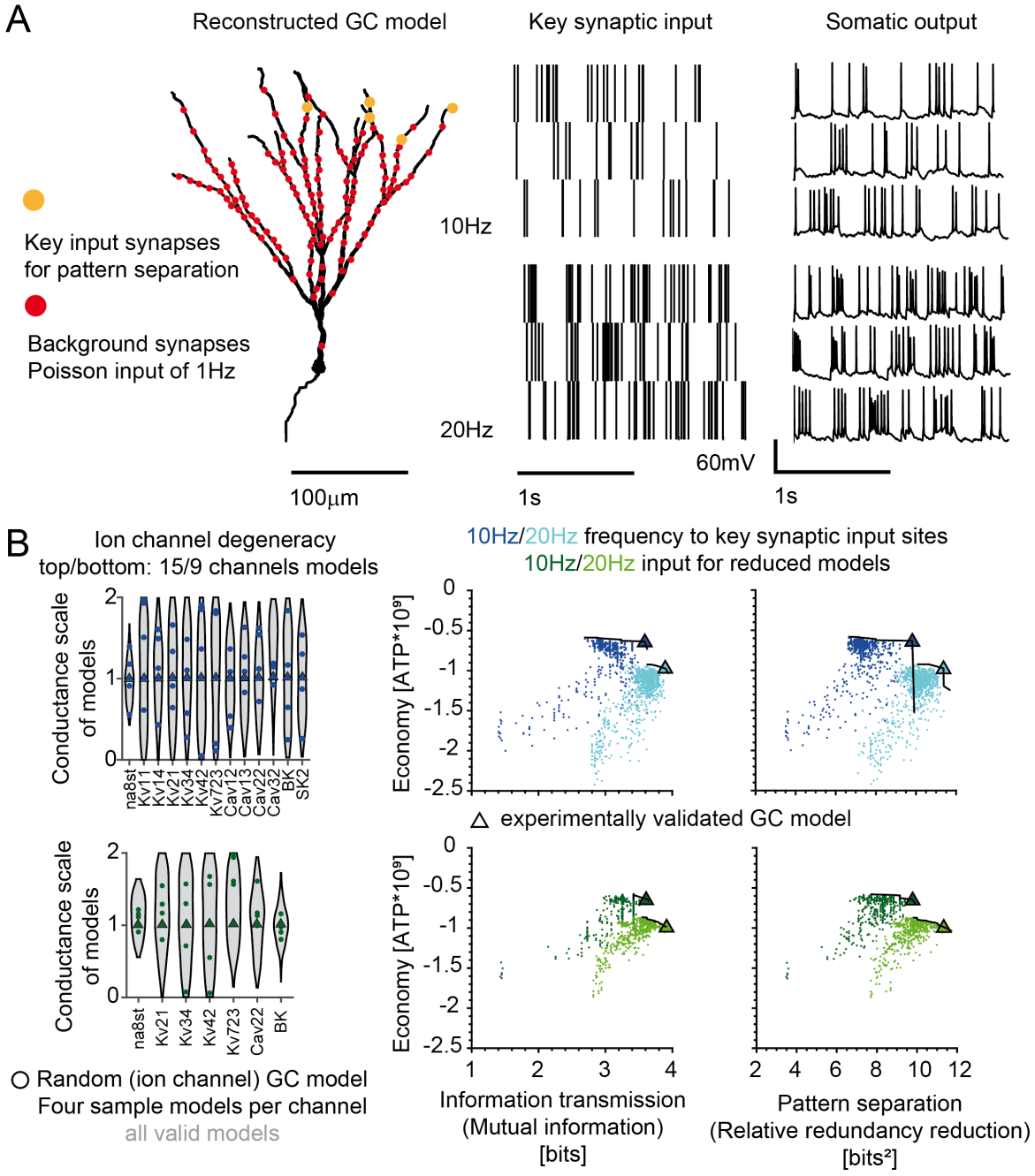

Figure 24. Simultaneous optimisation of economy and pattern separation for a population of valid GC models

A, GC morphology with key input synapses for pattern separation (*left, orange*), input spike ensemble for two frequencies ($10Hz$ and $20Hz$, *middle*, Bird *et al.*, 2024) and corresponding somatic output traces (*right*). **B**, *Left:* Ion channel composition and degeneracy for valid 15 and 9 channel models (*blue* and *green* respectively, adapted from Schneider *et al.*, 2023). *Right:* Information transmission and pattern separation versus economy shown for populations of valid GC models. The *black* line denotes the Pareto front and the *triangle* the original GC model (experimentally validated by Beining *et al.*, 2017).

5.4.2 How is the GC model performing so well? The underlying sodium and potassium currents show small overlap

Previous experiments and computer simulations have shown a link between optimal energy use and the overlap of sodium (influx of Na^+) and potassium (outflux of K^+) currents in the case of AP generation and transfer in mossy fibers (Alle *et al.*, 2009) and other cells (Crotty and Levy, 2007; Stemmler *et al.*, 2011; Niven, 2016). Interestingly, measures such as AP height or width seem to be poor predictors of the energy use (Sengupta *et al.*, 2010). It was therefore of interest to investigate if low usage of ATP could be explained by the overlap of the currents (example schematic in **Figure 25 A**) and further be a possible explanation for the optimised performance of the original GC model. First, a link between the GC model channels and the GC performances was established (**Figure 25 B**). Several correlations were revealed: Economy (negative ATP count), pattern separation (relative redundancy reduction) and efficiency (pattern separation/ATP) correlated positively with the axon hillock *Kv723* channel and most strongly with the dendritic *Kv42* channel. A negative correlation was seen for the axon hillock sodium *na8st* and the potassium *Kv14* channels. For the current overlap the same channel correlations could be seen but with reverse sign (except for sodium). Interestingly, an additional negative correlation of the current overlap with respect to the somatic *Kv21* and a positive correlation with the somatic *na8st* channel conductances could be observed (**Figure 25 B**). Importantly, this was not seen for economy, pattern separation nor efficiency. Second, the current overlap was directly compared to the performances. When comparing the overlap of somatic Na^+ and K^+ currents for the whole population of valid GC models, a negative correlation of the overlap with respect to economy, pattern separation and overall efficiency could be seen as shown in **Figure 25 C**. Especially the result for the relative redundancy reduction was interesting and its negative correlation to the current overlap is not obviously understood. The original GC model thereby had the smallest currents' overlap (see *triangles*). The points of the Pareto front (*10Hz: pink, 20Hz: purple*) are distributed among the whole data cloud, i.e. in a range between small and high current overlap. In all panels the correlation values for both input frequencies (r1 and r2) are indicated.

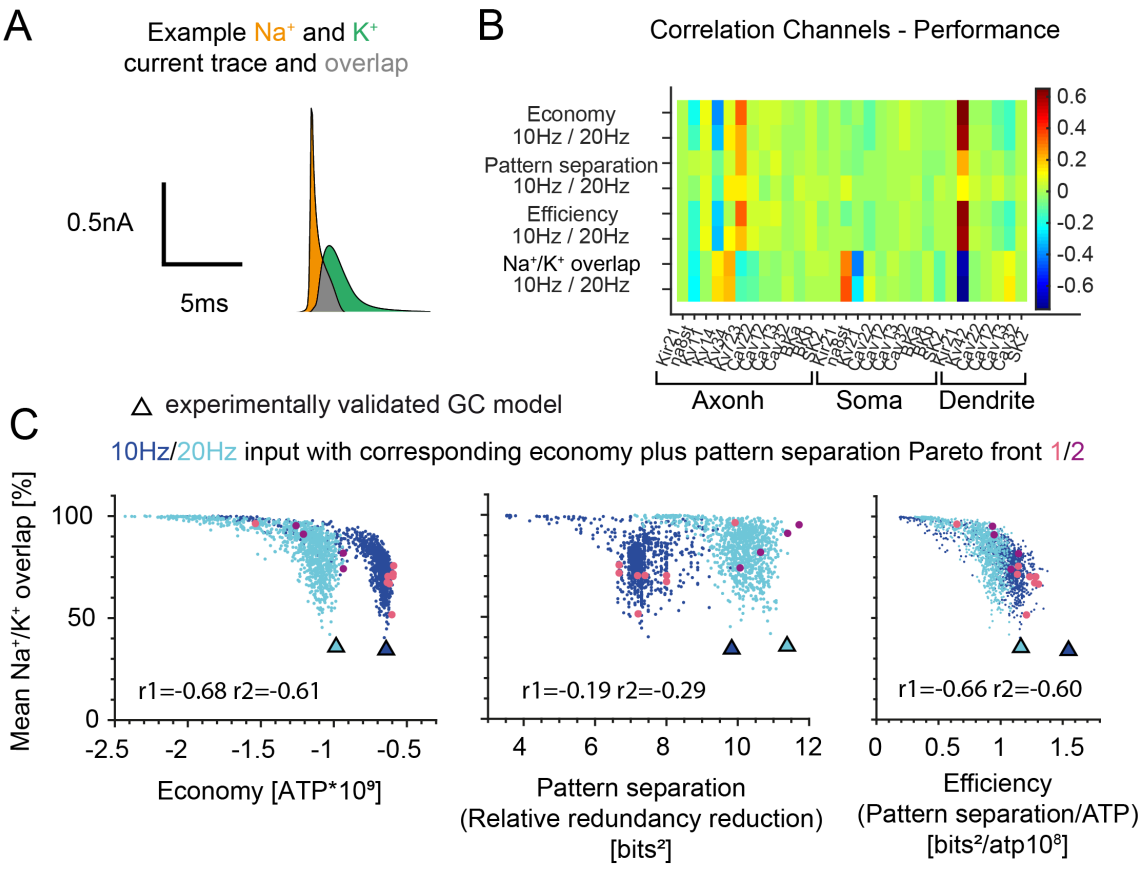

Figure 25. Sodium and potassium current overlap as a possible explanation for the optimal GC performance correlating negatively with economy and pattern separation

A: Example of current overlap for Na^+ and K^+ (sodium influx mirrored; overlap in *grey*). **B**: Correlation of channel conductances (13 out of the 15 model channels in the three cell regions were modified; the *HCN* channel and the passive conductance were not modified in Schneider *et al.*, 2023) with respect to the performance of pattern separation, economy (negative ATP) and efficiency (relative redundancy reduction divided by ATP) as well as the current overlap for both input frequencies. **C**: Mean Na^+ and K^+ overlap vs. economy, pattern separation and efficiency is shown. Correlation values are indicated in the panels. The *triangle* denotes the original GC model by Beining *et al.* (2017).

5.4.3 The original GC model shows high efficiency but only average robustness for the two-task optimisation of pattern separation and economy

Next, the robustness of the results was tested by introducing noise to the input (25% and 50% random input spike loss, schematic in **Figure 26 A**) as well as to the channel conductances ($\pm 5\%$ and $\pm 20\%$ additional conductance, **Figure 26 B**). The random loss of input spikes (*brown* and *orange* group) led to less ATP use compared to the no-noise condition (**Figure 26 C**, *left*). The shift to the left of the probability density functions (PDFs) confirmed the lower ATP use during input loss. This is not surprising as less synaptic input means less synaptic energy and lower somatic firing rate (reduced energy from the action potentials). In both noise groups the original GC model was at the low end of ATP use overall, however, more models showed even less ATP use than in the no-noise condition (see *triangles*).
Regarding the pattern separation function under noise in the form of relative redundancy reduction the original GC model performed at the upper end compared to the population of valid models in most conditions (**Figure 26 C**, *right*). Only in the $10Hz$ condition during input spike loss the performance went down to the population average (*brown* group). The loss of input spikes did not have such a strong effect in the $20Hz$ input condition compared to $10Hz$ since the cell received more (absolute number) input spikes overall and therefore the pattern was not as easily destroyed by missing spikes. The population of models as a whole showed a smaller maximum of the pattern separation performance and smaller variance for both noise conditions with $10Hz$ input (*brown* and *purple*). The PDFs of the $20Hz$ conditions for ATP and pattern separation measure were shifted to the right compared to the $10Hz$ conditions. More input therefore led to more ATP use but also better pattern separation.

Robustness of function after ion channel perturbation has been measured in previous studies by counting the fraction of perturbed models that still perform as the unperturbed model (Zang and Marder, 2023). In the investigations in this chapter, two functions are considered simultaneously: economy and pattern separation. Therefore these functions were combined into one efficiency measure defined as Pattern separation divided by ATP use. This is similar to commonly defined metabolic efficiency of MI/energy (Stone, 2018).

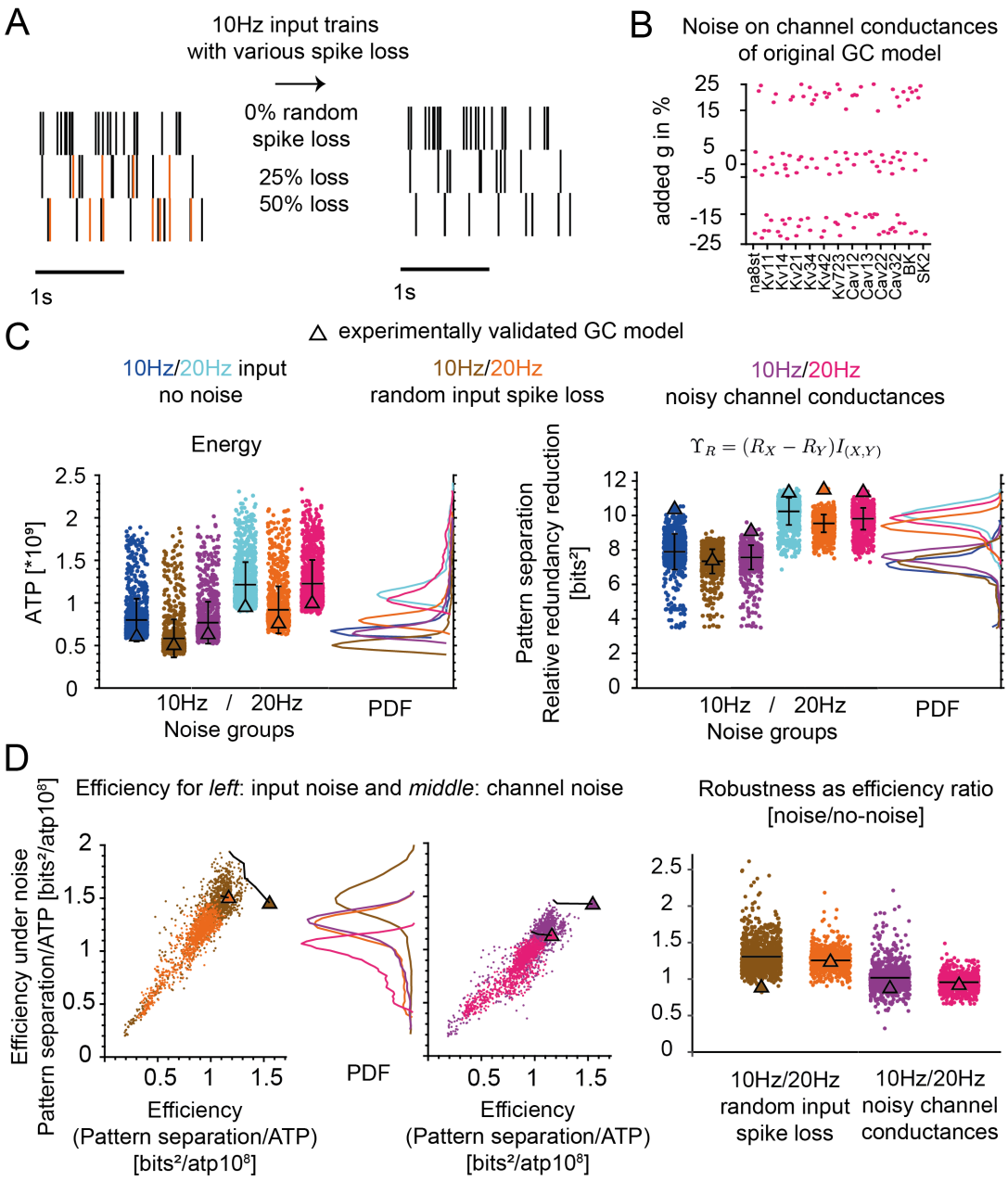

Figure 26. Efficiency and robustness to noise (intrinsic and extrinsic) of GC models regarding their concurrent pattern separation performance and economy

A: Schematic of input spike loss (input noise) for several spike trains and degrees of spike loss shown. **B**: Noise added to the channel conductances ($\pm 5\%$ and ± 15 to $\pm 25\%$) for the original GC model. **C**: Energy and relative redundancy reduction for all noise groups shown (*Blue/cyan*: no noise, *brown/orange*: input noise, *purple/pink*: channel noise). **D**: Efficiency vs. efficiency under noise and robustness (ratio of efficiency during noise divided by no-noise) shown for all noise conditions. The *black* line denotes the Pareto front and the *triangle* the original GC model by Beining *et al.* (2017).

The efficiency analysis revealed that in both noise conditions (input noise: **Figure 26 D**, *left*; and channel noise: **Figure 26 D**, *middle*), the original GC model performed better without noise than with noise as it was located on the right side of the Pareto front (see *triangles*). This was true for the $10Hz$ and the $20Hz$ condition. The slope of the population data in the input noise condition was higher than in the channel noise condition and the PDFs were shifted to the right due to the lower ATP use associated with input spike loss leading to higher efficiency (compare **Figure 26 D**, *left* and *middle*). Instead of counting the fraction of perturbed models performing to one specific, collective value (Zang and Marder, 2023), the robustness measure here compared the performance of each individual model with and without perturbation to itself. It was defined as efficiency during the noisy conditions divided by the efficiency of the no-noise condition. Consequently, a value smaller than 1 showed impaired performance. The robustness analysis of the efficiency performances confirmed that the effect of noise was stronger in the $10Hz$ condition: the original GC model was below population average when compared to other valid models for the robustness ratio (**Figure 26 D**, *right*). At the same time the robustness value of the original GC model was smaller than 1 in most conditions showing impaired performance under noise. Regarding the population average the robustness measure was bigger than 1 for input noise, confirming the higher efficiency under noise, and around 1 for channel noise, showing that some models improve and others impair the efficiency performance while the average stays robust.

For all conditions of the performances, the data showed skewed distributions (see PDFs in **Figure 26** C and D). The ATP measure was positively skewed with a long right tail which meant most models in the population had a low use of energy, or conversely the economy was high and negatively skewed. The pattern separation measure, however, was more symmetric and resembled a normal distribution. Together, the efficiency measure of pattern separation divided by ATP resulted in a negatively skewed distribution with a long left tail. Most population models therefore showed high efficiency.

Finally, in all investigated situations here the original GC model was on the Pareto front showing high efficiency but only average or below average robustness to noise for simultaneous optimisation of pattern separation performance and economy of energy.

5.4.4 Is the Pareto front the actual front? Perturbations and constraints can influence the Pareto front location

The robustness analysis earlier (**Figure 26**) revealed that the experimentally validated GC model performed better when there was no perturbation compared to the conditions of extrinsic (input loss) or intrinsic (channel) noise. Though, in most cases the performance was still among the best compared to the population of random GC models. Since two tasks were considered simultaneously, it was beneficial to analyse the results from the Pareto perspective. Therefore, the actual Pareto front for each of these noisy conditions was analysed in more detail, specifically with focus on the stability of its location. Overall, the Pareto front as well as the performances of the original GC model were not fixed and moved slightly for noisy conditions (**Figure 27 A**). In more detail, input spike loss moved the Pareto front towards lower energy (higher economy) and eventually with high noise (75%, *red*) towards lower pattern separation performance (**Figure 27 A**, *left*). This is understandable since less input spikes means less synaptic energy and less somatic firing. The $10Hz$ condition was more sensitive to input loss than the $20Hz$ condition shown by the movement of the Pareto front towards lower pattern separation performance already for medium noise (50%, *orange*). For channel noise the Pareto front stayed similar for random conductance variations up to 20% (*yellow* and *orange*) but high noise (50%, *red*) led to lower energy and lower pattern separation performance (**Figure 27 A** *right*). In all cases the original GC model was surprisingly close to the Pareto front (see *triangles*).

A further analysis of the Pareto front of the two-task optimisation problem for pattern separation and economy was performed by comparing the GC model (all valid models in *grey*, original GC model with *blue triangles*) with a toy model, namely the leaky integrate fire model (LIF, **Figure 27 B**, *blue dots*). The LIF model did not include channels but the morphology was taken into account (see **Methods**). In the LIF model, a somatic AP was generated once a certain voltage threshold had passed; this was followed with a reset of the voltage to its baseline. Additionally, the active GC model was compared with the non-spiking GC model (passive and blocked *na8st* channel). As a result, the LIF Pareto front was similar to the GC model Pareto front but with a shift to a higher maximum for the pattern separation performance and higher energies even though only synaptic energy was counted since the LIF model did not contain channels that could contribute to the ATP count. The passive and blocked GC models did not perform any pattern separation due to having no somatic output spikes. Consequently

they had a lower energy count and higher economy. They could be considered archetypes of the GC model Pareto front for the economy dimension.

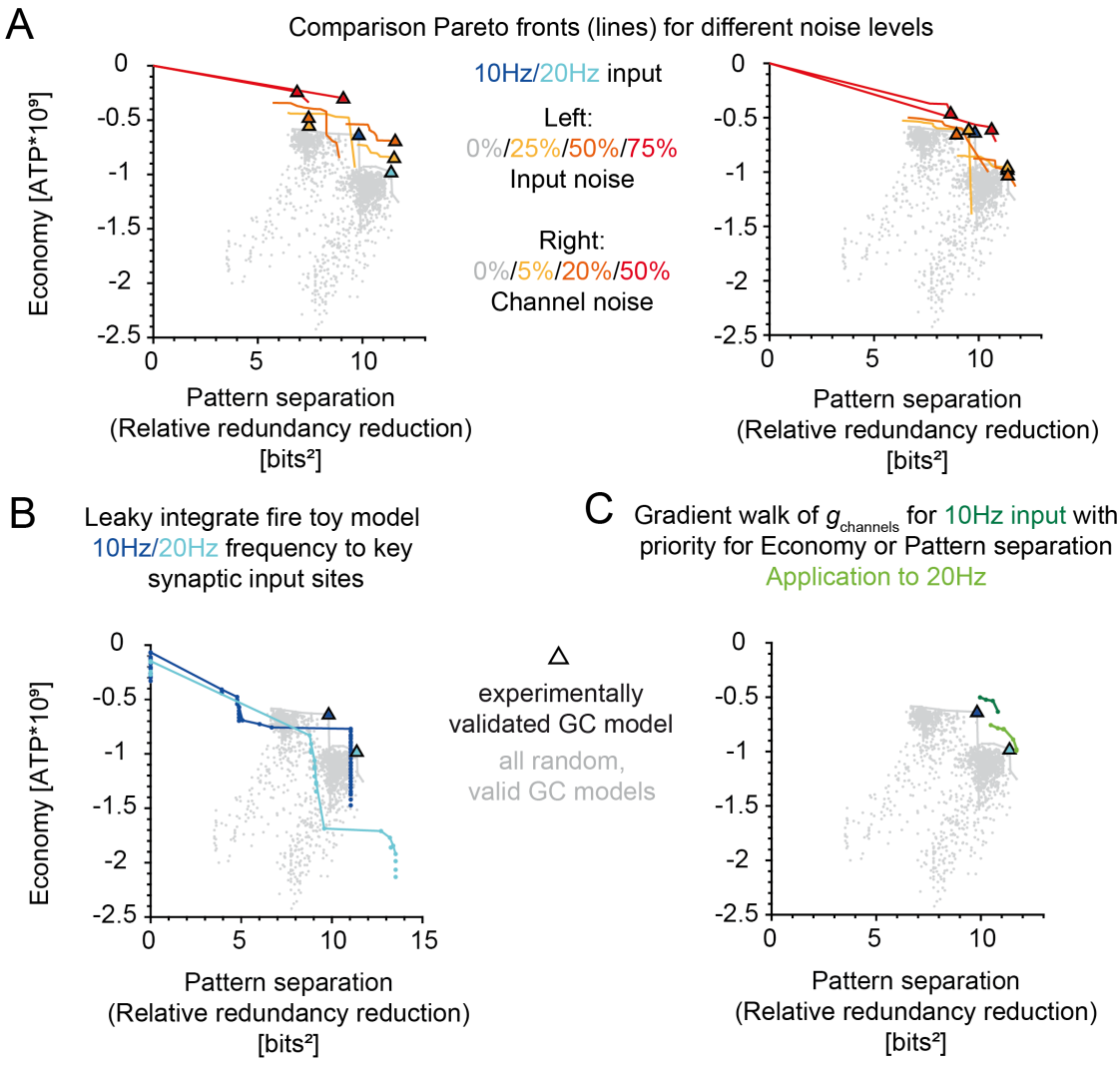

Figure 27. Stability of the Pareto front of the GC two-task optimisation during random noise and its comparison to a LIF model and a general parameter search

A: The Pareto fronts for simultaneous optimisation of pattern separation and economy shown for various degrees of input noise (*left*) and channel noise (*right*) as applied in **Figure 26**. The *grey* dots show all the random valid GC models from **Figure 24**. The upwards *triangle* denotes the original GC model by Beining *et al.* (2017). **B**: Leaky integrate fire (LIF) models and their economy versus pattern separation performance shown for input frequencies of $10Hz$ and $20Hz$ (*blue* and *cyan*). **C**: An optimisation algorithm was applied to the channel conductances of the original GC model (*triangle*) to improve performance in the $10Hz$ input condition with priority to economy or pattern separation (*dark green*). The application of the found mechanisms to the $20Hz$ input condition is depicted in *light green*.

Could the Pareto front, that was constructed by the performance of all random and valid GC models, be improved, i.e. moving its location towards higher pattern separation and economy? An optimisation algorithm was implemented that incrementally changed the conductances of 27 channels and regions ($\pm 5\%$ steps) of the original GC model (*triangle*). The goal was to concurrently improve economy and pattern separation in the $10Hz$ input condition without the original $Fitness$ constraint. In case this was not possible the priority of the algorithm was for simulation one to improve economy and for simulation two to improve the relative redundancy reduction (**Figure 27 C**, simulation one with 23 solutions and simulation two with three solutions of the optimisation walk respectively, totaling 26 solutions for both with a Pareto front in *dark green*). Indeed, the algorithm found channel parameters for which higher pattern separation or economy was possible: 24 of the 26 solutions showed lower ATP use, 23 higher relative redundancy reduction performance, and 21 improved in both simultaneously when compared to the performance of the original GC model. The channel mechanisms found by the optimisation algorithm were then applied to the $20Hz$ input condition as a control and generalisation test of the solutions (in *light green*). In that case, again 24 solutions showed lower ATP use, but only three improved in relative redundancy reduction performance, and only one in both at the same time (meaning 100%, 13%, and 5% compared to the number of solutions in the $10Hz$ condition respectively). It is important to note, that the $Fitness$ of the newly found GC models and their altered mechanisms with regards to somatic features was not a constraint of the search algorithm. This is in contrast to the population of GC models (*grey*) which were chosen to be valid due to having a $Fitness < 2$ and therefore being similar to experimental data and the original GC model by Beining *et al.* (2017), see Schneider *et al.* (2023). Likely, a longer and more detailed parameter search (see **Methods**) might have found even better results for the performances.

In summary, the perturbations due to input or channel noise did not disturb the Pareto front much when the noise was moderate. For high noise the Pareto front moved first to lower energies and then to lower pattern separation performance. Interestingly, compared to a model without ion channels (LIF) the GC models established a Pareto front with higher economy but smaller maximum pattern separation. Without the somatic behavioural constraint of the population models a parameter search could find ion channels that resulted in slightly better performances beyond the original Pareto front.

5.4.5 Young GCs simultaneously optimise for the pattern separation performance and economy with tendency towards low energy

Young abGCs can contribute to pattern separation and play a role in memory formation in the hippocampus (Clelland *et al.*, 2009; Johnston *et al.*, 2016). Therefore, in this section of the GC investigation the mature cells (*blue*) were compared to newly formed cells (*red*, see schematic in **Figure 28 A**). In order to do that, the original GC model (Beining *et al.*, 2017) was implemented in a whole dataset of 23 GC reconstructions (Schmidt-Hieber *et al.*, 2007; Vuksic *et al.*, 2011). Importantly, all cells per cell group had the same ion channel expressions and only differed in morphology. The mGC group was distinguished from the abGC group by using the same morphologies but with decreased synaptic density (40%, see also schematic in **Figure 28 A**) and blocked channels (Kir, Kv, BK channels according to Mongiat *et al.*, 2009; Beining *et al.*, 2017). For different pattern separation measures (relative redundancy reduction in **Figure 28 B** *left*, and sparsity weighted MI in **Figure 28 B** *middle*) the abGCs were located on the Pareto front with a tendency towards higher economy. They also showed higher efficiency (relative redundancy reduction per ATP use in **Figure 28 B** *right*) compared to the mGCs ($10Hz$: $p = 0.023$, $20Hz$: $p = 0.009$). Overall the abGCs simultaneously optimised the performances of pattern separation and economy leaning towards lower energy use than mGCs. This was mainly due to the lower synaptic density in abGCs and therefore less synaptic energy. At the same time the change in ion channel composition increased the excitability of abGCs but did not lead to higher energy use by the channels. It rather led to similar somatic firing rates and similar pattern separation measures even with less input. Both, mGCs and abGCs, showed a negative correlation of cell path length with respect to economy (negative ATP count), pattern separation and efficiency (**Figure 28 C**), i.e. a small cell showed higher economy since it has a smaller amount of channels and synapses that could contribute to the ATP count compared to a big cell. At the same time also the pattern separation (relative redundancy reduction) performance preferred a smaller cell. This led to an overall high anti-correlation between cell length and performance efficiency as it is defined by pattern separation over ATP use. The abGCs displayed even higher anti-correlation than the mGCs for most cases. The correlation values for both input frequencies (r1 and r2) are indicated in the respective panels.

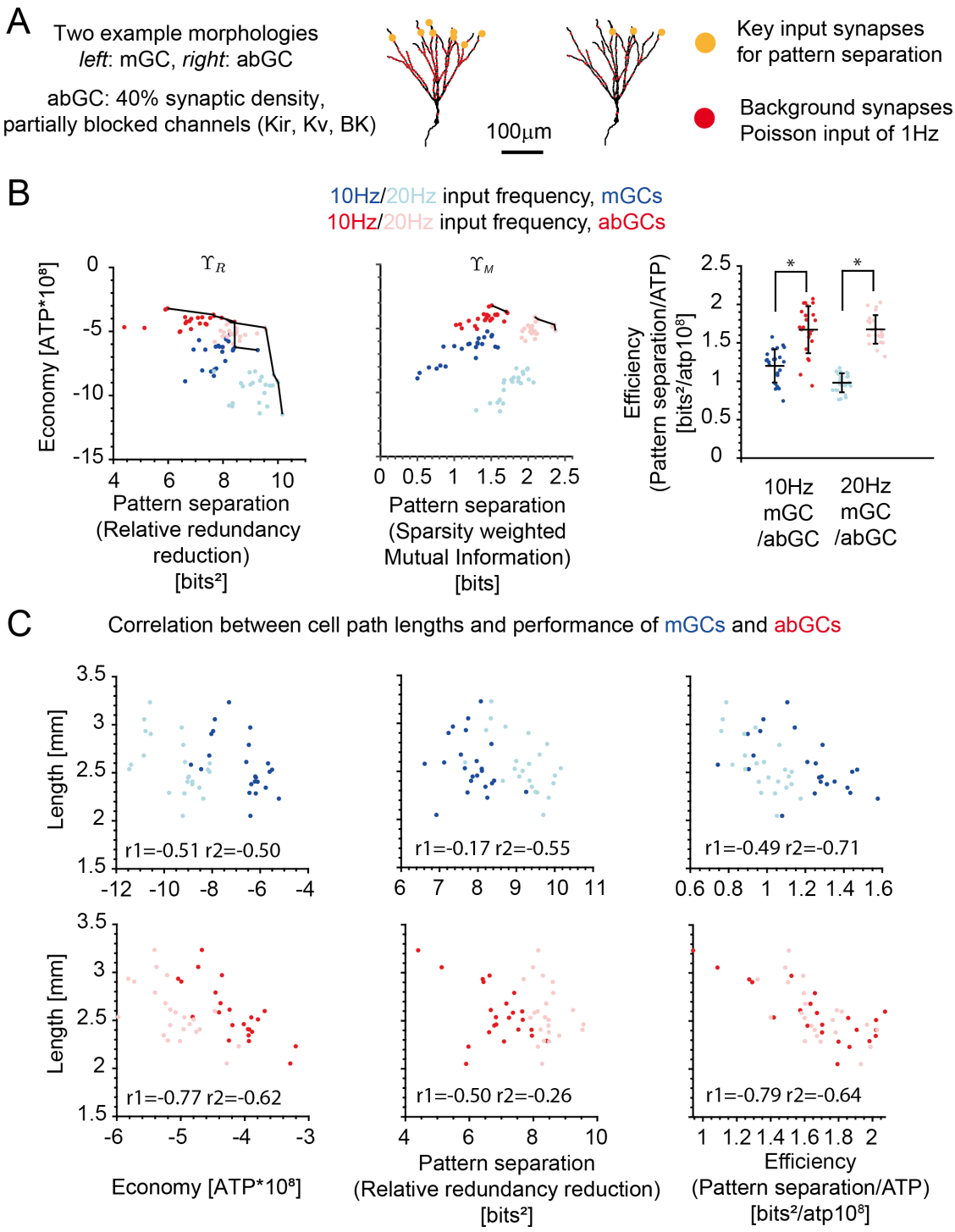

Figure 28. Comparison of mGCs and abGCs regarding simultaneous optimisation of pattern separation and economy and their dependence on cell length

A: Example morphologies for mGCs and abGCs. **B**: Economy vs. pattern separation (relative redundancy reduction, *left*, and sparsity weighted MI, *middle*) shown for mGCs (*blue*) and abGCs (*red*). The $20Hz$ condition is shown by the light colors. *Right*: Efficiency (pattern separation over ATP use) shown for both cell groups and input frequencies. **C**: Path length vs. economy, relative redundancy reduction and efficiency shown for mGCs (*top, blue*) and abGCs (*bottom, red*) with the correlation values indicated in the panels.

6 Discussion

The aim of this dissertation was to investigate rodent hippocampal nerve cells via realistic *in silico* models with respect to their morphology, intrinsic mechanisms and IO function. Thereby, several physiological and pathological conditions were compared in three major, complementary investigations covering invariant, impaired and optimised IO function. In the first chapter of this dissertation, a general principle of invariant IO function was revealed, called "dendritic constancy". It was confirmed as a fundamental, activity-equalising principle for several cell models independent of size and complexity during synaptic activation. Importantly, the cell models included realistic, dynamical non-linearities such as NMDA synapses and especially voltage-dependent ion channels. The dendritic constancy principle held true under all conditions. Furthermore, the dendritic constancy principle aided in the investigation of dendritic structural changes and the concurrent pathological hyperexcitability prevalent in AD PCs in the second chapter of this dissertation. Three possible scenarios for hyperexcitability as a form of impaired IO function could be identified that most likely cause the observed enhanced bursting in AD. The hyperexcitability scenarios were independent of the morphological changes but included modifications of intrinsic (ion channels) and extrinsic (E/I ratio) mechanisms during AD. The ion channel mechanisms played a further role in the third and final investigation of the thesis concerning optimised GC IO function. Chapter three established the original GC model, which had been validated by literature and experiments, as one of the optimal models located on the Pareto front in a population of valid GCs for the simultaneous performance of the pattern separation IO function and economy. This was supported by the fundamental finding that low energy usage and high pattern separation performance correlated with low current overlap of sodium and potassium. This is due to the particular ion channel expressions ultimately affecting the IO function. Finally, young abGCs were located on the Pareto front as well with tendency to low energies revealing the important role young GCs could play in pattern separation and in general in memory formation in the hippocampus. In summary, all *in silico* investigations in this dissertation revealed a close relationship between morphology, intrinsic ion channel mechanisms and IO function of hippocampal neurons.

6.1 Range of application and limitations of dendritic constancy

In the first chapter of this thesis, three compartmental models were implemented (Poirazi *et al.*, 2003a; Jarsky *et al.*, 2005; Almog and Korngreen, 2014) describing the underlying biophysics of rat PCs. They included several voltage-dependent ion channels and therefore made the cell models more realistic. For all models and reconstructions ($n = 105$ hippocampal CA1 PCs and $n = 20$ cortical layer 5 PCs) the IO function was invariant under synaptic activation continuously showing an independence of the activity from the cell size. This is a confirmation of the dendritic constancy principle previously shown for passive dendrites (Cuntz *et al.*, 2021). Furthermore, adding the synaptic transmission for excitatory NMDA and inhibitory GABA receptors, which contribute to the non-linear dynamics of the synaptic input signal, expanded the working range of the dendritic constancy principle further. This was true for whole cell and clustered synaptic activation. Importantly, each step of this investigation (from **Figures 13 - 15**) incorporated more accurate biophysics to the model neurons as shown in literature. Thereby, the results from this dissertation were key in validating the dendritic constancy principle by expanding it from theoretical considerations (**Equation 11**) and passive models (**Figure 2**) to realistic, active neuron models for synaptic activation (Cuntz *et al.*, 2021).

There are several assumptions involved in the derivation of the analytic solution of the dendritic constancy rule for neurons, that have consequences for the applicability and limitations of it as a general principle (Cuntz *et al.*, 2021). They mainly relate to morphological and electrophysiological features of the cells. The **Equations 10** and **11** show that, even though there is no length dependence, the voltage change still depends on the specific membrane conductance, the synaptic conductance and the average dendritic diameter. But it also depends on the axial conductance and the somatic leak conductance. First, the membrane conductance can vary greatly between individual neurons even from the same cell type which has been shown in previous studies: Garden *et al.* (2008) showed that the best approximation of data, especially for input resistance, was achieved with a non-uniform distribution of the membrane conductance within the cell; and Grashow *et al.* (2010) showed that the membrane conductance of a cell could vary between two- and eight-fold for different cell types. However, the average membrane conductance was comparable again between the cell types. Second, the average dendritic diameter was normalised for all cell reconstructions in this thesis. But real diameters can vary as can be seen in **Figure 14 C** for the PC data set used here. For an individual neuron this means, in consequence of **Equation 11**, that also the voltage response can vary. On a

population level, however, these differences matter less as they affect small and big cells alike and there is no length dependency. The variance in voltage response and firing rate gets bigger with bigger variance in dendritic diameter but the average response is still well approximated by **Equation 11** using the average dendritic diameter of all cells (**Figure 14 C**). Third, the somatas in this thesis did not have synapses located on their surface bodies as only the dendrites received synaptic input. This means that there was an empty "cable" surface that constituted a leak and potentially influenced the neural activity since one of the requirements of the dendritic constancy equation derivation was to give synaptic inputs along the whole cell surface area. According to Cuntz *et al.* (2021) the somatic leak effect can be minimised by small somatic conductances or by including the somatic diameter in the overall diameter normalisation of the cells. Fourth, synaptic conductances are not constant within a cell. They were modeled to increase with soma distance for AMPA and to decrease for NMDA to ensure realistic synapse strength distributions and dendritic democracy (Häusser, 2001; Kim *et al.*, 2015). The dendritic constancy principle still held true with these non-homogeneous synapse strengths. Interestingly, in potential numerical experiments, the synaptic conductances can in fact be used to approximate a certain desired output voltage change or subsequent firing rate: given **Equation 11** for certain values of the dendritic diameter and membrane conductance, the synaptic conductances can be set in a way to reach the desired somatic voltage response (Cuntz *et al.*, 2021). For the example of non-normalized dendrite diameters, the synaptic conductances could be scaled with the average diameter of the corresponding dendrite to control the voltage response and get the analytically predicted response as for the normalized diameter (Cuntz *et al.*, 2021). In a further step, knowing the synaptic conductances then can be used to approximate the synaptic input activation necessary for the desired voltage response. In addition to the synaptic conductances, the entire synaptic kinetics can potentially vary between synapses including the equilibrium potential which would certainly influence the voltage response and firing behaviour to synaptic input.

In combination, several variations of different parameters or mechanisms at the same time could possibly be able to cancel each other; e.g. different somatic leaks or different dendritic loads due to different morphologies might be canceled by concurrent variation of the AIS (location plasticity, Jamann *et al.*, 2021; Kumar *et al.*, 2022) or by ion channel density changes within the soma or axon (Hay *et al.*, 2013; Zbili *et al.*, 2021) to still guarantee the same somatic firing behaviour in a homeostatic manner. AIS plasticity was not included in this dissertation and has to be further investigated. However, ion channel alterations were an essential intrinsic

modification in this thesis and are discussed later in detail.

Dendritic constancy has specific clinical implications since changes in cell size and structure occur within several neural pathologies such as AD (Spires and Hyman, 2004; Grutzendler *et al.*, 2007; Šišková *et al.*, 2014; Rao *et al.*, 2022), epilepsy (Theodore *et al.*, 1999; Aroor and Brewster, 2021), stress (Magarin *et al.*, 1995; Belleau *et al.*, 2019) and depression (Sheline *et al.*, 1996; Roddy *et al.*, 2019). In this dissertation, pathological morphological changes in nerve cells in the form of dendritic atrophy are discussed. AD-related dendritic structural degeneration of CA1 PCs is a prominent example (Braak *et al.*, 1993; Cochran *et al.*, 2014; Šišková *et al.*, 2014). Often, dendritic atrophy is considered a feature of the pathology (Fiala *et al.*, 2002; Šišková *et al.*, 2014; Halliday, 2017). But previous studies already proposed the degeneration to be a mechanism of the cells' homeostasis regulatory system (Vlachos *et al.*, 2012; Dell'Orco *et al.*, 2015; Lenz *et al.*, 2023). For example, for dendritic structural changes in denervated GCs of the DG the modelling studies of Platschek *et al.* (2016, 2017) showed that there was a balance between synapse loss and dendritic reduction which kept the synapse density equal and resulted in similar somatic responses for synaptic activation. Experimental results confirmed that the density of synapses in pathological cells after denervation indeed reached a level equal to the healthy cells before (Steward *et al.*, 1988; Vuksic *et al.*, 2011). Under these conditions, dendritic constancy is a general principle that can be applied to explain equal firing rate for cells of different sizes due to pathological dendritic changes (Cuntz *et al.*, 2021). Similarly, this dissertation demonstrates that concurrent with synapse loss the dendritic atrophy during AD can be a homeostatic mechanism to keep the cell function stable by increasing the input resistance and therefore excitability in order to counter the lower synaptic excitation (Mittag *et al.*, 2023). This is discussed in more detail for chapter two involving AD hyperexcitability.

The dendritic constancy principle is not the only rule involved in the processes and dynamics of the nerve cells. It is rather an underlying, activity-equalising principle whereupon other processes can act. In the dendrites, several linear and non-linear computations (London and Häusser, 2005; Payeur *et al.*, 2019; Bicknell and Häusser, 2021) and synaptic plasticity rules (Turrigiano and Nelson, 2004; Morrison *et al.*, 2008; Magee and Grienberger, 2020; Inglebert *et al.*, 2020) are known to exist and interact with each other. These processes can be local or global within the cell and add to the transformation of synaptic signals into somatic voltage or firing patterns in a complex way. In addition to dendritic spikes (a feature of the compartmental model by Poirazi *et al.*, 2003b, see **Figure 13 D**) there are further dendritic events possible in a

neuron, such as NMDA and calcium spikes (Golding *et al.*, 2002; Larkum *et al.*, 2007; Major *et al.*, 2013; Larkum *et al.*, 2022). They add further non-linearities to the dendritic computation. The inhibition employed in chapter one was distributed along the dendrites and relatively weak. It did not disrupt the dendritic constancy principle. However, strong inhibition is known to have an effect on neurons in the form of shunting. For instance, it has been observed that the inhibition causes the input resistance to drop locally in such a drastic manner that the resulting voltage response is decreased in a supra-linear way (Mitchell and Silver, 2003). In chapter two, strong somatic inhibition was applied to the CA1 PCs (high γ range of $50-100Hz$) in order to create burst activity. Remarkably, the dendritic constancy principle was still valid in that case.

It is important to note that the dendritic constancy principle only refers to the firing rates of cells, i.e. the number of spikes. The exact timing of the spikes can vary between cells even though they might show the same average firing rate. For example, Cuntz *et al.* (2021) showed different firing patterns (including bursts) between different cell types while displaying the same firing rate for all of them (see also Connors and Gutnick, 1990). Nevertheless, the specific spike pattern and variety in spike timing can be important for the cell and brain function (Shinomoto *et al.*, 2009; Gjorgjieva *et al.*, 2016; Denève *et al.*, 2017; Paton and Buonomano, 2018). Consequently, in the third chapter of this dissertation, special attention was given to the spike pattern. It was investigated with respect to the pattern separation performance of dentate GCs (Bakker *et al.*, 2008; Yassa and Stark, 2011; Rolls, 2013; Bird *et al.*, 2024). This will be discussed further for chapter three.

6.2 AD dependent dendritic changes and its relation to hyperexcitability

In the second chapter of this dissertation, the dendritic constancy principle was a helpful guide in the investigation of hyperexcitability in AD, an impaired IO function. Hyperexcitability, the phenomenon of increased firing rate, has been investigated in many AD studies covering different methods such as *in vivo* (Palop *et al.*, 2007; Busche *et al.*, 2008, 2012; Šišková *et al.*, 2014; Verret *et al.*, 2012; Busche and Konnerth, 2016; Palop and Mucke, 2016; Sosulina *et al.*, 2021), *in vitro* (Šišková *et al.*, 2014) and organoids experiments (Ghatak *et al.*, 2019). This includes computational studies (Šišková *et al.*, 2014; van Elburg and van Ooyen, 2010; Vitale *et al.*, 2021; Mittag *et al.*, 2023). However, the actual underlying mechanisms and causes are

not fully understood. At the same time, another characteristics of AD has been shown in previous studies: dendritic structural degeneration of the neurons (Braak and Braak, 1991; Braak *et al.*, 1993; Anderton *et al.*, 1998; Le *et al.*, 2001; Augustinack *et al.*, 2002; Tsai *et al.*, 2004; Grutzendler *et al.*, 2007; Merino-Serrais *et al.*, 2013). In fact, few studies suggested a link between the enhanced firing and the dendritic degeneration (Šišková *et al.*, 2014; Ghatak *et al.*, 2019). The reasoning behind it can be understood from the following physical considerations of the electrotonic mechanisms. Morphological changes in a neuron in the form of dendrite shrinking lead to a reduction in membrane surface and consequently membrane conductance. The cell's input resistance is increased and therefore also the voltage response, i.e. the cell is more excitable (Van Ooyen *et al.*, 2002; van Elburg and van Ooyen, 2010). Importantly, this holds true for somatic current injections as well as for synaptic activation if the absolute number of synapses is constant between a small and a large cell (Šišková *et al.*, 2014). In line with dendritic constancy, the dendritic atrophy can potentially be a homeostatic effect to maintain IO function when also synapse loss occurs at the same time. In that case, the dendritic shortening with its resulting increase in excitability may counteract the lower number of synapses and therefore lower synaptic excitation. Even though the absolute number of synapses is decreased in this situation, the relative synapse density is invariant (Šišková *et al.*, 2014) which is a requirement of dendritic constancy (Cuntz *et al.*, 2021). For another pathological case of dendritic atrophy in GCs after EC lesion the electrophysiological modeling study by Platschek *et al.* (2016) explored the relationship of synapse loss and morphological changes. It revealed that dendritic atrophy was capable of adjusting the excitability of neurons thus compensating for the denervation-evoked loss of synapses (Platschek *et al.*, 2016, 2017). The computational principle of dendritic constancy has been previously shown for various cell types with a variety of dendritic shapes and sizes for passive models in Cuntz *et al.* (2021). It was further generalised to a large data set of CA1 PCs for several active, biophysical models in the first chapter of this dissertation. In summary, the analytical derivation (Cuntz *et al.*, 2021) and numerical simulations (Cuntz *et al.*, 2021; Mittag *et al.*, 2023) have shown that neuronal excitation in response to distributed synaptic inputs was generally independent of the cell length for invariant synaptic density. As an application of dendritic constancy from chapter one, rigorous computational modelling in chapter two indicates that atrophied APP/PS1 cell morphologies do not lead on their own to increased firing and bursting as compared to the WT group (**Figure 16** and **Figure 18**, Mittag *et al.*, 2023). This is based on the same density of distributed synaptic inputs which is in line with data showing comparable

spine and synapse density in APP/PS1 and WT PCs (Šišková *et al.*, 2014). At a later stage of the disease progression (> 20 months) additional spine loss can occur resulting in lower synapse density (Spires-Jones *et al.*, 2007; Knobloch and Mansuy, 2008; Bittner *et al.*, 2010). In that case, the homeostatic effect of dendritic degeneration obeying the dendritic constancy principle might break down since further shrinking of the dendrites to keep the synapse density constant seems to reach a limit. In this thesis however, the activity-invariant effect of dendritic degeneration on excitability in AD model cells was persistently observed. It was valid for the simple synaptic models with AMPA synapses (**Figure 16**) as well as for more complex synaptic models with distributed AMPA, NMDA and GABA-A synapses (**Figure 18 B**). Additionally to changes in dendritic length in the APP/PS1 cell morphologies also other morphological measures such as the number of branch-points and the surface area of the cells were concomitantly altered. Likewise, these changes had no effect on the excitability (**Figure 16 C**). No hyperactivity was found in the APP/PS1 cells, which display dendritic degeneration, for any of the whole cell stimulations. A second compartmental model by Jarsky *et al.* (2005) was implemented to check for variability or robustness of the results regarding the underlying biophysical mechanisms in form of ion channels. It confirmed the results of the previous model by Poirazi *et al.* (2003b) similarly showing no hyperexcitability in APP/PS1 cells based on morphological changes alone (**Figure 17**).

Moreover, whole cell distributed synaptic activation is not the only input mode received by the cells. Three prominent input layers such as EC input to the tuft, and CA3 input to oblique and basal dendrites are known, which show a distinct behavioural input pattern (theta frequency $5Hz$) received by the hippocampus (Bannister and Larkman, 1995; Megías *et al.*, 2001; Ang *et al.*, 2005; Manns *et al.*, 2007; Takahashi and Magee, 2009; López-Madrona *et al.*, 2021). Since basal dendrites are generally lost before the more peripheral portions of the apical dendrites in AD-related CA1 PCs (Scheibel, 1979; Šišková *et al.*, 2014), layer specific inputs could potentially lead to different excitation. As a result, a link between dendritic degeneration and excitability change could be seen, which is a direct effect of specific pathway inputs on the cell's response for both morphology groups (**Figure 18**). On the one side, stimulation of basal dendrites resulted in decreased firing of APP/PS1 cells compared to WT cells (**Figure 18 C, D**, *Right panels*). On the other side, stimulation of apical dendrites increased the activity of APP/PS1 cells though it was only significant in the passive model (**Figure 18 C, D**, *Middle panels*). An explanation of this effect is that the decrease in basal/apical ratio in APP/PS1 cells due to stronger basal degeneration resulted in less stimulated area per whole

cell surface for activation of basal dendrites. Alternatively, the stimulated area per whole cell surface was increased for activation of apical dendrites (**Figure 19 A**, *Left*). The disproportional change of basal and apical dendrites hence led to a selective gating of inputs from CA3. As a consequence, the effect of basal/apical ratio was tested. Indeed, in case of equal basal/apical ratio this difference in excitation disappeared (see morphological modelling of scaled WT and APP/PS1 PCs in **Figure 19**, Mittag *et al.*, 2023). Nevertheless, the increase in activity for APP/PS1 cells after apical stimulation was minimal and can not explain the hyperexcitability, and especially burst increase, observed in APP/PS1 cells (see **Table 1** and Šišková *et al.*, 2014).

The modelling results in the second chapter point to the conclusion that morphological changes during AD are not leading to hyperactivity and enhanced bursting. The APP/PS1 cells display no hyperexcitability compared to the WT cells even though they are statistically smaller (see **Figure 8**). Other intrinsic and extrinsic alterations are necessary to explain the observed *in vivo* data of increased firing rate (Šišková *et al.*, 2014). Still the general opinion in the literature supports the idea that cells possess a specific structure in order to fulfil a specific function (Meinertzhagen *et al.*, 2009). However, it has been shown that dendrite morphology can be rather well predicted by anatomical connectivity (Cuntz *et al.*, 2010; Holtmaat and Caroni, 2016), and that connected neuron ensembles rather than single neurons constitute an emergent functional unit (Yuste, 2015). Instead of a clear structure to function relationship, this dissertation proposes that the structure and size of a cell change to keep the function stable: dendritic atrophy, in AD and other pathologies, might be a compensatory mechanism contributing to firing rate homeostasis after synapse loss. This is in line with several modeling studies (Platschek *et al.*, 2016, 2017; Cuntz *et al.*, 2021; Mittag *et al.*, 2023). Consequently, dendritic remodelling that happens after synapse loss in AD might help restore the IO function of the cell. IO homeostasis of that kind would be advantageous for the single neuron and moreover for the network that it is a part of. In the literature compensatory mechanisms have been already shown for several cell types in different animals, in experiments and modeling (Weaver and Wearne, 2008; Tripodi *et al.*, 2008; Cuntz *et al.*, 2013; Yin and Yuan, 2015; Platschek *et al.*, 2016; Lenz *et al.*, 2023). In AD, morphological compensatory effects have been observed which might work against the experimentally documented decline in cell function. As an example, an increase in size of the dendritic spines that are left after AD-related spine loss (Fiala *et al.*, 2002; Moolman *et al.*, 2004; Dickstein *et al.*, 2010; Neuman *et al.*, 2015) and topological modifications of dendrites (Graveland *et al.*, 1985; Arendt *et al.*, 1995; Szot *et al.*, 2006) are indications of a functional beneficial effect of spine and dendrite

alterations. Consistent with the concept of homeostasis, studies have shown a conservation of the electrophysiological features even during structural changes of AD-affected neurons (Rocher *et al.*, 2008; Abuhassan *et al.*, 2014; Somogyi *et al.*, 2016). From the perspective of metabolic cost and energy demand, dendritic degeneration with its shrinkage in overall cell size as well as reduction in the amount of membrane surface and available space for synaptic contacts has its advantages: it saves energy resources. In chapter three of this thesis, economy of energy is one of the cell's tasks considered in the performance and discussed later. Taken together, chapter one and two confirm, that the cell's size and shape is largely independent for it's output under controlled conditions of distributed synaptic activation (Cuntz *et al.*, 2021; Mittag *et al.*, 2023). This indicates, that AD-related alterations of the dendrite structure and size during the beginning of the disease progression compensate for synaptic loss as long as possible and maintain the IO function such as somatic firing. Consequently, other mechanisms are required to explain the observed hyperexcitability in AD.

6.3 Multiple intrinsic and extrinsic mechanisms of AD hyperexcitability

The results in chapter two established that hyperexcitability in APP/PS1 neurons could not be explained by changes in the PC morphology. For that reason, other possible alternative explanations of hyperexcitability were investigated. This included several observed configurations of extrinsic and intrinsic changes during AD, and its combinations: elevated input frequency and correlation of excitatory input, diminished GABAergic inhibitory input, ion channel modifications, and increased network burst activity (Mittag *et al.*, 2023). From this it was possible to identify three scenarios of hyperexcitability in AD.

Regarding Scenario 1, E/I imbalance, **Figure 21 A**: Previous studies of AD mouse models have shown modifications in E/I balance due to reduced inhibition and increased excitation (Busche *et al.*, 2008; Schmid *et al.*, 2016; Palop *et al.*, 2007; Palop and Mucke, 2016; Ambrad Giovannetti and Fuhrmann, 2019; Xu *et al.*, 2020; Hijazi *et al.*, 2020; Gervais *et al.*, 2022; Targa Dias Anastacio *et al.*, 2022). The simulation results support the conclusion that the observed impairment of GABAergic inhibition and the concomitantly enhanced glutamatergic excitation (increased input frequency and input correlations in AMPA/NMDA) can be one of the main contributions to the AD-related hyperexcitability (Mittag *et al.*, 2023). Notably, these alterations can reproduce the data (Šišková *et al.*, 2014) leading not only to elevated firing rates but also

to a transition of the firing mode from single to burst firing in APP/PS1 PCs.

Regarding Scenario 2, alterations in E/I balance and ion channels together, **Figure 21 B**: AD hyperexcitability has been previously associated with ion channel alterations such as down-regulation of I_{AHP} current (Beck and Yaari, 2008; Zhang *et al.*, 2014; Wang *et al.*, 2015a; Niday and Bean, 2021), up-regulation of I_{Na} and persistent I_{Nap} currents (Williams and Stuart, 1999; Yue *et al.*, 2005; Beck and Yaari, 2008; Liu *et al.*, 2015; Wang *et al.*, 2016; Ghatak *et al.*, 2019) and up-regulation of T-type calcium current I_{CaT} (Yaari *et al.*, 2007; Beck and Yaari, 2008; Cain and Snutch, 2013; Medlock *et al.*, 2018; Garg *et al.*, 2021) as described in Mittag *et al.* (2023). The results of this dissertation in chapter two suggest that solely intrinsic changes of the ion channels are not sufficient to account for the observed AD hyperexcitability. Indeed the mode change from solitary firing to predominantly burst firing (Šišková *et al.*, 2014) could not be shown, even though the simulations (**Figure 20 C**) showed several ion channel changes that increased the overall spike rate and burst firing. However, the combined alterations in E/I balance and ion channels simultaneously could replicate the AD-related hyperexcitability in a quantitative and qualitative manner including also the mode change from single spikes to bursting (**Figure 21 B**). Clearly, ion channels and their alterations are part of the AD pathology and can be one of the main contributions to the AD-related increased excitability (Mittag *et al.*, 2023). Ion channel changes can have a combinatorial effect that is non-linear and which can be described as synergistic: they can result in more triplets than *E/I imbalance* on its own, and with a smaller perturbation of the healthy control situation. As a control, the ion channel and network modifications were applied to the healthy group of the WT PCs. Importantly, it resulted in a higher increase in burst firing in comparison to the APP/PS1 cells (see **Figure 23**). Hence, one important conclusion in this dissertation is, that the dendritic degeneration is a stabilising attempt which can partially counter the increase in burst firing in APP/PS1 cells. Previous studies of computational and morphological modelling confirm the effect of dendritic size and topology on the bursting behaviour of neurons (van Elburg and van Ooyen, 2010). Different ion channel changes can lead to ion channel variability occurring among the cells. Therefore, the important concepts of ion channel degeneracy and homeostasis are discussed (Drion *et al.*, 2015; O'Leary, 2018; Goaillard and Marder, 2021; Schneider *et al.*, 2023). Single PCs can possibly develop differently during AD and show different (degenerate) ion channel changes still resulting in the same somatic hyperexcitability with enhanced firing and bursting (many to one mapping). Moreover, the stage and region of the disease progression can lead to different populations of the cells showing a variety of AD-effects displaying increased

or even decreased excitability (Busche *et al.*, 2008; Zott *et al.*, 2018; Dunn and Kaczorowski, 2019). This is in contrast to healthy cells, where ion channel variability and degeneracy can be helpful with respect to robustness of function and homeostasis (Marder and Goaillard, 2006; Schneider *et al.*, 2023). There is however a limit to the applicability of the homeostatic compensation (= stabilise/restore function). It might only be possible for a limited parameter region. The manifold and complex interplay within the multi-dimensional parameter space of the mechanisms (O'Leary, 2018; Yang *et al.*, 2022; Stöber *et al.*, 2023; Mittag *et al.*, 2023) complicate a homeostatic reaction. On the one hand, the high-dimensional parameter space potentially offers more solutions to reach homeostasis (Schneider *et al.*, 2023), on the other hand these solutions can be difficult to find as it includes the adjustment of many parameters and properties simultaneously (Yang *et al.*, 2022; Jedlicka *et al.*, 2022). One hypothesis for AD progression is the deteriorating loop of impaired function and failed homeostatic reaction which reinforce each other (Frere and Slutsky, 2018; Dunn and Kaczorowski, 2019). Therefore, the ion channel variability in AD and the function/dysfunction of firing rate homeostasis remain important topics for future experimental and computational research (Mittag *et al.*, 2023). In this thesis, the same AD-related intrinsic and extrinsic alterations were consistently implemented in all cells. It is however quite realistic that some of the AD cells show increased excitability because of impaired E/I balance while others display impaired E/I together with ion channel changes leading to hyperexcitability in a degenerate way (Mittag *et al.*, 2023). The heterogeneity of these effects between neurons may depend on the stage of AD progression and has to be investigated in further experiments.

Regarding Scenario 3, enhanced network activity in AD cell regions, **Figure 21 C**: network hyperexcitability has been previously shown (Šišková *et al.*, 2014; Palop and Mucke, 2016; Zott *et al.*, 2018; Selkoe, 2019; Maestú *et al.*, 2021; Kazim *et al.*, 2021). It ultimately can result into epileptiform activity (Minkeviciene *et al.*, 2009; Noebels, 2011). In this thesis, enhanced excitability of the surrounding excitatory network due to more input bursts into the APP/PS1 PCs was sufficient to raise the somatic burst rate of the cells including a change of firing mode from single spike to bursting (**Figure 21 C**) as observed in APP/PS1 mice (Šišková *et al.*, 2014). These results suggest that extrinsic network bursts are one of the main contributions to AD hyperexcitability (Mittag *et al.*, 2023). Notably, this means that the hyperactivity caused in one AD area, e.g. EC or CA3 (Khan *et al.*, 2013; Duffy *et al.*, 2015; Angulo *et al.*, 2017; Petrache *et al.*, 2019), could expand to other areas such as CA1 resulting in a network dependent increase in firing rate and bursting. Most neurons are part of a network. AD in one region can

easily spread into another due to the network connectivity, which would potentially lead to a domino effect infecting one network after the other with hyperactivity. One way to confirm this hypothesis in future research would be to apply information theoretical measures to analyse AD-related changes combined with the spreading of activity in hippocampal areas, as illustrated in Świetlik *et al.* (2019).

In chapter two, this dissertation investigated AD cells at a time of the disease progression that shows clear formation of amyloid plaques in the hippocampus. Besides that, different AD stages and regions have to be further investigated. At an earlier stage before plaque formation, transgenic rats in an *in vivo* study showed hyperexcitability that was mainly caused by increased intrinsic excitability (Sosulina *et al.*, 2021). It follows, that an impaired extrinsic E/I ratio (Busche and Konnerth, 2016) would be expected to be initiated and be important at later phases of AD (Mittag *et al.*, 2023). The precise sequence of pathophysiological events still has to be demonstrated though. One idea is to compare several time points of the disease with respect to the underlying mechanisms and pathological progression, especially the increasingly synergistic effects of combined intrinsic and extrinsic alterations. An example study of APP/PS1 mice including and comparing three different ages originates from the group of Vitale *et al.* (2021). They showed alterations in membrane time constant, HCN channels, AP width and firing behaviour in APP/PS1 mice depending on the age and AD stage. It is important to note that in the mentioned study the activation was caused by somatic current injections. However, the simulations in this thesis suggest, that for a complete understanding of AD hyperactivity and its development in single cells and networks, the synaptically activated firing behaviour is more realistic and relevant. The focus in chapter two was exclusively on the AD-based hyperexcitability in the hippocampus region of APP/PS1 model mice. Increased activity due to AD in other regions and for other AD models as well as other species should be further investigated in experimental and computational studies as they might reveal other mechanisms and interactions (Mittag *et al.*, 2023). For example, recent investigations have shown that increased excitability in the somatosensory cortex of the familial AD mouse model is a consequence of an impaired function in the firing of GABAergic parvalbumin interneurons which is caused by changes in the Kv3 potassium channel (Olah *et al.*, 2022).

The mechanisms investigated in chapter two do not yet yield the complete picture of possible AD-related changes involved in hyperexcitability. Hence, it is worth to mention a few relevant

features that should be further examined. For instance, amyloid-beta accumulation is an important characteristics of AD and potentially has an effect on the extracellular glutamate concentrations (Bezprozvanny and Mattson, 2008; Scimemi *et al.*, 2013; Bao *et al.*, 2021; Targa Dias Anastacio *et al.*, 2022). The thesis attempted to simulate amyloid-beta accumulation only indirectly by an increased NMDA time constant meaning a delayed clearance of synaptically released glutamate. The results showed an increased firing rate of APP/PS1 cells (see **Figure 22 B**) due to an increased single spike rate but with a constant burst rate (Mittag *et al.*, 2023). This entails that other changes are necessary to explain the data of hyperactivity. Alterations in the synaptic plasticity, suppressed LTP and memory impairments are further consequences of AD and amyloid-beta (Rowan *et al.*, 2003; Shankar *et al.*, 2008). Nevertheless, the interactions are complicated and could potentially also lead to hypoactivity (Trinchese *et al.*, 2004). Furthermore, the AIS has a strong influence on the cell excitability (Kuba *et al.*, 2014; Evans *et al.*, 2015). For example, alterations in AIS plasticity following amyloid-beta formation in AD affect firing behaviour (León-Espinosa *et al.*, 2012; Sun *et al.*, 2014; Zhang *et al.*, 2014; Dongmin Sohn *et al.*, 2019; Booker *et al.*, 2020). One limitation of the modelling performed in chapter two is, that AIS changes were not included since there was no AIS anatomical information available in the morphology data sets (Mittag *et al.*, 2023). Future research therefore should investigate the role of the AIS and its potential changes in AD and hyperexcitability.

In conclusion of the second chapter of this dissertation, several mechanisms contributing to hyperexcitability in AD were revealed. Degeneracy with respect to these involved intrinsic and extrinsic mechanisms can be a useful concept to understand the AD pathology (Tononi *et al.*, 1999; Edelman and Gally, 2001). Systems within the brain can be considered degenerate with the following definition: multiple distinct mechanisms are sufficient, but none of them is necessary, to fulfil a certain function. In the same manner this also accounts for pathomechanisms leading to dysfunction (from regular- to hyper-activity, Neymotin *et al.*, 2016; Ratté and Prescott, 2016; O'Leary, 2018; Medlock *et al.*, 2022; Kamaleddin, 2022; Mittag *et al.*, 2023). In this thesis, Scenario 1 with increased E/I ratio, or Scenario 2 with increased E/I ratio combined with ion channel changes, or Scenario 3 with increased network burst input are sufficient to explain the mode change from single AP to burst firing (Mittag *et al.*, 2023, *in silico* study reproducing Šišková *et al.*, 2014). No scenario on its own is necessary, though all scenarios include extrinsic changes. The observed degeneracy of mechanisms leading to pathologies can make it difficult to fix a function as one mechanism is likely not

sufficient for the recovery (Kamaleddin, 2022; Stöber *et al.*, 2023; Mittag *et al.*, 2023). Various homeostatic mechanisms (O'Leary, 2018; Sakurai *et al.*, 2014; Onasch and Gjorgjieva, 2020) further compound clinical approaches as individual mechanism therapies are ineffective (Ratté *et al.*, 2014; Ratté and Prescott, 2016). Future therapies could benefit from the results obtained in this thesis by implementing approaches that incorporate multiple scenarios and pathomechanisms underlying AD hyperexcitability (Mittag *et al.*, 2023).

6.4 Pareto optimal GCs and beyond

Somatic firing rate and potential are important indicators of a neuron's IO function. Usually, additional computations operate within the neuron which define its function more precisely (London and Häusser, 2005). For instance, GCs of the DG perform pattern separation between input and output as their major function (Sahay *et al.*, 2011; Schmidt *et al.*, 2012; Rolls, 2013). This was the topic of the third and final chapter of this dissertation.

In general, function and computation of a neuron as a single unit and within a network are dependent on cell type, location, connectivity, developmental stage, and other factors (Pravettoni *et al.*, 2000; Masland, 2004; Espósito *et al.*, 2005; Marder and Goaillard, 2006; Sahay *et al.*, 2011; McKenna *et al.*, 2014; Yuste, 2015). These characteristics in turn differ in their underlying mechanisms and constraints. One particular constraint of the cell is the amount of available resources at its disposal or, in other words, the cell has to use its energy efficiently (Attwell and Laughlin, 2001; Quintela-López *et al.*, 2022). Taken together, functions and constraints of a neuron interact. Intriguingly, the recent study by Ali *et al.* (2022) has shown that an energy constraint alone can be sufficient to give rise to emergent functions such as predictive coding in an artificial neural network. Thereby, predictive coding entails the hypothesis that the brain inhibits future input of the senses which match its predictions and that it highlights the input which is surprising and has most informative content. In that way, efficient coding naturally leads to a network that is favorable in predicting the world since this minimises the required energy. Similarly, the GCs of the DG have to perform their pattern separation function in an energy efficient (economic) manner. This was the motivation to investigate pattern separation (Bird *et al.*, 2024) and economy for GCs as a two-task optimisation problem by applying the Pareto perspective in the third chapter (Alon, 2006; Jedlicka *et al.*, 2022). Pareto optimality was a helpful guide here to find the best group of GC models performing both

tasks simultaneously, especially, since the improvement in one task typically came with a trade-off in the other. The experimentally validated (original) GC model (Beining *et al.*, 2017) turned out to be on the Pareto line as one of the best models for both tasks without being the best for the individual tasks alone (**Figure 24**). The original model by Beining *et al.* (2017) was created using the vast amount of literature and experiments (mainly electrophysiological data measuring channel densities and features of the somatic AP) available at the time. It was not tuned to the performance of pattern separation or to save energy. Nevertheless, the results in chapter three of this thesis demonstrate, that the original GC model seems Pareto optimal for both of these tasks. The comparison of the original GC model to a population of valid, random GC models (1140 models are valid among 20000 randomly created models with a $Fitness < 2$, Schneider *et al.*, 2023) reveals that the population models can display quite different performances of pattern separation and economy, even though they initially display similar somatic firing behaviour. This underlines the astonishing function of the original GC model to not only fit the experimental data but to also perform Pareto optimal for pattern separation and economy for which it was not designed. Remarkably, it points to an evolutionary development of the GC with all its internal mechanisms to function well for pattern separation with low energy use and a behavioural constraint (Laughlin and Sejnowski, 2003; Shoval *et al.*, 2012; Pallasdies *et al.*, 2021). Thereby, Pareto optimality is a possible explanation for how the GCs evolved to their optimal biophysics (Shoval *et al.*, 2012; Jedlicka *et al.*, 2022). Additionally, the results from chapter three showed that the GC performances were robust with little change in the Pareto front even during moderate noise. This economic and robust pattern separation ability of GCs in the DG is consistent with literature as part of the memory function of the hippocampus (Yassa and Stark, 2011; Opitz, 2014; Madroñal *et al.*, 2016). In order to do that, the GCs control the flux and decorrelation of information from neocortex to hippocampal regions via perforant pathway of the EC (Jarrard, 1995; Amaral *et al.*, 2007; Lopez-Rojas and Kreutz, 2016; Burke *et al.*, 2018) with sparse, energy-efficient activity and coding (Leutgeb *et al.*, 2007; Krueppel *et al.*, 2011; Tonegawa *et al.*, 2015; GoodSmith *et al.*, 2017; Jaeger *et al.*, 2018).

A promising explanation of energy efficiency in neurons has been previously proposed and investigated by Alle *et al.* (2009) in mossy fibers. They showed a link between low overlap of sodium/potassium (Na^+/K^+) currents during spiking and minimal energy used for this process. Otherwise, a high overlap would lead to more sodium load needed for the process, and therefore also more energy. During the overlap of the currents, sodium and potassium

compete with each other and cancel each of their intended effects of depolarisation or repolarisation of the neuron (Sengupta *et al.*, 2010; Hasenstaub *et al.*, 2010). The energy during that overlap is wasted. Accordingly, the current overlap for the population of GC models was examined and likewise a correlation between the overlap of somatic Na^+/K^+ and the ATP consumption was found. Or vice versa, the current overlap was anti-correlated with the economy function of the cells (**Figure 25**). Ideally, the currents reduce their overlap by faster Na^+ channel inactivation and a delayed onset of K^+ channel opening (Crotty and Levy, 2007; Sengupta *et al.*, 2010; Stemmler *et al.*, 2011; Yu and Yu, 2017). Furthermore, the results in chapter three showed that the original GC model displays minimal currents' overlap and seems Pareto optimal near perfect energy economy among the population of investigated models that are valid. It is important to note, that the energy estimation in this dissertation is based on an ion counting system relating the ATP used for the Na^+/K^+ pumps (**Equation 41**, Attwell and Laughlin, 2001). However, other approaches of calculating the energy usage of the cell are possible. For example, previous work calculated the total electrochemical cell energy as a function of its state variables (Moujahid and d'Anjou, 2012). Surprisingly, the pattern separation performance via relative redundancy reduction in this thesis showed anti-correlation as well with the currents' overlap, i.e. it preferred separate Na^+/K^+ currents. One reason for this interesting relation could be that a clear spiking pattern is dependent on the separation of Na^+/K^+ currents to generate the action potentials accurately in time. Or, more likely even, the separate currents add noise to the signal and therefore output pattern which makes it more distinguishable from the input pattern. Previously, there have been modeling attempts to investigate the link between Na^+/K^+ currents and reliable spike timing (Schreiber *et al.*, 2004). In another study, it was shown how voltage-gated conductances (including Na^+/K^+ channels) could be modified to learn a maximised information transfer of MI (Stemmler and Koch, 1999). Such MI measure was also part of the relative redundancy reduction measure for pattern separation in this thesis. Future research should investigate the link between ion channel mechanisms and cell function optimisation such as pattern separation maximisation further.

What is a cell's actual fitness function or objective to optimise (Van Geit *et al.*, 2008)? In a previous study by Schneider *et al.* (2023), the selection of valid GCs was determined via similarity to somatic electrophysiological features such as AP width and height and ISI ($Fitness < 2$). Notably, dendritic features such as backpropagating action potentials were not included as a constraint for the comparison. In this dissertation however, further tasks were

added to evaluate the performance of GC models: pattern separation and economy. As a result, the valid population models show differences in pattern separation and energy economy, and therefore can be discriminated by them. When these optimisation tasks were incorporated into the function of the GCs, only a handful of models remained, including the original model, which showed Pareto optimality. In general, it is not known what the total objective function of the GC is. It is reasonable to make assumptions based on biophysical experiments, showing the involvement of GCs in pattern separation (Yassa and Stark, 2011) and using the metabolic resources rationally (Alle *et al.*, 2009; Sengupta *et al.*, 2010; Schmidt-Hieber and Bischofberger, 2010; Yu and Yu, 2017). Several recent studies have successfully used similar approaches by including energy constraints in the function and optimisation of neuron models (Remme *et al.*, 2018; Fardet and Levina, 2020; Ali *et al.*, 2022). Additionally, other constraints or tasks could very well be involved in the natural function of the GC beyond a two-task optimisation problem. For instance, one could also include the function of pattern completion for mGCs (Nakashiba *et al.*, 2012), dendritic computations (London and Häusser, 2005; Larkum *et al.*, 2007) or several plasticity phenomena (Morrison *et al.*, 2008; Magee and Grienberger, 2020; Inglebert *et al.*, 2020). In this thesis, the constraints arise from the implemented morphological and biophysical models. Subsequently, a population of models was selected which all show very similar somatic behaviour as another constraint. Without any further conditions, the results indicate, that for pattern separation and economy the original GC model functions Pareto optimal among a population of models.

In chapter three, the Pareto front location was analysed for several conditions of input and noise. Further, an optimisation algorithm was implemented to find channel compositions (starting with the original GC mechanisms) which could move the Pareto front in the direction of improved relative redundancy reduction or economy or both simultaneously for GCs. Without the constraint of the somatic $Fitness$ function, which was a boundary of the GC population models originally, the algorithm eventually found channel solutions that pushed the Pareto front further (**Figure 27 C**, 26 solutions in total). Importantly, the performance improvement was small (max. 20% for economy and max. 10% for relative redundancy reduction). Control simulations in the $20Hz$ input condition revealed that the same models did not perform as well as in the $10Hz$ input condition for which they were optimized: the number of solutions for better pattern separation performance reduced to 13% and the number of solutions for both, better pattern separation performance and economy together, reduced even to just 5%. Looking at the channel modifications that contributed to this performance

improvement, certain trends could be identified. An increase in calcium and calcium-activated potassium channels as well as the big voltage-gated potassium channel (sometimes two to three times as much as in the original model, which seems biologically unrealistic) was observed. Especially, a decrease in the axon hillock sodium *na8st* channel and an increase in the dendritic potassium *Kv42* channel could be seen. This is in agreement with an earlier finding in this thesis, which showed correlations between performance and the conductances of *na8st* and *Kv42* for the population models (**Figure 25 B**). What is the location of the Pareto front? For medium noise the front was quite robust. For high noise the pattern separation was impaired but economy could be consolidated. With a parameter optimisation algorithm without any further constraint the front moved slightly towards better performances of pattern separation and economy. More constraints or tasks could move the front again, likely towards worse performances of the current tasks due to trade-offs. Pareto optimality can help to investigate this further.

Ion channel degeneracy played an important role in the second chapter of the thesis regarding hyperexcitability in AD cells. On the one hand, degeneracy and variability of ion channels can be a helpful feature for robustness and homeostasis of a system to keep a stable function of the cell. For example, a particular channel failure might be compensated by other redundant channels (many to one mapping of channels to function, Rich *et al.*, 2022; Schneider *et al.*, 2023). On the other hand, in a pathological development of the cell, multiple pathomechanisms including different ion channel changes could lead to the same pathology, e.g. AD hyperexcitability, and therefore making it very difficult to apply efficient treatment strategies (O'Leary, 2018; Stöber *et al.*, 2023; Yang *et al.*, 2022; Yang and Prescott, 2023; Mittag *et al.*, 2023). Notably, ion channel variability and degeneracy played a major role in the third chapter regarding GC performance as well. Schneider *et al.* (2023) showed degeneracy of the GC model regarding its various ion channel compositions and its distinct somatic spiking behaviour, and ultimately emphasized the advantage of its biological existence for homeostasis. However, the simulations in chapter three exposed, that the inclusion of other tasks in the cell function reduced the population of GCs to a handful of models that performed Pareto optimal for pattern separation and economy. It follows, that a perturbation of an ion channel can potentially be compensated by changes of other channels to fulfil the somatic GC behaviour in a degenerate way. Unfortunately, these compensations could at the same time perturb the functions of pattern separation and economy since the effect of an ion channel is usually not limited to one feature (see pleiotropy in Edelman and Gally, 2001; Yang and Prescott, 2023).

In consequence, to keep all functions stable an even higher degree of degeneracy might be necessary to have enough adjustment potential. As an example, it is easier to regulate ion channels in a homeostatic manner for just invariant somatic behaviour compared to invariant somatic behaviour, pattern separation and economy in parallel. As another example, the optimisation algorithm applied in this thesis found good solutions for pattern separation and economy by adjusting mainly the sodium channel, which could be therefore seen as one mechanism of the GC function homeostasis. However, the $Fitness$ function of the GC somatic spike behaviour was disturbed in that case. It is clear that homeostasis of the GCs several functions is more complicated than previously thought and involves likely different regulatory systems to avoid unintended effects (O'Leary, 2018; Niemeyer *et al.*, 2021; Yang *et al.*, 2022). Energy regulation seems to be just one candidate to control for behaviour (Vergara *et al.*, 2019). The existence of multiple homeostatic regulatory systems opens up more chances to counter pathological developments for neuron functions (Davis and Bezprozvanny, 2001; Marder and Goaillard, 2006; Cannon and Miller, 2016).

6.5 The role of young abGCs

Pattern separation is not only a function of mGCs (Leutgeb *et al.*, 2007; Bakker *et al.*, 2008; Neunuebel and Knierim, 2014; Yassa and Stark, 2011; Chavlis and Poirazi, 2017) but possibly involves young, abGCs as well (Clelland *et al.*, 2009; Johnston *et al.*, 2016). However, the exact function of abGCs and what part each subpopulation of old and young GCs play in pattern separation is still on debate in the literature (Kempermann, 2002; Jessberger and Kempermann, 2003; Lopez-Rojas and Kreutz, 2016; Johnston *et al.*, 2016). In addition, previous studies have shown that the role of young GCs is highly dependent on activity and regulation during maturation (Fabel and Kempermann, 2008; Kempermann *et al.*, 2015). The computational results in this dissertation confirm the major role of newly formed GCs, and thus neurogenesis, in the GC function of pattern separation and memory (see also Sahay *et al.*, 2011; Tuncdemir *et al.*, 2019; Kropff *et al.*, 2015). Indeed, the abGCs seem to be Pareto optimal for pattern separation and economy with a tendency towards lower energy usage compared to mGCs (**Figure 28**). An interpretation of this result could very well be, that neurogenesis is an energy-intense process (Perera *et al.*, 2011). Therefore, it might be initially more optimal to save energy while performing the pattern separation function. At a later maturation stage the GC has more energy at its disposal and hence can perform more to the right of the Pareto front with

better pattern separation performance to the cost of less economy, as shown by the mGCs. The mice used in part three of this research were 2-4 months old and 11–12 months old adult male transgenic mice containing matured GCs, with either the compartmental model by Beining *et al.* (2017) implemented for the mGCs or the model version with altered ion channel densities for the abGCs. Future studies should look at several temporal stages of the maturation of GCs from new to mature under the influence of activity and plasticity to investigate how the function of the GC arises and how it is optimised for pattern separation. Importantly, the integration of the single GC into its DG network needs to be investigated further as ultimately no cell is an island and rather part of a subpopulation or circuit function (Kee *et al.*, 2007; Tuncdemir *et al.*, 2019). This network integration however can be source of a pathology as well, especially when it goes wrong, e.g. as seen by epileptic seizures due to increased GC network activity after neurogenesis (Parent *et al.*, 1997; Sparks *et al.*, 2020 and see also Stöber *et al.*, 2023). Mostly though, the literature shows a positive effect of neurogenesis and the integration of new GCs into the hippocampal network on memory, behaviour and well-being of animals: there seems to be a link between enhanced learning and increased neurogenesis (Van Praag *et al.*, 1999; Gould *et al.*, 1999; Leuner *et al.*, 2006) as well as heightened stress and decreased neurogenesis (Gould and Tanapat, 1999; Snyder *et al.*, 2011). The detailed mechanisms underneath the benefits of neurogenesis are still not fully known though. One possibility is that new GCs temporarily increase plasticity (Kropff *et al.*, 2015; Kempermann, 2022) and add to sparsity (Lodge and Bischofberger, 2019), both of which can be beneficial for pattern separation. Alternatively, the new GCs help forgetting old memories and forming new ones via easier integration of new information into familiar contexts. This is a possible strategy to solve the plasticity-stability dilemma: balancing the acquisition of new memories without disrupting old memories too strongly (Yau *et al.*, 2015; Kempermann, 2022). The balance between old and new memories could potentially be established by a balance between old and new GC populations.

Additionally, a length dependency was revealed by comparing all cell reconstructions. This is in contrast to the results in chapter one regarding dendritic constancy: the thesis revealed that there is an anti-correlation between cell size and economy as well as pattern separation performance. This means, smaller GCs on average perform better than bigger GCs. Regarding energy demand, it is easy to see that a smaller cell with less surface and fewer ion channels needs less energy to perform and has less metabolic demand (Miettinen and Björklund, 2017). It is however surprising that a smaller cell also performs better in pattern separation. Why do

bigger neurons exist then? This possibly relates to other GC functions and computations of their dendrites (London and Häusser, 2005; Larkum, 2013). For instance, a recent paper by Wilmes and Clopath (2023) pointed to the importance of dendrites in mitigating the plasticity-stability dilemma, which was mentioned for abGCs earlier. Moreover, GCs are part of a bigger network in which they possibly connect more optimally with bigger cell size (Bird *et al.*, 2021a). Previously, Chklovskii (2000) and Cuntz *et al.* (2007) investigated and linked optimisation of morphology and connectivity. The results in chapter three indicate, that cell morphology, network function and connectivity are features that should be investigated further in their interrelation, particularly for the GCs and their pattern separation performance. This includes the network integration and interplay of the old mGC and young abGC subpopulations. These constraints and functions could be part of a multi-dimensional *Fitness* or optimisation function beyond just somatic behaviour (Schneider *et al.*, 2023) and the two-task optimisation of single cell pattern separation and economy which were the topic of the third chapter of this dissertation. A recent promising approach to model the DG-EC-CA3 network function including information transfer and pattern separation as well as completion originates from the group of Müller-Komorowska *et al.* (2023). However, single cell compartmental modelling details were not fully included. Ideally, single cell and network approaches should be combined. A detailed single cell bottom-up approach investigating the GC pattern separation function with energetic constraints, as done in this thesis, is an important first step. Future research should broaden the focus of investigation and consider GCs in a more holistic circuit manner, with additional network functions and constraints, including the integration of young GCs.

6.6 Closing remarks

At the conclusion of this dissertation I refer again to the initial questions: what constitutes the IO relationship of nerve cells? What mechanisms or principles underlie their IO function?

First, the study of the structure-to-function relationship is a major aim in neuroscience. Morphological size and structure clearly influence the neural IO function. Complementary, in this dissertation I reveal a fundamental principle, called dendritic constancy, which entails that the IO function can in fact be independent of cell size under certain conditions.

Second, ion channel variability is an important phenomenon observed within nerve cells. I show in this thesis, that the specifically altered expression of ion channels during pathological cell development can lead to the observed impaired IO function (e.g. in AD cells). Likewise, the specific ion channel expression arising during healthy cell development can be the resulting evolutionary solution of cells to optimise their performance (e.g. in GC pattern separation).

Together, morphological structure and the involved non-linear ion channel mechanisms within that structure strongly affect the IO function of nerve cells revealing particular structure-to-function connections. I demonstrate this for three *in silico* investigations of hippocampal neurons and their known IO activity in this dissertation. Moreover, the results have a broader relevance and can likely be generalised to other nerve cells beyond the hippocampus and further IO functions during healthy and pathological evolution, though this has to be scrutinized.

Thereby, Pareto optimality has turned out to be a useful explanatory tool, especially for biological systems such as the nerve cells in this thesis, to investigate several tasks and/or constraints simultaneously as part of the neural IO function.

7 Publications

*Cuntz H, Bird AD, **Mittag M**, Beining M, Schneider M, Mediavilla L, Hoffmann FZ, Deller T, Jedlicka P (2021)
A general principle of dendritic constancy: A neuron's size- and shape-invariant excitability. *Neuron* 109: 3647–3662.
doi: 10.1016/j.neuron.2021.08.028

***Mittag M**, Mediavilla L, Remy S, Cuntz H, Jedlicka P (2023)
Modelling the contributions to hyperexcitability in a mouse model of Alzheimer's disease. *Journal of Physiology*
doi: 10.1113/JP283401

Rößler N, Jungenitz T, Sigler A, Bird AD, **Mittag M**, Rhee JS, Deller T, Cuntz H, Brose N, Schwarzacher SW, Jedlicka P (2023)
Skewed distribution of spines is independent of presynaptic transmitter release and synaptic plasticity, and emerges early during adult neurogenesis. *Open Biology*
doi: 10.1098/rsob.230063

In preparation:

Del Turco D, Paul MH, Rietsche M, Schlaudraff J, Bas-Orth C, **Mittag M**, Jedlicka P, Drakew A, Kreuzer A, Roeper J, Deller T
Transgenic overexpression of the plasticity-related protein Synaptopodin in adult mice increases the number of spine apparatuses and activates silent synapses of dentate granule cells

***Mittag M**, Bird AD, Cuntz H, Jedlicka P
Modelling suggests biophysics of dentate granule cells are Pareto optimal for the simultaneous maximisation of economy and pattern separation

* relevant for this dissertation

8 Acknowledgements

This dissertation is the result of years of curious learning and diligent working. Science is creative, complex and collaborative; without a network of colleagues, friends and family this work would not have been possible.

First, I want to express my gratitude to Prof. Dr. Peter Jedlička and Dr. Hermann Cuntz for initially giving me a chance to do research and overall for their academic and scientific guidance and support over the past years. Their perspective and expertise showed me the importance of the small but essential details as well as the wider picture and context of our research projects. Second, I want to thank Prof. Dr. Christian Heiliger for being my official supervisor. A special thanks goes to Dr. Alexander Bird, who always had insightful and invaluable comments and inputs in our collaborative research projects.

I further want to thank all my colleagues at the ESI in Frankfurt and the 3R center in Gießen, who provided me with short relaxing chats or inspiring scientific talks.

Life in general and scientific work in particular can only be prosperous as a nurturing balance of heart and mind. I want to seize the occasion here to show my gratitude to my sisters Anika and Kathrin for their emotional support and love throughout our lives; the three Musketeers battle together. To my brilliant friends: you are family too. I therefore want to give a hug and appreciation to Daniel, Emjay, Wegi, Wiebke, Nina, Pablo and all my friends here in Frankfurt. You probably do not even know how important you were in finishing this work and how vital you are in my day-to-day life.

Dear Ximena Icaria Salinas Hernández, I was so incredibly lucky to have found you, the love of my life, while figuring out my scientific life. We went on the PhD journey together and now continue our journey in life together. Along the way we got married and I got a whole new, loving and amazing family with you, Margarita, Ulises and Jesus to share this adventure with. Ximena, your love and brightness is second to none and not only helped me with this dissertation but made me a better person in general. In particular, thank you for going through my thesis so thoroughly and not shying away from criticizing me. Thank you also for letting me ramble on all the time about my research projects. Fortunately, we share this passion. And over all, thank you for your support, love and motivation; you inspire me, and this thesis would not have been without you. I am eternally grateful for you and our family. All my love goes to you.

9 Declaration

I declare that I have completed this dissertation single-handedly without the unauthorized help of a second party and only with the assistance acknowledged therein. I have appropriately acknowledged and cited all text passages that are derived verbatim from or are based on the content of published work of others, and all information relating to verbal communications. I consent to the use of an anti-plagiarism software to check my thesis. I have abided by the principles of good scientific conduct laid down in the charter of the Justus Liebig University Giessen "Satzung der Justus-Liebig-Universitat Gießen zur Sicherung guter wissenschaftlicher Praxis" in carrying out the investigations described in the dissertation.

Gießen, 5.12.2023

10 References

References

Abraham WC, Bear MF (1996) Metaplasticity: the plasticity of synaptic plasticity. *Trends in neurosciences* 19:126–130.

Abraham WC, Jones OD, Glanzman DL (2019) Is plasticity of synapses the mechanism of long-term memory storage? *npj Science of Learning* 4:9.

Abraham WC, Mason-Parker SE, Bear MF, Webb S, Tate WP (2001) Heterosynaptic metaplasticity in the hippocampus in vivo: a bcm-like modifiable threshold for ltp. *Proceedings of the National Academy of Sciences* 98:10924–10929.

Abuhassan K, Coyle D, Belatreche A, Maguire L (2014) Compensating for synaptic loss in alzheimer's disease. *Journal of computational neuroscience* 36:19–37.

Adlard PA, Vickers JC (2002) Morphologically distinct plaque types differentially affect dendritic structure and organisation in the early and late states of Alzheimer's disease. *Acta Neuropathologica* 103:377–383.

Ali A, Ahmad N, de Groot E, van Gerven MAJ, Kietzmann TC (2022) Predictive coding is a consequence of energy efficiency in recurrent neural networks. *Patterns* 3.

Alle H, Roth A, Geiger JR (2009) Energy-efficient action potentials in hippocampal mossy fibers. *Science* 325:1405–1408.

Almog M, Korngreen A (2014) A quantitative description of dendritic conductances and its application to dendritic excitation in layer 5 pyramidal neurons. *Journal of Neuroscience* 34:182–196.

Alon U (2006) *An introduction to systems biology: design principles of biological circuits* Chapman and Hall/CRC.

Alvarez-Buylla A, Garcıa-Verdugo JM (2002) Neurogenesis in adult subventricular zone. *Journal of Neuroscience* 22:629–634.

Amaral DG, Scharfman HE, Lavenex P (2007) The dentate gyrus: fundamental neuroanatomical organization (dentate gyrus for dummies). *Progress in brain research* 163:3–790.

Ambrad Giovannetti E, Fuhrmann M (2019) Unsupervised excitation: GABAergic dysfunctions in Alzheimer's disease. *Brain Research* 1707:216–226.

Anand KS, Dhikav V (2012) Hippocampus in health and disease: An overview. *Annals of Indian Academy of Neurology* 15:239.

Anderton BH, Callahan L, Coleman P, Davies P, Flood D, Jicha GA, Ohm T, Weaver C (1998) Dendritic changes in Alzheimer's disease and factors that may underlie these changes. *Progress in Neurobiology* 55:595–609.

Anekonda TS, Quinn JF, Harris C, Frahler K, Wadsworth TL, Woltjer RL (2011) L-type voltage-gated calcium channel blockade with isradipine as a therapeutic strategy for Alzheimer's disease. *Neurobiology of Disease* 41:62–70.

Ang CW, Carlson GC, Coulter DA (2005) Hippocampal CA1 circuitry dynamically gates direct cortical inputs preferentially at theta frequencies. *Journal of Neuroscience* 25:9567–9580.

Angulo SL, Orman R, Neymotin SA, Liu L, Buitrago L, Cepeda-Prado E, Stefanov D, Lytton WW, Stewart M, Small SA, Duff KE, Moreno H (2017) Tau and amyloid-related pathologies in the entorhinal cortex have divergent effects in the hippocampal circuit. *Neurobiology of Disease* 108:261–276.

Arellano JI, Benavides-Piccione R, DeFelipe J, Yuste R (2007) Ultrastructure of dendritic spines: Correlation between synaptic and spine morphologies. *Frontiers in Neuroscience* 1:131–143.

Arendt T, Brückner MK, Bigl V, Marcova L (1995) Dendritic reorganisation in the basal forebrain under degenerative conditions and its defects in Alzheimer's disease. III. The basal forebrain compared with other subcortical areas. *Journal of Comparative Neurology* 351:223–246.

Aroor A, Brewster AL (2021) Dendritic and spine loss in epilepsy: What seizures got to do with it? *Epilepsy Currents* 21:186–188.

Ascoli GA, Donohue DE, Halavi M (2007) Neuromorpho. org: a central resource for neuronal morphologies. *Journal of Neuroscience* 27:9247–9251.

Attwell D, Laughlin SB (2001) An energy budget for signaling in the grey matter of the brain. *Journal of Cerebral Blood Flow & Metabolism* 21:1133–1145.

Augustinack JC, Schneider A, Mandelkow EM, Hyman BT (2002) Specific tau phosphorylation sites correlate with severity of neuronal cytopathology in Alzheimer's disease. *Acta Neuropathologica* 103:26–35.

Bakken TE, Stevens CF (2012) Visual system scaling in teleost fish. *Journal of Comparative Neurology* 520:142–153.

Bakker A, Kirwan CB, Miller M, Stark CE (2008) Pattern separation in the human hippocampal ca3 and dentate gyrus. *science* 319:1640–1642.

Ballesteros-Yáñez I, Benavides-Piccione R, Elston GN, Yuste R, DeFelipe J (2006) Density and morphology of dendritic spines in mouse neocortex. *Neuroscience* 138:403–409.

Baloyannis SJ (2009) Dendritic pathology in Alzheimer's disease. *Journal of the Neurological Sciences* 283:153–157.

Bannister NJ, Larkman AU (1995) Dendritic morphology of CA1 pyramidal neurons from the rat hippocampus: I. Branching patterns. *Journal of Comparative Neurology* 360:150–160.

Bao Y, Yang X, Fu Y, Li Z, Gong R, Lu W (2021) NMDAR-dependent somatic potentiation of synaptic inputs is correlated with β amyloid-mediated neuronal hyperactivity. *Translational Neurodegeneration* 10:1–15.

Barker JM, Boonstra R, Wojtowicz JM (2011) From pattern to purpose: how comparative studies contribute to understanding the function of adult neurogenesis. *European Journal of Neuroscience* 34:963–977.

Beck H, Yaari Y (2008) Plasticity of intrinsic neuronal properties in CNS disorders. *Nature Reviews Neuroscience* 9:357–369.

Beining M, Mongiat LA, Schwarzacher SW, Cuntz H, Jedlicka P (2017) T2N as a new tool for robust electrophysiological modeling demonstrated for mature and adult-born dentate granule cells. *Elife* 6:e26517.

Belleau EL, Treadway MT, Pizzagalli DA (2019) The impact of stress and major depressive disorder on hippocampal and medial prefrontal cortex morphology. *Biological psychiatry* 85:443–453.

Benavides-Piccione R, Fernaud-Espinosa I, Robles V, Yuste R, Defelipe J (2013) Age-based comparison of human dendritic spine structure using complete three-dimensional reconstructions. *Cerebral Cortex* 23:1798–1810.

Benavides-Piccione R, Regalado-Reyes M, Fernaud-Espinosa I, Kastanauskaite A, Tapia-González S, León-Espinosa G, Rojo C, Insausti R, Segev I, Defelipe J (2020) Differential structure of hippocampal CA1 pyramidal neurons in the human and mouse. *Cerebral Cortex* 30:730–752.

Benuskova L, Abraham WC (2007) Stdp rule endowed with the bcm sliding threshold accounts for hippocampal heterosynaptic plasticity. *Journal of computational neuroscience* 22:129–133.

Bernstein J (1902) Untersuchungen zur thermodynamik der bioelektrischen ströme. *Pflügers Archiv European Journal of Physiology* 92:521–562.

Berridge MJ (2014) Calcium regulation of neural rhythms, memory and Alzheimer's disease. *Journal of Physiology* 592:281–293.

Bezchlibnyk YB, Stone SS, Hamani C, Lozano AM (2017) High frequency stimulation of the infralimbic cortex induces morphological changes in rat hippocampal neurons. *Brain Stimulation* 10:315–323.

Bezprozvanny I, Mattson MP (2008) Neuronal calcium mishandling and the pathogenesis of Alzheimer's disease. *Trends in Neurosciences* 31:454–463.

Bicknell BA, Häusser M (2021) A synaptic learning rule for exploiting nonlinear dendritic computation. *Neuron* 109:4001–4017.

Bird AD, Cuntz H (2016) Optimal current transfer in dendrites. *PLoS computational biology* 12:e1004897.

Bird AD, Deters L, Cuntz H (2021a) Excess neuronal branching allows for local innervation of specific dendritic compartments in mature cortex. *Cerebral Cortex* 31:1008–1031.

Bird AD, Jedlicka P, Cuntz H (2021b) Dendritic normalisation improves learning in sparsely connected artificial neural networks. *PLOS Computational Biology* 17:e1009202.

Bird AD, Cuntz H, Jedlicka P (2024) Robust and consistent measures of pattern separation based on information theory and demonstrated in the dentate gyrus. *PLOS Computational Biology* 20:e1010706.

Bittner KC, Andrasfalvy BK, Magee JC (2012) Ion channel gradients in the apical tuft region of CA1 pyramidal neurons. *PloS one* 7:e46652.

Bittner T, Fuhrmann M, Burgold S, Ochs SM, Hoffmann N, Mitteregger G, Kretzschmar H, Laferla FM, Herms J (2010) Multiple events lead to dendritic spine loss in triple transgenic Alzheimer's disease mice. *PloS one* 5:e15477.

Bliss TV, Collingridge GL (1993) A synaptic model of memory: long-term potentiation in the hippocampus. *Nature* 361:31–39.

Bliss TV, Lømo T (1973) Long-lasting potentiation of synaptic transmission in the dentate area of the anaesthetized rabbit following stimulation of the perforant path. *The Journal of physiology* 232:331–356.

Bliss TV, Cooke SF (2011) Long-term potentiation and long-term depression: a clinical perspective. *Clinics* 66:3–17.

Bloss EB, Cembrowski MS, Karsh B, Colonell J, Fetter RD, Spruston N (2016) Structured dendritic inhibition supports branch-selective integration in CA1 pyramidal cells. *Neuron* 89:1016–1030.

Bojarski L, Herms J, Kuznicki J (2008) Calcium dysregulation in Alzheimer's disease. *Neurochemistry International* 52:621–633.

Booker SA, De Oliveira LS, Anstey NJ, Kozic Z, Dando OR, Jackson AD, Baxter PS, Isom LL, Sherman DL, Hardingham GE et al. (2020) Input-output relationship of ca1 pyramidal neurons reveals intact homeostatic mechanisms in a mouse model of fragile x syndrome. *Cell Reports* 32:107988.

Born HA, Kim JY, Savjani RR, Das P, Dabaghian YA, Guo Q, Yoo JW, Schuler DR, Cirrito JR, Zheng H, Golde TE, Noebels JL, Jankowsky JL (2014) Genetic suppression of transgenic APP rescues hypersynchronous network activity in a mouse model of Alzheimer's disease. *Journal of Neuroscience* 34:3826–3840.

Borst A, Haag J (1996) The intrinsic electrophysiological characteristics of fly lobula plate tangential cells: I. Passive membrane properties. *Journal of Computational Neuroscience* 3:313–336.

Braak H, Braak E (1991) Neuropathological stageing of Alzheimer-related changes. *Acta Neuropathologica* 82:239–259.

Braak H, Braak E, Bohl J (1993) Staging of Alzheimer-related cortical destruction. *European Neurology* 33:403–408.

Bromer C, Bartol TM, Bowden JB, Hubbard DD, Hanka DC, Gonzalez PV, Kuwajima M, Mendenhall JM, Parker PH, Abraham WC, Sejnowski TJ, Harris KM (2018) Long-term potentiation expands information content of hippocampal dentate gyrus synapses. *Proceedings of the National Academy of Sciences of the United States of America* 115:E2410–E2418.

Brown JT, Chin J, Leiser SC, Pangalos MN, Randall AD (2011) Altered intrinsic neuronal excitability and reduced Na+ currents in a mouse model of Alzheimer's disease. *Neurobiology of Aging* 32:2109.e1–2109.e14.

Buchanan K, Mellor J (2010) The activity requirements for spike timing-dependent plasticity in the hippocampus. *Frontiers in synaptic neuroscience* p. 11.

Buckmaster PS, Wenzel HJ, Kunkel DD, Schwartzkroin PA (1996) Axon arbors and synaptic connections of hippocampal mossy cells in the rat in vivo. *Journal of comparative neurology* 366:270–292.

Burke SN, Turner SM, Desrosiers CL, Johnson SA, Maurer AP (2018) Perforant path fiber loss results in mnemonic discrimination task deficits in young rats. *Frontiers in Systems Neuroscience* 12:61.

Busche M, Eichhoff G, Adelsberger H, Abramowski D, Wiederhold K, Haass C, Staufenbiel M, Konnerth A, Garaschuk O (2008) Clusters of hyperactive neurons near amyloid plaques in a mouse model of Alzheimer's disease. *Science* 321:1686–1689.

Busche MA, Chen X, Henning HA, Reichwald J, Staufenbiel M, Sakmann B, Konnerth A (2012) Critical role of soluble amyloid-β for early hippocampal hyperactivity in a mouse model of Alzheimer's disease. *Proceedings of the National Academy of Sciences of the United States of America* 109:8740–8745.

Busche MA, Grienberger C, Keskin AD, Song B, Neumann U, Staufenbiel M, Förstl H, Konnerth A (2015a) Decreased amyloid-β and increased neuronal hyperactivity by immunotherapy in Alzheimer's models. *Nature Neuroscience* 18:1725–1727.

Busche MA, Kekuš M, Adelsberger H, Noda T, Förstl H, Nelken I, Konnerth A (2015b) Rescue of long-range circuit dysfunction in Alzheimer's disease models. *Nature Neuroscience* 18:1623–1630.

Busche MA, Konnerth A (2015) Neuronal hyperactivity - A key defect in Alzheimer's disease? *BioEssays* 37:624–632.

Busche MA, Konnerth A (2016) Impairments of neural circuit function in Alzheimer's disease. *Philosophical Transactions of the Royal Society B: Biological Sciences* 371:20150429.

Buzsáki G, Tingley D (2018) Space and time: the hippocampus as a sequence generator. *Trends in cognitive sciences* 22:853–869.

Cain SM, Snutch TP (2013) T-type calcium channels in burst-firing, network synchrony, and epilepsy. *Biochimica et Biophysica Acta (BBA) - Biomembranes* 1828:1572–1578.

Cannon J, Miller P (2016) Synaptic and intrinsic homeostasis cooperate to optimize single neuron response properties and tune integrator circuits. *Journal of neurophysiology* 116:2004–2022.

Carnevale NT, Tsai KY, Claiborne BJ, Brown TH (1997) Comparative electrotonic analysis of three classes of rat hippocampal neurons. *Journal of Neurophysiology* 78:703–720.

Carnevale N, Lebeda F (1987) Numerical analysis of electrotonus in multicompartmental neuron models. *Journal of neuroscience methods* 19:69–87.

Chavlis S, Petrantonakis PC, Poirazi P (2017) Dendrites of dentate gyrus granule cells contribute to pattern separation by controlling sparsity. *Hippocampus* 27:89–110.

Chavlis S, Poirazi P (2017) Pattern separation in the hippocampus through the eyes of computational modeling. *Synapse* 71:e21972.

Chen C (2005) beta-Amyloid increases dendritic Ca2+ influx by inhibiting the A-type K+ current in hippocampal CA1 pyramidal neurons. *Biochemical and Biophysical Research Communications* 338:1913–1919.

Chklovskii DB (2000) Optimal sizes of dendritic and axonal arbors in a topographic projection. *Journal of Neurophysiology* 83:2113–2119.

Claiborne BJ, Amaral DG, Cowan WM (1990) Quantitative, three-dimensional analysis of granule cell dendrites in the rat dentate gyrus. *Journal of comparative neurology* 302:206–219.

Clelland C, Choi M, Romberg C, Clemenson Jr G, Fragniere A, Tyers P, Jessberger S, Saksida L, Barker R, Gage F et al. (2009) A functional role for adult hippocampal neurogenesis in spatial pattern separation. *Science* 325:210–213.

Cochran JN, Hall AM, Roberson ED (2014) The dendritic hypothesis for Alzheimer's disease pathophysiology. *Brain Research Bulletin* 103:18–28.

Connors BW, Gutnick MJ (1990) Intrinsic firing patterns of diverse neocortical neurons. *Trends in neurosciences* 13:99–104.

Cook EP, Guest JA, Liang Y, Masse NY, Colbert CM (2007) Dendrite-to-soma input/output function of continuous time-varying signals in hippocampal ca1 pyramidal neurons. *Journal of neurophysiology* 98:2943–2955.

Craig MT, McBain CJ (2015) Fast gamma oscillations are generated intrinsically in CA1 without the involvement of fast-spiking basket cells. *Journal of Neuroscience* 35:3616–3624.

Crotty P, Levy WB (2007) Effects of na+ channel inactivation kinetics on metabolic energy costs of action potentials. *Neurocomputing* 70:1652–1656.

Culmone V, Migliore M (2012) Progressive effect of beta amyloid peptides accumulation on CA1 pyramidal neurons: A model study suggesting possible treatments. *Frontiers in Computational Neuroscience* 6:52.

Cuntz H, Bird AD, Mittag M, Beining M, Schneider M, Mediavilla L, Hoffmann FZ, Deller T, Jedlicka P (2021) A general principle of dendritic constancy: A neuron's size- and shape-invariant excitability. *Neuron* 109:3647–3662.

Cuntz H, Borst A, Segev I (2007) Optimization principles of dendritic structure. *Theoretical Biology and Medical Modelling* 4:1–8.

Cuntz H, Forstner F, Borst A, Häusser M (2010) One rule to grow them all: A general theory of neuronal branching and its practical application. *PLoS Computational Biology* 6:e1000877.

Cuntz H, Forstner F, Borst A, Häusser M (2011) The TREES Toolbox - Probing the basis of axonal and dendritic branching. *Neuroinformatics* 9:91–96.

Cuntz H, Forstner F, Schnell B, Ammer G, Raghu SV, Borst A (2013) Preserving neural function under extreme scaling. *PloS one* 8:1–10.

Cuntz H, Mathy A, Häusser M (2012) A scaling law derived from optimal dendritic wiring. *Proceedings of the National Academy of Sciences* 109:11014–11018.

Cutsuridis V, Graham BP, Cobb S, Vida I (2019) *Hippocampal microcircuits: a computational modeler's resource book* Springer.

Davis GW, Bezprozvanny I (2001) Maintaining the stability of neural function: a homeostatic hypothesis. *Annual review of physiology* 63:847–869.

Dell'Orco JM, Wasserman AH, Chopra R, Ingram MA, Hu YS, Singh V, Wulff H, Opal P, Orr HT, Shakkottai VG (2015) Neuronal atrophy early in degenerative ataxia is a compensatory mechanism to regulate membrane excitability. *Journal of Neuroscience* 35:11292–11307.

Denève S, Alemi A, Bourdoukan R (2017) The brain as an efficient and robust adaptive learner. *Neuron* 94:969–977.

Derdikman D, Knierim JJ et al. (2014) Space, time and memory in the hippocampal formation Technical report, Springer.

Dickerson BC, Salat DH, Greve DN, Chua EF, Rand-Giovannetti E, Rentz DM, Bertram L, Mullin K, Tanzi RE, Blacker D, Albert MS, Sperling RA (2005) Increased hippocampal activation in mild cognitive impairment compared to normal aging and AD. *Neurology* 65:404–411.

Dickstein DL, Brautigam H, Stockton SD, Jr., Schmeidler J, Hof PR (2010) Changes in dendritic complexity and spine morphology in transgenic mice expressing human wild-type tau. *Brain Structure and Function* 214:161.

Doan J, Gardier AM, Tritschler L (2019) Role of adult-born granule cells in the hippocampal functions: Focus on the glun2b-containing nmda receptors. *European Neuropsychopharmacology* 29:1065–1082.

Dongmin Sohn P, Tzu-Ling Huang C, Yan R, Fan L, Tracy TE, Camargo CM, Montgomery KM, Arhar T, Mok SA, Freilich R, Baik J, He M, Gong S, Roberson ED, Karch CM, Gestwicki JE, Xu K, Kosik KS, Gan L, Appel Alzheimer R (2019) Pathogenic tau impairs axon initial segment plasticity and excitability homeostasis. *Neuron* 104:458–470.

Drion G, O'Leary T, Marder E (2015) Ion channel degeneracy enables robust and tunable neuronal firing rates. *Proceedings of the National Academy of Sciences of the United States of America* 112:E5361–E5370.

Duffy ÁM, Morales-Corraliza J, Bermudez-Hernandez KM, Schaner MJ, Magagna-Poveda A, Mathews PM, Scharfman HE (2015) Entorhinal cortical defects in Tg2576 mice are present as early as 2-4months of age. *Neurobiology of Aging* 36:134–148.

Dunn AR, Kaczorowski CC (2019) Regulation of intrinsic excitability: Roles for learning and memory, aging and Alzheimer's disease, and genetic diversity. *Neurobiology of Learning and Memory* 164:107069.

Edelman GM, Gally JA (2001) Degeneracy and complexity in biological systems. *Proceedings of the National Academy of Sciences of the United States of America* 98:13763–13768.

Eichenbaum H (2017) On the integration of space, time, and memory. *Neuron* 95:1007–1018.

Eichenbaum H, Otto T, Cohen NJ (1992) The hippocampus—what does it do? *Behavioral and neural biology* 57:2–36.

Ekstrom AD, Ranganath C (2018) Space, time, and episodic memory: The hippocampus is all over the cognitive map. *Hippocampus* 28:680–687.

Espósito MS, Piatti VC, Laplagne DA, Morgenstern NA, Ferrari CC, Pitossi FJ, Schinder AF (2005) Neuronal differentiation in the adult hippocampus recapitulates embryonic development. *Journal of Neuroscience* 25:10074–10086.

Evans MD, Dumitrescu AS, Kruijssen DL, Taylor SE, Grubb MS (2015) Rapid modulation of axon initial segment length influences repetitive spike firing. *Cell Reports* 13:1233–1245.

Fabel K, Kempermann G (2008) Physical activity and the regulation of neurogenesis in the adult and aging brain. *Neuromolecular medicine* 10:59–66.

Faghihi F, Moustafa AA (2015) A computational model of pattern separation efficiency in the dentate gyrus with implications in schizophrenia. *Frontiers in systems neuroscience* 9:42.

Falke E, Nissanov J, Mitchell TW, Bennett DA, Trojanowski JQ, Arnold SE (2003) Subicular dendritic arborization in Alzheimer's disease correlates with neurofibrillary tangle density. *American Journal of Pathology* 163:1615–1621.

Fardet T, Levina A (2020) Simple models including energy and spike constraints reproduce complex activity patterns and metabolic disruptions. *PLoS Computational Biology* 16:e1008503.

Ferrao Santos S, Pierrot N, Octave JN (2010) Network excitability dysfunction in Alzheimer's disease: Insights from in vitro and in vivo models. *Reviews in the Neurosciences* 21:153–171.

Fiala JC, Spacek J, Harris KM (2002) Dendritic spine pathology: cause or consequence of neurological disorders? *Brain research reviews* 39:29–54.

Frazzini V, Guarnieri S, Bomba M, Navarra R, Morabito C, Mariggiò MA, Sensi SL (2016) Altered Kv2.1 functioning promotes increased excitability in hippocampal neurons of an Alzheimer's disease mouse model. *Cell Death and Disease* 7:e2100–e2100.

Frere S, Slutsky I (2018) Alzheimer's disease: From firing instability to homeostasis network collapse. *Neuron* 97:32–58.

Garden DL, Dodson PD, O'Donnell C, White MD, Nolan MF (2008) Tuning of synaptic integration in the medial entorhinal cortex to the organization of grid cell firing fields. *Neuron* 60:875–889.

Garg J, Lakhani A, Dave V (2021) Effects of the involvement of calcium channels on neuronal hyperexcitability related to Alzheimer's disease: A computational model. *Neurophysiology* 52:334–347.

Ge S, Yang Ch, Hsu Ks, Ming Gl, Song H (2007) A critical period for enhanced synaptic plasticity in newly generated neurons of the adult brain. *Neuron* 54:559–566.

Gervais É, Iloun P, Martianova E, Bessa ACG, Rivest S, Topolnik L (2022) Structural analysis of the microglia–interneuron interactions in the CA1 hippocampal area of the APP/PS1 mouse model of Alzheimer's disease. *Journal of Comparative Neurology* 530:1423–1437.

Geula C, Mesulam MM, Saroff DM, Wu CK (1998) Relationship between plaques, tangles, and loss of cortical cholinergic fibers in Alzheimer disease. *Journal of Neuropathology and Experimental Neurology* 57:63–75.

Ghatak S, Dolatabadi N, Trudler D, Zhang X, Wu Y, Mohata M, Ambasudhan R, Talantova M, Lipton SA (2019) Mechanisms of hyperexcitability in Alzheimer's disease hiPSC-derived neurons and cerebral organoids vs. isogenic control. *Elife* 8:1–22.

Gidon A, Zolnik TA, Fidzinski P, Bolduan F, Papoutsi A, Poirazi P, Holtkamp M, Vida I, Larkum ME (2020) Dendritic action potentials and computation in human layer 2/3 cortical neurons. *Science* 367:83–87.

Gjorgjieva J, Drion G, Marder E (2016) Computational implications of biophysical diversity and multiple timescales in neurons and synapses for circuit performance. *Current opinion in neurobiology* 37:44–52.

Goaillard JM, Marder E (2021) Ion channel degeneracy, variability and covariation in neuron and circuit resilience. *Annual Review of Neuroscience* 44:335–357.

Golding NL, Mickus TJ, Katz Y, Kath WL, Spruston N (2005) Factors mediating powerful voltage attenuation along CA1 pyramidal neuron dendrites. *The Journal of Physiology* 568:69–82.

Golding NL, Staff NP, Spruston N (2002) Dendritic spikes as a mechanism for cooperative long-term potentiation. *Nature* 418:326–331.

Goldstein SS, Rall W (1974) Changes of action potential shape and velocity for changing core conductor geometry. *Biophysical journal* 14:731–757.

Good TA, Smith D, Murphy RM (1996) Beta-amyloid peptide blocks the fast-inactivating K+ current in rat hippocampal neurons. *Biophysical Journal* 70:296–304.

GoodSmith D, Chen X, Wang C, Kim SH, Song H, Burgalossi A, Christian KM, Knierim JJ (2017) Spatial representations of granule cells and mossy cells of the dentate gyrus. *Neuron* 93:677–690.

Gould E, Beylin A, Tanapat P, Reeves A, Shors TJ (1999) Learning enhances adult neurogenesis in the hippocampal formation. *Nature neuroscience* 2:260–265.

Gould E, Tanapat P (1999) Stress and hippocampal neurogenesis. *Biological psychiatry* 46:1472–1479.

Grashow R, Brookings T, Marder E (2010) Compensation for variable intrinsic neuronal excitability by circuit-synaptic interactions. *Journal of Neuroscience* 30:9145–9156.

Graveland GA, Williams RS, DiFiglia M (1985) Evidence for degenerative and regenerative changes in neostriatal spiny neurons in Huntington's disease. *Science* 227:770–773.

Grienberger C, Rochefort NL, Adelsberger H, Henning HA, Hill DN, Reichwald J, Staufenbiel M, Konnerth A (2012) Staged decline of neuronal function in vivo in an animal model of Alzheimer's disease. *Nature Communications* 3:774.

Grutzendler J, Helmin K, Tsai J, Gan WB (2007) Various dendritic abnormalities are associated with fibrillar amyloid deposits in Alzheimer's disease. *Annals of the New York Academy of Sciences* 1097:30–39.

Guzman SJ, Schlögl A, Espinoza C, Zhang X, Suter BA, Jonas P (2021) How connectivity rules and synaptic properties shape the efficacy of pattern separation in the entorhinal cortex–dentate gyrus–ca3 network. *Nature Computational Science* 1:830–842.

Hall AM, Throesch BT, Buckingham SC, Markwardt SJ, Peng Y, Wang Q, Hoffman DA, Roberson ED (2015) Tau-dependent Kv4.2 depletion and dendritic hyperexcitability in a mouse model of Alzheimer's disease. *Journal of Neuroscience* 35:6221–6230.

Halliday G (2017) Pathology and hippocampal atrophy in alzheimer's disease. *The Lancet Neurology* 16:862–864.

Harris JJ, Jolivet R, Attwell D (2012) Synaptic energy use and supply. *Neuron* 75:762–777.

Harris JJ, Jolivet R, Engl E, Attwell D (2015) Energy-efficient information transfer by visual pathway synapses. *Current Biology* 25:3151–3160.

Hasenstaub A, Otte S, Callaway E, Sejnowski TJ (2010) Metabolic cost as a unifying principle governing neuronal biophysics. *Proceedings of the National Academy of Sciences* 107:12329–12334.

Häusser M (2001) Synaptic function: Dendritic democracy. *Current Biology* 11:10–12.

Hay E, Schürmann F, Markram H, Segev I (2013) Preserving axosomatic spiking features despite diverse dendritic morphology. *Journal of neurophysiology* 109:2972–2981.

Hijazi S, Heistek TS, Scheltens P, Neumann U, Shimshek DR, Mansvelder HD, Smit AB, van Kesteren RE (2020) Early restoration of parvalbumin interneuron activity prevents memory loss and network hyperexcitability in a mouse model of Alzheimer's disease. *Molecular Psychiatry* 25:3380–3398.

Hines ML, Carnevale NT (2004) Discrete event simulation in the NEURON environment. *Neurocomputing* 58-60:1117–1122.

Hodgkin AL, Huxley AF (1952) A quantitative description of membrane current and its application to conduction and excitation in nerve. *The Journal of physiology* 117:500.

Hodgkin AL, Huxley AF, Katz B (1952) Measurement of current-voltage relations in the membrane of the giant axon of loligo. *The Journal of physiology* 116:424.

Hodgkin AL, Katz B (1949) The effect of sodium ions on the electrical activity of the giant axon of the squid. *The Journal of physiology* 108:37.

Holtmaat A, Caroni P (2016) Functional and structural underpinnings of neuronal assembly formation in learning. *Nature neuroscience* 19:1553–1562.

Horvath AA, Papp A, Zsuffa J, Szucs A, Luckl J, Radai F, Nagy F, Hidasi Z, Csukly G, Barcs G, Kamondi A (2021) Subclinical epileptiform activity accelerates the progression of alzheimer's disease: A long-term eeg study. *Clinical Neurophysiology* 132:1982–1989.

Inglebert Y, Aljadeff J, Brunel N, Debanne D (2020) Synaptic plasticity rules with physiological calcium levels. *Proceedings of the National Academy of Sciences* 117:33639–33648.

Jaeger BN, Linker SB, Parylak SL, Barron JJ, Gallina IS, Saavedra CD, Fitzpatrick C, Lim CK, Schafer ST, Lacar B et al. (2018) A novel environment-evoked transcriptional signature predicts reactivity in single dentate granule neurons. *Nature communications* 9:3084.

Jaffe DB, Carnevale NT (1999) Passive normalization of synaptic integration influenced by dendritic architecture. *Journal of neurophysiology* 82:3268–3285.

Jamann N, Dannehl D, Lehmann N, Wagener R, Thielemann C, Schultz C, Staiger J, Kole MH, Engelhardt M (2021) Sensory input drives rapid homeostatic scaling of the axon initial segment in mouse barrel cortex. *Nature Communications* 12:23.

Jarrard LE (1995) What does the hippocampus really do? *Behavioural brain research* 71:1–10.

Jarsky T, Roxin A, Kath WL, Spruston N (2005) Conditional dendritic spike propagation following distal synaptic activation of hippocampal CA1 pyramidal neurons. *Nature Neuroscience* 8:1667–1676.

Jedlicka P, Bird AD, Cuntz H (2022) Pareto optimality, economy–effectiveness trade-offs and ion channel degeneracy: improving population modelling for single neurons. *Open Biology* 12:220073.

Jessberger S, Kempermann G (2003) Adult-born hippocampal neurons mature into activity-dependent responsiveness. *European Journal of Neuroscience* 18:2707–2712.

Johnston ST, Shtrahman M, Parylak S, Gonçalves JT, Gage FH (2016) Paradox of pattern separation and adult neurogenesis: A dual role for new neurons balancing memory resolution and robustness. *Neurobiology of learning and memory* 129:60–68.

Jungenitz T, Beining M, Radic T, Deller T, Cuntz H, Jedlicka P, Schwarzacher SW (2018) Structural homo-and heterosynaptic plasticity in mature and adult newborn rat hippocampal granule cells. *Proceedings of the National Academy of Sciences* 115:E4670–E4679.

Kamaleddin MA (2022) Degeneracy in the nervous system: from neuronal excitability to neural coding. *BioEssays* 44:2100148.

Kath WL (2005) Computational modeling of dendrites. *Journal of neurobiology* 64:91–99.

Katz Y, Menon V, Nicholson DA, Geinisman Y, Kath WL, Spruston N (2009) Synapse distribution suggests a two-stage model of dendritic integration in CA1 pyramidal neurons. *Neuron* 63:171–177.

Kazim SF, Chuang SC, Zhao W, Wong RK, Bianchi R, Iqbal K (2017) Early-onset network hyperexcitability in presymptomatic Alzheimer's disease transgenic mice is suppressed by passive immunization with anti-human APP/Aβ antibody and by mGluR5 blockade. *Frontiers in Aging Neuroscience* 9:71.

Kazim SF, Seo JH, Bianchi R, Larson CS, Sharma A, Wong RK, Gorbachev KY, Pereira AC (2021) Neuronal network excitability in Alzheimer's disease: The puzzle of similar versus divergent roles of amyloid β and tau. *eNeuro* 8.

Kee N, Teixeira CM, Wang AH, Frankland PW (2007) Preferential incorporation of adult-generated granule cells into spatial memory networks in the dentate gyrus. *Nature neuroscience* 10:355–362.

Kellner V, Menkes-Caspi N, Beker S, Stern EA (2014) Amyloid-β alters ongoing neuronal activity and excitability in the frontal cortex. *Neurobiology of Aging* 35:1982–1991.

Kempermann G (2002) Why new neurons? possible functions for adult hippocampal neurogenesis. *Journal of neuroscience* 22:635–638.

Kempermann G (2022) What is adult hippocampal neurogenesis good for? *Frontiers in Neuroscience* 16:852680.

Kempermann G, Jessberger S, Steiner B, Kronenberg G (2004) Milestones of neuronal development in the adult hippocampus. *Trends in neurosciences* 27:447–452.

Kempermann G, Song H, Gage FH (2015) Neurogenesis in the adult hippocampus. *Cold Spring Harbor perspectives in biology* 7:a018812.

Kerrigan TL, Brown JT, Randall AD (2014) Characterization of altered intrinsic excitability in hippocampal CA1 pyramidal cells of the Aβ-overproducing PDAPP mouse. *Neuropharmacology* 79:515–524.

Keskin AD, Kekuš M, Adelsberger H, Neumann U, Shimshek DR, Song B, Zott B, Peng T, Förstl H, Staufenbiel M, Nelken I, Sakmann B, Konnerth A, Busche MA (2017) BACE inhibition-dependent repair of Alzheimer's pathophysiology. *Proceedings of the National Academy of Sciences of the United States of America* 114:8631–8636.

Khan UA, Liu L, Provenzano FA, Berman DE, Profaci CP, Sloan R, Mayeux R, Duff KE, Small SA (2013) Molecular drivers and cortical spread of lateral entorhinal cortex dysfunction in preclinical Alzheimer's disease. *Nature Neuroscience* 17:304–311.

Kim DY, Carey BW, Wang H, Ingano LA, Binshtok AM, Wertz MH, Pettingell WH, He P, Lee VM, Woolf CJ, Kovacs DM (2007) BACE1 regulates voltage-gated sodium channels and neuronal activity. *Nature Cell Biology* 9:755–764.

Kim WR, Christian K, Ming GL, Song H (2012) Time-dependent involvement of adult-born dentate granule cells in behavior. *Behavioural brain research* 227:470–479.

Kim Y, Hsu CL, Cembrowski MS, Mensh BD, Spruston N (2015) Dendritic sodium spikes are required for long-term potentiation at distal synapses on hippocampal pyramidal neurons. *Elife* 4:1–30.

Knobloch M, Mansuy IM (2008) Dendritic spine loss and synaptic alterations in Alzheimer's disease. *Molecular Neurobiology* 37:73–82.

Koch C, Segev I (1998) *Methods in neuronal modeling: from ions to networks* MIT press.

Kogan JH, Franklandand PW, Silva AJ (2000) Long-term memory underlying hippocampus-dependent social recognition in mice. *Hippocampus* 10:47–56.

Krichmar JL, Nasuto SJ, Scorcioni R, Washington SD, Ascoli GA (2002) Effects of dendritic morphology on ca3 pyramidal cell electrophysiology: a simulation study. *Brain research* 941:11–28.

Kropff E, Yang SM, Schinder AF (2015) Dynamic role of adult-born dentate granule cells in memory processing. *Current opinion in neurobiology* 35:21–26.

Krueppel R, Remy S, Beck H (2011) Dendritic integration in hippocampal dentate granule cells. *Neuron* 71:512–528.

Kuba H, Adachi R, Ohmori H (2014) Activity-dependent and activity-independent development of the axon initial segment. *Journal of Neuroscience* 34:3443–3453.

Kuhn HG, Dickinson-Anson H, Gage FH (1996) Neurogenesis in the dentate gyrus of the adult rat: age-related decrease of neuronal progenitor proliferation. *Journal of Neuroscience* 16:2027–2033.

Kumar SS, Gänswein T, Buccino AP, Xue X, Bartram J, Emmenegger V, Hierlemann A (2022) Tracking axon initial segment plasticity using high-density microelectrode arrays: A computational study. *Frontiers in neuroinformatics* 16:957255.

Larkum M (2013) A cellular mechanism for cortical associations: an organizing principle for the cerebral cortex. *Trends in neurosciences* 36:141–151.

Larkum ME, Wu J, Duverdin SA, Gidon A (2022) The guide to dendritic spikes of the mammalian cortex in vitro and in vivo. *Neuroscience* 489:15–33.

Larkum ME, Waters J, Sakmann B, Helmchen F (2007) Dendritic spikes in apical dendrites of neocortical layer 2/3 pyramidal neurons. *Journal of Neuroscience* 27:8999–9008.

Laughlin SB, Sejnowski TJ (2003) Communication in neuronal networks. *Science* 301:1870–1874.

Le R, Cruz L, Urbanc B, Knowles RB, Hsiao-Ashe K, Duff K, Irizarry MC, Stanley HE, Hyman BT (2001) Plaque-induced abnormalities in neurite geometry in transgenic models of Alzheimer disease: Implications for neural system disruption. *Journal of Neuropathology and Experimental Neurology* 60:753–758.

Lenz M, Eichler A, Kruse P, Stöhr P, Kleidonas D, Galanis C, Lu H, Vlachos A (2023) Denervated mouse ca1 pyramidal neurons express homeostatic synaptic plasticity following entorhinal cortex lesion. *Frontiers in Molecular Neuroscience* 16:1148219.

León-Espinosa G, DeFelipe J, Muñoz A (2012) Effects of Amyloid-β plaque proximity on the axon initial segment of pyramidal cells. *Journal of Alzheimer's Disease* 29:841–852.

Leuner B, Gould E (2010) Structural plasticity and hippocampal function. *Annual review of psychology* 61:111–140.

Leuner B, Gould E, Shors TJ (2006) Is there a link between adult neurogenesis and learning? *Hippocampus* 16:216–224.

Leutgeb JK, Leutgeb S, Moser MB, Moser EI (2007) Pattern separation in the dentate gyrus and ca3 of the hippocampus. *science* 315:961–966.

Liebscher S, Keller GB, Goltstein PM, Bonhoeffer T, Hübener M (2016) Selective persistence of sensorimotor mismatch signals in visual cortex of behaving Alzheimer's disease mice. *Current Biology* 26:956–964.

Liu C, Tan FCK, Xiao ZC, Dawe GS (2015) Amyloid precursor protein enhances Nav1.6 sodium channel cell surface expression. *Journal of Biological Chemistry* 290:12048–12057.

Lodge M, Bischofberger J (2019) Synaptic properties of newly generated granule cells support sparse coding in the adult hippocampus. *Behavioural brain research* 372:112036.

London M, Häusser M (2005) Dendritic computation. *Annu. Rev. Neurosci.* 28:503–532.

London M, Meunier C, Segev I (1999) Signal transfer in passive dendrites with nonuniform membrane conductance. *Journal of Neuroscience* 19:8219–8233.

López-Madrona VJ, Canals S, Hernández M, Joan D'alacant S (2021) Functional interactions between entorhinal cortical pathways modulate theta activity in the hippocampus. *Biology* 10:692.

Lopez-Rojas J, Kreutz MR (2016) Mature granule cells of the dentate gyrus—passive bystanders or principal performers in hippocampal function? *Neuroscience & Biobehavioral Reviews* 64:167–174.

Lu B, Zhang Q, Wang H, Wang Y, Nakayama M, Ren D (2010) Extracellular calcium controls background current and neuronal excitability via an unc79-unc80-nalcn cation channel complex. *Neuron* 68:488–499.

Madar AD, Ewell LA, Jones MV (2019) Pattern separation of spiketrains in hippocampal neurons. *Scientific Reports* 9:5282.

Madroñal N, Delgado-García JM, Fernández-Guizán A, Chatterjee J, Köhn M, Mattucci C, Jain A, Tsetsenis T, Illarionova A, Grinevich V et al. (2016) Rapid erasure of hippocampal memory following inhibition of dentate gyrus granule cells. *Nature communications* 7:10923.

Maestú F, de Haan W, Busche MA, DeFelipe J (2021) Neuronal excitation/inhibition imbalance: core element of a translational perspective on Alzheimer pathophysiology. *Ageing Research Reviews* 69:101372.

Magarin A, McEwen B et al. (1995) Stress-induced atrophy of apical dendrites of hippocampal ca3c neurons: involvement of glucocorticoid secretion and excitatory amino acid receptors. *Neuroscience* 69:89–98.

Magee JC, Cook EP (2000) Somatic EPSP amplitude is independent of synapse location in hippocampal pyramidal neurons. *Nature Neuroscience* 3:895–903.

Magee JC, Grienberger C (2020) Synaptic plasticity forms and functions. *Annual review of neuroscience* 43:95–117.

Maia LF, Kaeser SA, Reichwald J, Hruscha M, Martus P, Staufenbiel M, Jucker M (2013) Changes in amyloid-β and tau in the cerebrospinal fluid of transgenic mice overexpressing amyloid precursor protein. *Science translational medicine* 5:194re2–194re2.

Maier FC, Wehrl HF, Schmid AM, Mannheim JG, Wiehr S, Lerdkrai C, Calaminus C, Stahlschmidt A, Ye L, Burnet M, Stiller D, Sabri O, Reischl G, Staufenbiel M, Garaschuk O, Jucker M, Pichler BJ (2014) Longitudinal PET-MRI reveals β-amyloid deposition and rCBF dynamics and connects vascular amyloidosis to quantitative loss of perfusion. *Nature Medicine* 20:1485–1492.

Major G, Larkum ME, Schiller J (2013) Active properties of neocortical pyramidal neuron dendrites. *Annual review of neuroscience* 36:1–24.

Mallot HA (2013) *Computational neuroscience*, Vol. 486 Springer.

Manns JR, Zilli EA, Ong KC, Hasselmo ME, Eichenbaum H (2007) Hippocampal CA1 spiking during encoding and retrieval: Relation to theta phase. *Neurobiology of Learning and Memory* 87:9–20.

Marder E, Goaillard JM (2006) Variability, compensation and homeostasis in neuron and network function. *Nature Reviews Neuroscience* 7:563–574.

Marr D (1969) A theory of cerebellar cortex. *Journal of Physiology* pp. 437–470.

Martin SJ, Grimwood PD, Morris RG (2000) Synaptic plasticity and memory: an evaluation of the hypothesis. *Annual review of neuroscience* 23:649–711.

Masland RH (2004) Neuronal cell types. *Current Biology* 14:R497–R500.

Masliah E, Mallory M, Hansen L, DeTeresa R, Alford M, Terry R (1994) Synaptic and neuritic alterations during the progression of Alzheimer's disease. *Neuroscience Letters* 174:67–72.

McDougal RA, Morse TM, Carnevale T, Marenco L, Wang R, Migliore M, Miller PL, Shepherd GM, Hines ML (2017) Twenty years of ModelDB and beyond: Building essential modeling tools for the future of neuroscience. *Journal of Computational Neuroscience* 42:1.

McKenna TM, Davis JL, Zornetzer SF (2014) *Single neuron computation* Academic Press.

Medlock L, Sekiguchi K, Hong S, Dura-Bernal S, Lytton WW, Prescott SA (2022) Multiscale computer model of the spinal dorsal horn reveals changes in network processing associated with chronic pain. *Journal of Neuroscience* 42:3133–3149.

Medlock L, Shute L, Fry M, Standage D, Ferguson AV (2018) Ionic mechanisms underlying tonic and burst firing behavior in subfornical organ neurons: A combined experimental and modeling study. *Journal of Neurophysiology* 120:2269–2281.

Megías M, Emri Z, Freund TF, Gulyás AI (2001) Total number and distribution of inhibitory and excitatory synapses on hippocampal CA1 pyramidal cells. *Neuroscience* 102:527–540.

Meinertzhagen IA, Takemura Sy, Meinertzhagen IA, Takemura Sy, Lu Z, Huang S, Gao S, Ting CY, Lee CH (2009) From form to function: the ways to know a neuron. *Journal of Neurogenetics* 23:68–77.

Melgosa-Ecenarro L, Doostdar N, Radulescu CI, Jackson JS, Barnes SJ (2022) Pinpointing the locus of GABAergic vulnerability in Alzheimer's disease In *Seminars in Cell & Developmental Biology*. Elsevier.

Merino-Serrais P, Benavides-Piccione R, Blazquez-Llorca L, Kastanauskaite A, Rábano A, Avila J, Defelipe J (2013) The influence of phospho-tau on dendritic spines of cortical pyramidal neurons in patients with Alzheimer's disease. *Brain* 136:1913–1928.

Miettinen TP, Björklund M (2017) Mitochondrial function and cell size: an allometric relationship. *Trends in cell biology* 27:393–402.

Minkeviciene R, Rheims S, Dobszay MB, Zilberter M, Hartikainen J, Fülöp L, Penke B, Zilberter Y, Harkany T, Pitkänen A, Tanila H (2009) Amyloid β-induced neuronal hyperexcitability triggers progressive epilepsy. *Journal of Neuroscience* 29:3453–3462.

Mitchell SJ, Silver RA (2003) Shunting inhibition modulates neuronal gain during synaptic excitation. *Neuron* 38:433–445.

Mittag M, Mediavilla L, Remy S, Cuntz H, Jedlicka P (2023) Modelling the contributions to hyperexcitability in a mouse model of Alzheimer's disease. *The Journal of Physiology* pp. 1–35.

Mongiat LA, Espósito MS, Lombardi G, Schinder AF (2009) Reliable activation of immature neurons in the adult hippocampus. *PloS one* 4:e5320.

Moolman DL, Vitolo OV, Vonsattel JPG, Shelanski ML (2004) Dendrite and dendritic spine alterations in Alzheimer models. *Journal of Neurocytology* 33:377–387.

Moreno-Jiménez EP, Flor-García M, Terreros-Roncal J, Rábano A, Cafini F, Pallas-Bazarra N, Ávila J, Llorens-Martín M (2019) Adult hippocampal neurogenesis is abundant in neurologically healthy subjects and drops sharply in patients with alzheimer's disease. *Nature medicine* 25:554–560.

Morrison A, Diesmann M, Gerstner W (2008) Phenomenological models of synaptic plasticity based on spike timing. *Biological cybernetics* 98:459–478.

Morse TM, Carnevale NT, Mutalik PG, Migliore M, Shepherd GM (2010) Abnormal excitability of oblique dendrites implicated in early Alzheimer's: A computational study. *Frontiers in Neural Circuits* 4:16.

Moser MB, Rowland DC, Moser EI (2015) Place cells, grid cells, and memory. *Cold Spring Harbor perspectives in biology* 7:a021808.

Moujahid A, d'Anjou A (2012) Metabolic efficiency with fast spiking in the squid axon. *Frontiers in Computational Neuroscience* 6:95.

Müller L, Kirschstein T, Köhling R, Kuhla A, Teipel S (2021) Neuronal hyperexcitability in APPSWE/PS1dE9 mouse models of Alzheimer's disease. *Journal of Alzheimer's disease* 81:855–869.

Müller-Komorowska D, Kuru B, Beck H, Braganza O (2023) Phase information is conserved in sparse, synchronous population-rate-codes via phase-to-rate recoding. *Nature Communications* 14:6106.

Musial TF, Molina-Campos E, Bean LA, Ybarra N, Borenstein R, Russo ML, Buss EW, Justus D, Neuman KM, Ayala GD, Mullen SA, Voskobiynyk Y, Tulisiak CT, Fels JA, Corbett NJ, Carballo G, Kennedy CD, Popovic J, Ramos-Franco J, Fill M, Pergande MR, Borgia JA, Corbett GT, Pahan K, Han Y, Chetkovich DM, Vassar RJ, Byrne RW, Matthew Oh M, Stoub TR, Remy S, Disterhoft JF, Nicholson DA (2018) Store depletion-induced h-channel plasticity rescues a channelopathy linked to Alzheimer's disease. *Neurobiology of Learning and Memory* 154:141–157.

Nakashiba T, Cushman JD, Pelkey KA, Renaudineau S, Buhl DL, McHugh TJ, Barrera VR, Chittajallu R, Iwamoto KS, McBain CJ et al. (2012) Young dentate granule cells mediate pattern separation, whereas old granule cells facilitate pattern completion. *Cell* 149:188–201.

Nelson PC, Radosavljević M, Bromberg S, Goodsell DS (2008) *Biological physics: energy, information, life* Number QH505 N44. WH Freeman New York.

Neuman KM, Molina-Campos E, Musial TF, Price AL, Oh KJ, Wolke ML, Buss EW, Scheff SW, Mufson EJ, Nicholson DA (2015) Evidence for Alzheimer's disease-linked synapse loss and compensation in mouse and human hippocampal CA1 pyramidal neurons. *Brain Structure and Function* 220:3143.

Neunuebel JP, Knierim JJ (2014) Ca3 retrieves coherent representations from degraded input: direct evidence for ca3 pattern completion and dentate gyrus pattern separation. *Neuron* 81:416–427.

Neves G, Cooke SF, Bliss TV (2008) Synaptic plasticity, memory and the hippocampus: a neural network approach to causality. *Nature Reviews Neuroscience* 9:65–75.

Neymotin SA, Dura-Bernal S, Lakatos P, Sanger TD, Lytton WW (2016) Multitarget multiscale simulation for pharmacological treatment of dystonia in motor cortex. *Frontiers in Pharmacology* 7:157.

Niday Z, Bean BP (2021) BK channel regulation of afterpotentials and burst firing in cerebellar purkinje neurons. *Journal of Neuroscience* 41:2854–2869.

Niemeyer N, Schleimer JH, Schreiber S (2021) Biophysical models of intrinsic homeostasis: Firing rates and beyond. *Current Opinion in Neurobiology* 70:81–88.

Niven JE (2016) Neuronal energy consumption: biophysics, efficiency and evolution. *Current opinion in neurobiology* 41:129–135.

Noebels J (2011) A perfect storm: Converging paths of epilepsy and Alzheimer's dementia intersect in the hippocampal formation. *Epilepsia* 52:39–46.

Okuhara DY, Beck SG (1998) Corticosteroids influence the action potential firing pattern of hippocampal subfield CA3 pyramidal cells. *Neuroendocrinology* 67:58–66.

Olah VJ, Goettemoeller AM, Rayaprolu S, Dammer EB, Seyfried NT, Rangaraju S, Dimidschstein J, Rowan MJ (2022) Biophysical kv3 channel alterations dampen excitability of cortical pv interneurons and contribute to network hyperexcitability in early alzheimer's. *Elife* 11:e75316.

O'Leary T (2018) Homeostasis, failure of homeostasis and degenerate ion channel regulation. *Current Opinion in Physiology* 2:129–138.

Olton DS, Becker JT, Handelmann GE (1979) Hippocampus, space, and memory. *Behavioral and Brain sciences* 2:313–322.

Onasch S, Gjorgjieva J (2020) Circuit stability to perturbations reveals hidden variability in the balance of intrinsic and synaptic conductances. *Journal of Neuroscience* 40:3186–3202.

Opitz B (2014) Memory function and the hippocampus. *The hippocampus in clinical neuroscience* 34:51–59.

Pallasdies F, Norton P, Schleimer JH, Schreiber S (2021) Neural optimization: Understanding trade-offs with pareto theory. *Current Opinion in Neurobiology* 71:84–91.

Palop JJ, Chin J, Roberson ED, Wang J, Thwin MT, Bien-Ly N, Yoo J, Ho KO, Yu GQ, Kreitzer A, Finkbeiner S, Noebels JL, Mucke L (2007) Aberrant excitatory neuronal activity and compensatory remodeling of inhibitory hippocampal circuits in mouse models of Alzheimer's disease. *Neuron* 55:697–711.

Palop JJ, Mucke L (2009) Epilepsy and cognitive impairments in Alzheimer disease. *Archives of Neurology* 66:435–440.

Palop JJ, Mucke L (2016) Network abnormalities and interneuron dysfunction in Alzheimer disease. *Nature Reviews Neuroscience* 17:777–792.

Parent JM, Timothy WY, Leibowitz RT, Geschwind DH, Sloviter RS, Lowenstein DH (1997) Dentate granule cell neurogenesis is increased by seizures and contributes to aberrant network reorganization in the adult rat hippocampus. *Journal of Neuroscience* 17:3727–3738.

Paton JJ, Buonomano DV (2018) The neural basis of timing: distributed mechanisms for diverse functions. *Neuron* 98:687–705.

Payeur A, Béïque JC, Naud R (2019) Classes of dendritic information processing. *Current opinion in neurobiology* 58:78–85.

Perera TD, Lu D, Thirumangalakudi L, Smith EL, Yaretskiy A, Rosenblum LA, Kral JG, Coplan JD et al. (2011) Correlations between hippocampal neurogenesis and metabolic indices in adult nonhuman primates. *Neural plasticity* 2011.

Petrache AL, Rajulawalla A, Shi A, Wetzel A, Saito T, Saido TC, Harvey K, Ali AB (2019) Aberrant excitatory-inhibitory synaptic mechanisms in entorhinal cortex microcircuits during the pathogenesis of Alzheimer's disease. *Cerebral Cortex* 29:1834–1850.

Platschek S, Cuntz H, Deller T, Jedlicka P (2017) Lesion-induced dendritic remodeling as a new mechanism of homeostatic structural plasticity in the adult brain. *The Rewiring Brain* pp. 203–218.

Platschek S, Cuntz H, Vuksic M, Deller T, Jedlicka P (2016) A general homeostatic principle following lesion induced dendritic remodeling. *Acta Neuropathologica Communications* 4:19.

Poirazi P, Brannon T, Mel BW (2003a) Arithmetic of subthreshold synaptic summation in a model CA1 pyramidal cell. *Neuron* 37:977–987.

Poirazi P, Brannon T, Mel BW (2003b) Pyramidal neuron as two-layer neural network. *Neuron* 37:989–999.

Poirazi P, Papoutsi A (2020) Illuminating dendritic function with computational models. *Nature Reviews Neuroscience* 21:303–321.

Post RL, Jolly PC (1957) The linkage of sodium, potassium, and ammonium active transport across the human erythrocyte membrane. *Biochimica et biophysica acta* 25:118–128.

Pothmann L, Klos C, Braganza O, Schmidt S, Horno O, Memmesheimer RM, Beck H (2019) Altered dynamics of canonical feedback inhibition predicts increased burst transmission in chronic epilepsy. *Journal of Neuroscience* 39:8998–9012.

Pouille F, Scanziani M (2004) Routing of spike series by dynamic circuits in the hippocampus. *Nature* 429:717–723.

Pravettoni E, Bacci A, Coco S, Forbicini P, Matteoli M, Verderio C (2000) Different localizations and functions of l-type and n-type calcium channels during development of hippocampal neurons. *Developmental biology* 227:581–594.

Pyapali GK, Sik A, Penttonen M, Buzsaki G, Turner DA (1998) Dendritic properties of hippocampal CA1 pyramidal neurons in the rat: intracellular staining in vivo and in vitro. *Journal of Comparative Neurology* 391:335–352.

Quintanilla J, Jia Y, Lauterborn JC, Pruess BS, Le AA, Cox CD, Gall CM, Lynch G, Gunn BG (2022) Novel types of frequency filtering in the lateral perforant path projections to dentate gyrus. *The Journal of Physiology* 600:3865–3896.

Quintela-López T, Shiina H, Attwell D (2022) Neuronal energy use and brain evolution. *Current Biology* 32:R650–R655.

Rall W (1959) Branching dendritic trees and motoneuron membrane resistivity. *Experimental neurology* 1:491–527.

Rall W (1962) Electrophysiology of a dendritic neuron model. *Biophysical journal* 2:145.

Rall W (1964) Theoretical significance of dendritic trees for neuronal input-output relations. *Neural theory and modeling* .

Rall W, Burke R, Smith T, Nelson PG, Frank K (1967) Dendritic location of synapses and possible mechanisms for the monosynaptic epsp in motoneurons. *Journal of neurophysiology* 30:1169–1193.

Rall W, Rinzel J (1973) Branch input resistance and steady attenuation for input to one branch of a dendritic neuron model. *Biophysical Journal* 13:648–687.

Ranasinghe KG, Kudo K, Hinkley L, Beagle A, Lerner H, Mizuiri D, Findlay A, Miller BL, Kramer JH, Gorno-Tempini ML et al. (2022) Neuronal synchrony abnormalities associated with subclinical epileptiform activity in early-onset alzheimer's disease. *Brain* 145:744–753.

Rao YL, Ganaraja B, Murlimanju B, Joy T, Krishnamurthy A, Agrawal A (2022) Hippocampus and its involvement in alzheimer's disease: a review. *3 Biotech* 12:55.

Ratté S, Prescott SA (2016) Afferent hyperexcitability in neuropathic pain and the inconvenient truth about its degeneracy. *Current Opinion in Neurobiology* 36:31–37.

Ratté S, Zhu Y, Lee KY, Prescott SA (2014) Criticality and degeneracy in injury-induced changes in primary afferent excitability and the implications for neuropathic pain. *Elife* 3:e02370.

Remme MW, Rinzel J, Schreiber S (2018) Function and energy consumption constrain neuronal biophysics in a canonical computation: Coincidence detection. *PLoS computational biology* 14:e1006612.

Rich S, Chameh HM, Lefebvre J, Valiante TA (2022) Loss of neuronal heterogeneity in epileptogenic human tissue impairs network resilience to sudden changes in synchrony. *Cell Reports* 39:110863.

Rinzel J, Rall W (1974) Transient response in a dendritic neuron model for current injected at one branch. *Biophysical journal* 14:759–790.

Roberson ED, Halabisky B, Yoo JW, Yao J, Chin J, Yan F, Wu T, Hamto P, Devidze N, Yu GQ, Palop JJ, Noebels JL, Mucke L (2011) Amyloid-β/Fyn - induced synaptic, network, and cognitive impairments depend on tau levels in multiple mouse models of Alzheimer's disease. *Journal of Neuroscience* 31:700–711.

Rocher AB, Kinson MS, Luebke JI (2008) Significant structural but not physiological changes in cortical neurons of 12-month-old Tg2576 mice. *Neurobiology of Disease* 32:309.

Roddy DW, Farrell C, Doolin K, Roman E, Tozzi L, Frodl T, O'Keane V, O'Hanlon E (2019) The hippocampus in depression: more than the sum of its parts? advanced hippocampal substructure segmentation in depression. *Biological Psychiatry* 85:487–497.

Rodrigues YE, Da J, Freitas S (2017) CA1 and CA3 pyramidal cell morphologies under Alzheimer's disease amyloid beta interaction. *bioRxiv* p. 187476.

Rolls ET (2013) The mechanisms for pattern completion and pattern separation in the hippocampus. *Frontiers in systems neuroscience* 7:74.

Rowan MJ, Klyubin I, Cullen WK, Anwyl R (2003) Synaptic plasticity in animal models of early Alzheimer's disease. *Philosophical Transactions of the Royal Society of London. Series B: Biological Sciences* 358:821–828.

Rudinskiy N, Hawkes JM, Betensky RA, Eguchi M, Yamaguchi S, Spires-Jones TL, Hyman BT (2012) Orchestrated experience-driven arc responses are disrupted in a mouse model of Alzheimer's disease. *Nature Neuroscience* 15:1422–1429.

Ruiter M, Herstel LJ, Wierenga CJ (2020) Reduction of dendritic inhibition in CA1 pyramidal neurons in amyloidosis models of early Alzheimer's disease. *Journal of Alzheimer's Disease* 78:951–964.

Sahay A, Scobie KN, Hill AS, O'Carroll CM, Kheirbek MA, Burghardt NS, Fenton AA, Dranovsky A, Hen R (2011) Increasing adult hippocampal neurogenesis is sufficient to improve pattern separation. *Nature* 472:466–470.

Sakurai A, Tamvacakis AN, Katz PS (2014) Hidden synaptic differences in a neural circuit underlie differential behavioral susceptibility to a neural injury. *Elife* 3:e02598.

Sanabria ER, Su H, Yaari Y (2001) Initiation of network bursts by Ca2+-dependent intrinsic bursting in the rat pilocarpine model of temporal lobe epilepsy. *Journal of Physiology* 532:205–216.

Santoro A (2013) Reassessing pattern separation in the dentate gyrus.

Scala F, Fusco S, Ripoli C, Piacentini R, Li Puma DD, Spinelli M, Laezza F, Grassi C, D'Ascenzo M (2015) Intraneuronal Aβ accumulation induces hippocampal neuron hyperexcitability through A-type K+ current inhibition mediated by activation of caspases and GSK-3. *Neurobiology of Aging* 36:886–900.

Scheibel AB (1979) The hippocampus: Organizational patterns in health and senescence. *Mechanisms of Ageing and Development* 9:89–102.

Schimanski L, Nguyen P (2004) Multidisciplinary approaches for investigating the mechanisms of hippocampus-dependent memory: a focus on inbred mouse strains. *Neuroscience & Biobehavioral Reviews* 28:463–483.

Schmid LC, Mittag M, Poll S, Steffen J, Wagner J, Geis HR, Schwarz I, Schmidt B, Schwarz MK, Remy S, Fuhrmann M (2016) Dysfunction of somatostatin-positive interneurons associated with memory deficits in an Alzheimer's disease model. *Neuron* 92:114–125.

Schmidt B, Marrone DF, Markus EJ (2012) Disambiguating the similar: the dentate gyrus and pattern separation. *Behavioural brain research* 226:56–65.

Schmidt-Hieber C, Bischofberger J (2010) Fast sodium channel gating supports localized and efficient axonal action potential initiation. *Journal of Neuroscience* 30:10233–10242.

Schmidt-Hieber C, Jonas P, Bischofberger J (2004) Enhanced synaptic plasticity in newly generated granule cells of the adult hippocampus. *Nature* 429:184–187.

Schmidt-Hieber C, Jonas P, Bischofberger J (2007) Subthreshold dendritic signal processing and coincidence detection in dentate gyrus granule cells. *Journal of Neuroscience* 27:8430–8441.

Schneider M, Bird AD, Gidon A, Triesch J, Jedlicka P, Cuntz H (2023) Biological complexity facilitates tuning of the neuronal parameter space. *PLOS Computational Biology* 19:e1011212.

Schreiber S, Fellous JM, Tiesinga P, Sejnowski TJ (2004) Influence of ionic conductances on spike timing reliability of cortical neurons for suprathreshold rhythmic inputs. *Journal of neurophysiology* 91:194–205.

Scimemi A, Meabon JS, Woltjer RL, Sullivan JM, Diamond JS, Cook DG (2013) Amyloid-β1-42 slows clearance of synaptically released glutamate by mislocalizing astrocytic GLT-1. *Annals of Internal Medicine* 158:5312–5318.

Segev I, London M (2000) Untangling dendrites with quantitative models. *Science* 290:744–750.

Segev I, Rall W (1988) Computational study of an excitable dendritic spine. *Journal of neurophysiology* 60:499–523.

Selkoe DJ (2019) Early network dysfunction in Alzheimer's disease. *Science* 365:540–541.

Sengupta B, Stemmler M, Laughlin SB, Niven JE (2010) Action potential energy efficiency varies among neuron types in vertebrates and invertebrates. *PLoS computational biology* 6:e1000840.

Shankar GM, Li S, Mehta TH, Garcia-Munoz A, Shepardson NE, Smith I, Brett FM, Farrell MA, Rowan MJ, Lemere CA, Regan CM, Walsh DM, Sabatini BL, Selkoe DJ (2008) Amyloid-β protein dimers isolated directly from Alzheimer's brains impair synaptic plasticity and memory. *Nature Medicine* 14:837–842.

Shannon CE (1948) A mathematical theory of communication. *The Bell system technical journal* 27:379–423.

Sheftel H, Shoval O, Mayo A, Alon U (2013) The geometry of the p areto front in biological phenotype space. *Ecology and evolution* 3:1471–1483.

Sheline YI, Wang PW, Gado MH, Csernansky JG, Vannier MW (1996) Hippocampal atrophy in recurrent major depression. *Proceedings of the National Academy of Sciences* 93:3908–3913.

Shinomoto S, Kim H, Shimokawa T, Matsuno N, Funahashi S, Shima K, Fujita I, Tamura H, Doi T, Kawano K et al. (2009) Relating neuronal firing patterns to functional differentiation of cerebral cortex. *PLoS computational biology* 5:e1000433.

Shoval O, Sheftel H, Shinar G, Hart Y, Ramote O, Mayo A, Dekel E, Kavanagh K, Alon U (2012) Evolutionary trade-offs, pareto optimality, and the geometry of phenotype space. *Science* 336:1157–1160.

Silver RA (2010) Neuronal arithmetic. *Nature Reviews Neuroscience* 11:474–489.

Šišková Z, Justus D, Kaneko H, Friedrichs D, Henneberg N, Beutel T, Pitsch J, Schoch S, Becker A, von der Kammer H, Remy S (2014) Dendritic structural degeneration is functionally linked to cellular hyperexcitability in a mouse model of Alzheimer's disease. *Neuron* 84:1023–1033.

Snyder JS, Soumier A, Brewer M, Pickel J, Cameron HA (2011) Adult hippocampal neurogenesis buffers stress responses and depressive behaviour. *Nature* 476:458–461.

Snyder J, Kee N, Wojtowicz J (2001) Effects of adult neurogenesis on synaptic plasticity in the rat dentate gyrus. *Journal of neurophysiology* 85:2423–2431.

Somogyi A, Katonai Z, Alpár A, Wolf E (2016) A novel form of compensation in the Tg2576 amyloid mouse model of Alzheimer's disease. *Frontiers in Cellular Neuroscience* 0:152.

Sosulina L, Mittag M, Geis HR, Hoffmann K, Klyubin I, Qi Y, Steffen J, Friedrichs D, Henneberg N, Fuhrmann F, Justus D, Keppler K, Cuello AC, Rowan MJ, Fuhrmann M, Remy S (2021) Hippocampal hyperactivity in a rat model of Alzheimer's disease. *Journal of Neurochemistry* 157:2128–2144.

Sparks F, Liao Z, Li W, Grosmark A, Soltesz I, Losonczy A (2020) Hippocampal adult-born granule cells drive network activity in a mouse model of chronic temporal lobe epilepsy. *Nature communications* 11:6138.

Spires TL, Hyman BT (2004) Neuronal structure is altered by amyloid plaques. *Reviews in the Neurosciences* 15:267–278.

Spires-Jones TL, Meyer-Luehmann M, Osetek JD, Jones PB, Stern EA, Bacskai BJ, Hyman BT (2007) Impaired spine stability underlies plaque-related spine loss in an Alzheimer's disease mouse model. *The American Journal of Pathology* 171:1304–1311.

Stemmler M, Koch C (1999) How voltage-dependent conductances can adapt to maximize the information encoded by neuronal firing rate. *Nature neuroscience* 2:521–527.

Stemmler M, Sengupta B, Laughlin S, Niven J (2011) Energetically optimal action potentials. *Advances in neural information processing systems* 24.

Steward O, Vinsant SL, Davis L (1988) The process of reinnervation in the dentate gyrus of adult rats: an ultrastructural study of changes in presynaptic terminals as a result of sprouting. *Journal of Comparative Neurology* 267:203–210.

Stöber TM, Batulin D, Triesch J, Narayanan R, Jedlicka P (2023) Degeneracy in epilepsy: multiple routes to hyperexcitable brain circuits and their repair. *Communications Biology* 6:479.

Stone JV (2018) Principles of neural information theory. *Computational Neuroscience and Metabolic Efficiency* .

Strüber M, Sauer JF, Jonas P, Bartos M (2017) Distance-dependent inhibition facilitates focality of gamma oscillations in the dentate gyrus. *Nature Communications* 8:1–15.

Sun X, Wu Y, Gu M, Liu Z, Ma Y, Li J, Zhang Y (2014) Selective filtering defect at the axon initial segment in Alzheimer's disease mouse models. *Proceedings of the National Academy of Sciences* 111:14271–14276.

Świetlik D, Białowas J, Moryś J, Kusiak A (2019) Computer model of synapse loss during an Alzheimer's disease-like pathology in hippocampal subregions DG, CA3 and CA1 - The way to chaos and information transfer. *Entropy* 21:408.

Szekely P, Sheftel H, Mayo A, Alon U (2013) Evolutionary tradeoffs between economy and effectiveness in biological homeostasis systems. *PLoS computational biology* 9:e1003163.

Szot P, White SS, Greenup JL, Leverenz JB, Peskind ER, Raskind MA (2006) Compensatory changes in the noradrenergic nervous system in the locus ceruleus and hippocampus of postmortem subjects with alzheimer's disease and dementia with lewy bodies. *Journal of Neuroscience* 26:467–478.

Takahashi H, Magee JC (2009) Pathway interactions and synaptic plasticity in the dendritic tuft regions of CA1 pyramidal neurons. *Neuron* 62:102–111.

Takahashi H, Brasnjevic I, Rutten BP, Van Der Kolk N, Perl DP, Bouras C, Steinbusch HW, Schmitz C, Hof PR, Dickstein DL (2010) Hippocampal interneuron loss in an APP/PS1 double mutant mouse and in Alzheimer's disease. *Brain Structure and Function* 214:145–160.

Tan Y, Deng Y, Qing H (2012) Calcium channel blockers and Alzheimer's disease. *Neural Regeneration Research* 7:137–140.

Targa Dias Anastacio H, Matosin N, Ooi L (2022) Neuronal hyperexcitability in Alzheimer's disease: what are the drivers behind this aberrant phenotype? *Translational Psychiatry* 12:1–14.

Teeter CM, Stevens CF (2011) A general principle of neural arbor branch density. *Current Biology* 21:2105–2108.

Terry RD, Masliah E, Salmon DP, Butters N, DeTeresa R, Hill R, Hansen LA, Katzman R (1991) Physical basis of cognitive alterations in Alzheimer's disease: synapse loss is the major correlate of cognitive impairment. *Annals of Neurology* 30:572–580.

Theodore W, Bhatia S, Hatta J, Fazilat S, DeCarli C, Bookheimer S, Gaillard W (1999) Hippocampal atrophy, epilepsy duration, and febrile seizures in patients with partial seizures. *Neurology* 52:132–132.

Tonegawa S, Liu X, Ramirez S, Redondo R (2015) Memory engram cells have come of age. *Neuron* 87:918–931.

Tononi G, Sporns O, Edelman GM (1999) Measures of degeneracy and redundancy in biological networks. *Proceedings of the National Academy of Sciences* 96:3257–3262.

Trinchese F, Liu S, Battaglia F, Walter S, Mathews PM, Arancio O (2004) Progressive age-related development of alzheimer-like pathology in app/ps1 mice. *Annals of Neurology: Official Journal of the American Neurological Association and the Child Neurology Society* 55:801–814.

Tripodi M, Evers JF, Mauss A, Bate M, Landgraf M (2008) Structural homeostasis: Compensatory adjustments of dendritic arbor geometry in response to variations of synaptic input. *PLoS Biology* 6:2172–2187.

Trommald M, Jensen V, Andersen P (1995) Analysis of dendritic spines in rat CA1 pyramidal cells intracellularly filled with a fluorescent dye. *Journal of Comparative Neurology* 353:260–274.

Tsai J, Grutzendler J, Duff K, Gan WB (2004) Fibrillar amyloid deposition leads to local synaptic abnormalities and breakage of neuronal branches. *Nature Neuroscience* 7:1181–1183.

Tuncdemir SN, Lacefield CO, Hen R (2019) Contributions of adult neurogenesis to dentate gyrus network activity and computations. *Behavioural Brain Research* 374:112112.

Turrigiano GG, Nelson SB (2004) Homeostatic plasticity in the developing nervous system. *Nature reviews neuroscience* 5:97–107.

van Elburg RA, van Ooyen A (2010) Impact of dendritic size and dendritic topology on burst firing in pyramidal cells. *PLoS Computational Biology* 6:1–19.

Van Geit W, De Schutter E, Achard P (2008) Automated neuron model optimization techniques: a review. *Biological cybernetics* 99:241–251.

Van Ooyen A, Duijnhouwer J, Remme MW, van Pelt J (2002) The effect of dendritic topology on firing patterns in model neurons. *Network: Computation in Neural Systems* 13:311.

Van Praag H, Christie BR, Sejnowski TJ, Gage FH (1999) Running enhances neurogenesis, learning, and long-term potentiation in mice. *Proceedings of the National Academy of Sciences* 96:13427–13431.

Vergara RC, Jaramillo-Riveri S, Luarte A, Moënne-Loccoz C, Fuentes R, Couve A, Maldonado PE (2019) The energy homeostasis principle: neuronal energy regulation drives local network dynamics generating behavior. *Frontiers in computational neuroscience* p. 49.

Verret L, Mann EO, Hang GB, Barth AM, Cobos I, Ho K, Devidze N, Masliah E, Kreitzer AC, Mody I, Mucke L, Palop JJ (2012) Inhibitory interneuron deficit links altered network activity and cognitive dysfunction in Alzheimer model. *Cell* 149:708–721.

Vetter P, Roth A, Haäusser M (2001) Propagation of action potentials in dendrites depends on dendritic morphology. *Journal of neurophysiology* 85:926–937.

Vineyard CM, Verzi SJ, James CD, Aimone JB (2016) Quantifying neural information content: A case study of the impact of hippocampal adult neurogenesis In *2016 International Joint Conference on Neural Networks (IJCNN)*, pp. 5181–5188. IEEE.

Vitale P, Salgueiro-Pereira AR, Lupascu CA, Willem M, Migliore R, Migliore M, Marie H (2021) Analysis of age-dependent alterations in excitability properties of CA1 pyramidal neurons in an APPPS1 model of Alzheimer's disease. *Frontiers in Aging Neuroscience* 13:1–15.

Vlachos A, Becker D, Jedlicka P, Winkels R, Roeper J, Deller T (2012) Entorhinal denervation induces homeostatic synaptic scaling of excitatory postsynapses of dentate granule cells in mouse organotypic slice cultures. *PLoS One* 7:e32883.

Vossel K, Ranasinghe KG, Beagle AJ, La A, Ah Pook K, Castro M, Mizuiri D, Honma SM, Venkateswaran N, Koestler M, Zhang W, Mucke L, Howell MJ, Possin KL, Kramer JH, Boxer AL, Miller BL, Nagarajan SS, Kirsch HE (2021) Effect of levetiracetam on cognition in patients with alzheimer disease with and without epileptiform activity: A randomized clinical trial. *JAMA Neurology* 78:1345–1354.

Vossel KA, Beagle AJ, Rabinovici GD, Shu H, Lee SE, Naasan G, Hegde M, Cornes SB, Henry ML, Nelson AB et al. (2013) Seizures and epileptiform activity in the early stages of Alzheimer disease. *JAMA Neurology* 70:1158–1166.

Vossel KA, Tartaglia MC, Nygaard HB, Zeman AZ, Miller BL (2017) Epileptic activity in Alzheimer's disease: causes and clinical relevance. *The Lancet Neurology* 16:311–322.

Vuksic M, Del Turco D, Vlachos A, Schuldt G, Müller CM, Schneider G, Deller T (2011) Unilateral entorhinal denervation leads to long-lasting dendritic alterations of mouse hippocampal granule cells. *Experimental neurology* 230:176–185.

Vyas Y, Montgomery JM, Cheyne JE (2020) Hippocampal deficits in amyloid-β-related rodent models of Alzheimer's disease. *Frontiers in neuroscience* 14:266.

Wang F, Zhang Y, Wang L, Sun P, Luo X, Ishigaki Y, Sugai T, Yamamoto R, Kato N (2015a) Improvement of spatial learning by facilitating large-conductance calcium-activated potassium channel with transcranial magnetic stimulation in Alzheimer's disease model mice. *Neuropharmacology* 97:210–219.

Wang L, Kang H, Li Y, Shui Y, Yamamoto R, Sugai T, Kato N (2015b) Cognitive recovery by chronic activation of the large-conductance calcium-activated potassium channel in a mouse model of Alzheimer's disease. *Neuropharmacology* 92:8–15.

Wang X, Zhang XG, Zhou TT, Li N, Jang CY, Xiao ZC, Ma QH, Li S (2016) Elevated neuronal excitability due to modulation of the voltage-gated sodium channel Nav1.6 by Aβ1-42. *Frontiers in Neuroscience* 10:1–9.

Weaver CM, Wearne SL (2008) Neuronal firing sensitivity to morphologic and active membrane parameters. *PLoS Computational Biology* 4:130–150.

Wellmer J, Su H, Beck H, Yaari Y (2002) Long-lasting modification of intrinsic discharge properties in subicular neurons following status epilepticus. *European Journal of Neuroscience* 16:259–266.

Williams PL, Beer RD (2010) Nonnegative decomposition of multivariate information. *arXiv preprint arXiv:1004.2515* .

Williams SR, Stuart GJ (1999) Mechanisms and consequences of action potential burst firing in rat neocortical pyramidal neurons. *The Journal of Physiology* 521 Pt 2:467–482.

Wilmes KA, Clopath C (2023) Dendrites help mitigate the plasticity-stability dilemma. *Scientific Reports* 13:6543.

Wittenberg GM, Wang SSH (2007) Evolution and scaling of dendrites. *Dendrites. Oxford University Press, New York* pp. 43–67.

Witter MP, Kleven H, Flatmoen AK (2017) Comparative contemplations on the hippocampus. *Brain, Behavior and Evolution* 90:15–24.

Xu W, Fitzgerald S, Nixon RA, Levy E, Wilson DA (2015) Early hyperactivity in lateral entorhinal cortex is associated with elevated levels of AβPP metabolites in the Tg2576 mouse model of Alzheimer's disease. *Experimental Neurology* 264:82–91.

Xu Y, Zhao M, Han Y, Zhang H (2020) GABAergic inhibitory interneuron deficits in Alzheimer's disease: implications for treatment. *Frontiers in Neuroscience* 14:660.

Yaari Y, Yue C, Su H (2007) Recruitment of apical dendritic T-type Ca2+ channels by backpropagating spikes underlies de novo intrinsic bursting in hippocampal epileptogenesis. *The Journal of Physiology* 580:435.

Yang J, Prescott SA (2023) Homeostatic regulation of neuronal function: importance of degeneracy and pleiotropy. *Frontiers in Cellular Neuroscience* 17:1184563.

Yang J, Shakil H, Ratté S, Prescott SA (2022) Minimal requirements for a neuron to coregulate many properties and the implications for ion channel correlations and robustness. *Elife* 11:e72875.

Yassa MA, Stark CE (2011) Pattern separation in the hippocampus. *Trends in neurosciences* 34:515–525.

Yau Sy, Li A, So KF et al. (2015) Involvement of adult hippocampal neurogenesis in learning and forgetting. *Neural plasticity* 2015.

Yin J, Yuan Q (2015) Structural homeostasis in the nervous system: a balancing act for wiring plasticity and stability. *Frontiers in cellular neuroscience* 8:439.

Yu L, Yu Y (2017) Energy-efficient neural information processing in individual neurons and neuronal networks. *Journal of Neuroscience Research* 95:2253–2266.

Yue C, Remy S, Su H, Beck H, Yaari Y (2005) Proximal persistent Na+ channels drive spike afterdepolarizations and associated bursting in adult CA1 pyramidal cells. *Journal of Neuroscience* 25:9704–9720.

Yuste R (2015) From the neuron doctrine to neural networks. *Nature reviews neuroscience* 16:487–497.

Zang Y, Marder E (2023) Neuronal morphology enhances robustness to perturbations of channel densities. *Proceedings of the National Academy of Sciences* 120:e2219049120.

Zbili M, Rama S, Benitez MJ, Fronzaroli-Molinieres L, Bialowas A, Boumedine-Guignon N, Garrido JJ, Debanne D (2021) Homeostatic regulation of axonal kv1. 1 channels accounts for both synaptic and intrinsic modifications in the hippocampal ca3 circuit. *Proceedings of the National Academy of Sciences* 118:e2110601118.

Zhang Y, Shi ZG, Wang ZH, Li JG, Chen JY, Zhang C (2014) Effects of amyloid β-peptide fragment 31-35 on the BK channel-mediated K+ current and intracellular free Ca2+ concentration of hippocampal CA1 neurons. *Neuroscience Letters* 568:72–76.

Zott B, Busche MA, Sperling RA, Konnerth A (2018) What happens with the circuit in Alzheimer's disease in mice and humans? *Annual Review of Neuroscience* 41:277–297.

Zott B, Simon MM, Hong W, Unger F, Chen-Engerer HJ, Frosch MP, Sakmann B, Walsh DM, Konnerth A (2019) A vicious cycle of β amyloid−dependent neuronal hyperactivation. *Science* 365:559–565.